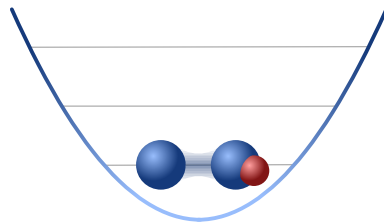

Sideband Cooling of Atomic and Molecular Ions



PhD Thesis

November 2011

Gregers Poulsen

Center for Quantum Optics – QUANTOP
Department of Physics and Astronomy
University of Aarhus, Denmark

This thesis is submitted to the Faculty of Science at the University of Aarhus, Denmark, in order to fulfill the requirements for obtaining the PhD degree in Physics. The studies have been carried out under the supervision of Prof. Michael Drewsen in the Ion Trap Group at the Institute of Physics and Astronomy, University of Aarhus from December 2008 to November 2011.



Gregers Poulsen
Sideband Cooling of Atomic and Molecular Ions
University of Aarhus 2011
Electronic Version, Published January 2012

Abstract

Research in the field of cold trapped molecules has attracted increasing interest over the last decade. Methods to prepare molecules in well-defined quantum states are particularly exciting, as they would enable high precision spectroscopy and state-selected reaction-chemistry studies. Control of the internal states of molecular ions can be realized by coupling their internal degrees of freedom to the translational motion in a Coulomb crystal. The work described in this thesis takes a step towards realizing such experiments with the experimental demonstration of sympathetic cooling of a single molecular ion to the motional ground state.

We demonstrate cooling of a $^{40}\text{CaH}^+$ molecular ion through sympathetic sideband cooling with an atomic ion to a ground state population of 86%. Simulations indicate that the remaining population is trapped in highly excited states, and with an improved cooling scheme we expect a significantly increased ground state occupation. The cooling scheme employs a co-trapped atomic $^{40}\text{Ca}^+$ ion driven on the narrow $S_{1/2} \leftrightarrow D_{5/2}$ transition. This transition is addressed with a laser system stabilized to a newly designed Zerodur reference cavity which shows a thermal sensitivity of only $4 \cdot 10^{-9}$ K. The linewidth of the laser has been estimated from the in-loop error signal to be below 55 Hz.

We also explore the possibility of decreasing the ion's energy and increasing the coupling between its motion and the light field through adiabatic lowering of the trapping potential. This is investigated from both Doppler- and sideband-cooled initial conditions, demonstrating tools for both simple sub-Doppler cooling and reduction of the zero-point energy of the motion; both of which are very relevant in studies of ultra-cold chemistry. With this procedure, we realize a secular kinetic energy corresponding to a temperature of only $6.8 \mu\text{K}$. The experiments are realized in a macroscopic RF Paul trap. The motional heating in this trap has been investigated and shows a heating rate of only a single quantum per second. This is also promising for investigating even lower adiabatic potentials.

List of Publications

- [I] G. Poulsen, Y. Miroshnychenko and M. Drewsen, "*Ground state cooling of an ion in a macroscopic trap with ultra-low heating rate*", Manuscript in preparation.
- [II] G. Poulsen and M. Drewsen, "*Adiabatic cooling of an ion in an rf trap*", Manuscript in preparation.
- [III] G. Poulsen and M. Drewsen, "*Sympathetic ground state sideband cooling of a single molecular ion*", Manuscript in preparation.

List of Acronyms

amu	atomic mass unit	115
AOM	Acousto-Optic Modulator	75
AR	Anti-Reflection	75
CCD	Charge-Coupled Device	77
DDS	Direct Digital Synthesizer	136
EOM	Electro-Optic Modulator	47
ExpCtrl	ExperimentController	135
ExpItr	ExperimentIterator	135
FET	Field Effect Transistor	75
FPGA	Field Programmable Gate Array	136
FWHM	Full Width at Half Maximum	16
GUI	Graphical User Interface	135
GUI	Graphical User Interface	135
NTC	Negative Temperature Coefficient	65
PD	Photo Detector	77
PDH	Pound-Drever-Hall	45
PID	Proportional-Integral-Derivative	59
PZT	Piezo-Electric Transducer	75
QE	Quantum Efficiency	89
SeqCom	SequenceComponents	136
SM/PM	Single Mode Polarization Maintaining	75
SRS	Sympathetic Recoil Spectroscopy	23
TTL	Transistor-Transistor Logic	93

Contents

Abstract	i
List of Publications	iii
List of Acronyms	v
Contents	vi
1 Introduction	1
1.1 Thesis Outline	4
I General Physics of Trapped Ions	5
2 Trapping Ions	7
2.1 The linear Paul Trap	8
2.2 Quantum Mechanics of the Ion Motion	13
2.3 The Motion of Two co-trapped Ions	14
3 Atom-Light Interactions	15
3.1 The Free Two-Level Atom	15
3.2 Interaction with a Trapped Ion	19
3.3 The Secular Motion as a State Mediator	21
4 Cooling of Trapped Ions	25
4.1 Doppler Cooling	26
4.2 Sideband Cooling	29
4.3 Determination of the Motional State	32
5 Manipulating the $^{40}\text{Ca}^+$ ion	37
5.1 Doppler Cooling	38
5.2 Sideband Cooling	38
5.3 Detecting the Internal State	38

II Laser Stabilization	41
6 Introduction	43
7 Laser Stabilization using Optical Resonators	45
7.1 The Optical Resonator	45
7.2 The Pound-Drever-Hall Technique	47
7.3 Experimental Considerations	50
8 Control Theory	53
8.1 Transfer Functions	53
8.2 The Feedback Loop	55
8.3 Lead and Lag Regulators	59
8.4 Laser Locking	62
9 Optical Resonator Design	65
9.1 Temperature Stabilization	65
9.2 Vibration isolation	68
10 Setup and Measurements	75
10.1 The Laser Source and Setup	75
10.2 The Optical Setup for Stabilization	77
10.3 The Electronic System	77
10.4 The Stabilized Linewidth	80
10.5 Long Term Stability of the Resonator	82
III Experiments with Trapped Ions	85
11 Experimental Equipment and Methods	87
11.1 Confinement of Ions	87
11.2 Imaging System	89
11.3 Optical Geometry and Light Sources	89
11.4 Control System	92
11.5 Experimental Procedures	93
12 Sideband Cooling and Motional Dynamics	97
12.1 Spectroscopy on the $S_{1/2} \leftrightarrow D_{5/2}$ Transition	97
12.2 Dynamics after Doppler Cooling	99
12.3 Sideband Cooling	100
12.4 Dynamics after Sideband Cooling	102
12.5 Motional Decoherence	102
12.6 Conclusion	106
13 Adiabatic Cooling	109
13.1 Doppler Cooled	109
13.2 Sideband Cooled	112
13.3 Conclusion	113

14 Sympathetic Sideband Cooling of Molecular Ions	115
14.1 Sideband Spectrum of a Two Ion Crystal	115
14.2 Formation/Identification of Molecular Ions	116
14.3 Sideband Cooling	117
14.4 Conclusion	118
15 Summary and Outlook	121
IV Appendix	123
A Ion motion in presence of stray electric fields	125
B The $^{40}\text{Ca}^+$ ion	127
B.1 Dipole Transitions	127
B.2 Zeeman-splitting	129
B.3 The $S_{1/2} \leftrightarrow D_{5/2}$ Transition	130
C Sideband Cooling Simulation	133
D Control System	135
D.1 Software System	135
D.2 Hardware System	136
Bibliography	139

CHAPTER 1

Introduction

Experimental physicists have always sought isolated and well-controlled systems to investigate nature. This is especially true in the field of quantum mechanics, and its foundation around a century ago was naturally followed by interest in isolating and investigating single quantum systems.

One way to isolate single quantum systems (atoms) appeared in the middle of the 20th century when Wolfgang Paul invented the quadrupole mass filter [1]. Paul's mass filter used a set of oscillating potentials to confine ions in two dimensions, and with a slight modification this idea could be used to confine ions in all three dimensions; a device known today as the Paul trap. With the invention of the ion trap, it was possible to study atoms in detail, and in the 1960's, Dehmelt's group published the first atomic hyperfine structure measurements with trapped $^3\text{He}^+$ ions [2]. These experiments demonstrated that confinement of ions provides a unique way to realize high precision spectroscopy. Around a decade later, this was taken one step further when it was realized that atoms could be cooled using laser radiation [3, 4]; a technique known today as Doppler cooling. By cooling the ions to low temperatures, it was possible to suppress Doppler broadening and achieve even higher precision. In 1978, the first optical observation of a single ion was demonstrated by Toschek et al. [5]. From this point on, it was possible to study the evolution of a single quantum system. This eventually led to optical clocks based on single trapped ions; pioneered by the $^{199}\text{Hg}^+$ based clock developed in Wineland's group at NIST [6]. With the development of the optical frequency comb [7, 8], it became possible to down-convert optical frequencies, and the $^{199}\text{Hg}^+$ based clock now outperforms previous Cesium-based atomic clocks [9].

Doppler cooling relies on continuous scattering of photons. To achieve this, the ions must provide a set of reasonably closed transitions to avoid decay into states where they do not interact with the cooling light. This has

confined these experiments to a limited set of ions, primarily atomic ions from the alkaline earth and transition metals. Recently, direct Doppler cooling of SrF molecules has been demonstrated [10], and AlH^+ and BH^+ have also been proposed as possible molecular ion candidates for Doppler cooling [11]. Most molecular ions remain, however, unsuitable for laser cooling, due to decays to different rovibrational levels. One way to overcome this is to sympathetically cool the molecular ions together with atomic ions in so-called Coulomb crystals; a technique which has been applied for more than a decade [12, 13]. This technique has for example been used to realize vibrational spectroscopy of HD^+ ions [14]. These ions do not provide cycling transitions, and this measurement therefore relied on destructive detection using Resonance Enhanced Multi-Photon Dissociation on a large ion crystal. Such large crystals give rise to additional Doppler broadening; performing similar measurements with only a few ions could potentially increase the precision. To realize this, a non-destructive detection technique would be valuable. Fortunately, another branch of ion-trapping, that of quantum information processing, has provided ideas to extend single ion spectroscopy to species lacking cycling transitions: the so-called quantum bus.

The idea for this quantum bus appeared in the middle of the 1990's when Cirac and Zoller proposed the ion-trap-based quantum computer [15]. The quantum computer has been a hot topic for many physicists since Feynman and Deutsch proposed such a device back in the 1980's [16, 17]. This device could potentially provide the ability to simulate quantum systems which are too complicated for classical computers. The basic idea behind Cirac and Zoller's proposal was to use the quantum mechanical motion of the ions inside the trapping potential to transfer information between the ions (qubits). Since then, new proposals have appeared which make this scheme more robust [18], but the basic principle remains the same: to use the common motion of the ions to transfer quantum information.

Quantum logic is, however, not only interesting for information processing: it can also be used to realize spectroscopy of otherwise inaccessible ion species [19]. By proper application, quantum logic can be used to determine the internal state of a *spectroscopy* ion using an *auxiliary* ion. In this case, only the *auxiliary* ion is required to provide a closed level scheme for cooling and state detection, and this enables high precision spectroscopy of a much wider range of ions - including molecular ions.

This technique has applications in many fields, for example for metrology: When atomic transitions are used as a frequency reference, the transition should naturally be chosen to be narrow and relatively insensitive to external perturbations. Previously, the number of candidate species was reduced by the requirement that the ion should also provide a closed level scheme

to realize cooling and detection. With quantum logic, this is no longer a requirement: an ion can be chosen only to provide a good clock transition and a co-trapped atomic ion can then be responsible for the other requirements. This has, for example, been used to realize an atomic clock using a single $^{27}\text{Al}^+$ ion trapped together with a $^9\text{Be}^+$ ion [20]; outperforming the previous single ion $^{199}\text{Hg}^+$ based clock [21, 22].

The goal of the research project described in this thesis is to extend these high precision studies to molecules. Using quantum logic, it is possible to realize non-destructive spectroscopy in the Lamb-Dicke limit and thereby achieve very high precision. Such spectroscopic measurements are interesting for many reasons: First of all, spectroscopy of molecular ions provides an opportunity to realize high precision measurements of electronic and rovibrational transition frequencies. Such measurements can be valuable to improve the understanding of molecular quantum mechanics by comparing these measurements to current theoretical calculations, for example for the astrophysically relevant CaH^+ molecule [23, 24]. In addition, such studies are relevant for testing fundamental physics, for example through a more precise value of the electron to proton mass ratio [25], the search for the electron electric dipole moment [26] or for a possible time evolution of the fine structure constant [27].

Realizing this technique requires cooling to the motional ground state in the external potential. This also provides other interesting possibilities, for example studies of cold chemistry: By cooling to the motional ground state, only a small kinetic energy remains from the zero-point motion, which can be as low as a few μK . This makes it possible to realize reactive scattering experiments at very low temperatures [28]. By coupling the external motion to the internal degrees of freedom, it is further possible to prepare molecules in well-defined rovibrational states [29]. This could further enable state-selected reactive-collision studies [30] or even quantum information processing [31].

1.1 Thesis Outline

This thesis is organized in three parts. [Part I](#) contains an introduction to the field of trapped ions and their interaction with light and explains how this interaction can be used to manipulate the internal and external state of the ions to eventually cool them to the ground state. For the reader with previous experience in this field, it should be noted that [Section 3.3](#) and [Section 4.3](#) introduces some new concepts.

[Part II](#) is focused on a more practical aspect of quantum optics, that of laser stabilization. This part contains a general introduction to the theory of laser stabilization in addition to a description of the specific laser system constructed to realize the experiments reported in this thesis.

The final part, [Part III](#), is dedicated to the actual experiments with trapped atomic and molecular ions. It includes a description of the experimental equipment and, most importantly, the experiments and the results.

Part I

General Physics of Trapped Ions

CHAPTER 2

Trapping Ions

To realize experiments with single atoms, they must be confined in a narrow region of space. Trapping of neutral atoms can be realized for example in a magnetic-trap or a magneto-optical-trap, but these either have relatively small well-depths or introduce large perturbations to the atoms. By ionizing the atoms, the Coulomb interaction between the ions and electromagnetic fields (which are orders of magnitudes larger) can be exploited to obtain well-depths of several eV; even for moderate field strengths.

To confine a particle in space, a potential energy minimum must be established, so that the corresponding force in all three dimensions points toward this point. In general, the magnitude of this force can have an arbitrary form, but the analytical description simplifies if the potential is harmonic ($\phi = m\omega^2 x^2/2$). In the quantum mechanical regime, this also gives rise to a set of equidistant motional levels which is important for sideband cooling as discussed in [Chapter 4](#). In a harmonic potential, the restoring force is proportional to the displacement ($d^2x/dt^2 = -\omega^2 x$) and the resulting motion is simple harmonic.

Static electric potentials are easy to implement, and it would be ideal if it was possible to trap an ion between a set of electrodes with a harmonic potential of the form:

$$\phi = \phi_0(\alpha x^2 + \beta y^2 + \gamma z^2) \quad (2.1)$$

The electric potential has to satisfy Laplace's equation ($\nabla^2\phi = 0$ [32]). Except for the trivial case where $\phi_0 = 0$, this requires that

$$\alpha + \beta + \gamma = 0. \quad (2.2)$$

This implies that at least one of the coefficients has to be negative; the static potential cannot be confining in all directions at the same time - the potential has the shape of a saddle point. The equilibrium can, however, be dynamically stabilized by varying the potential, ϕ , in time, as realized by Wolfgang

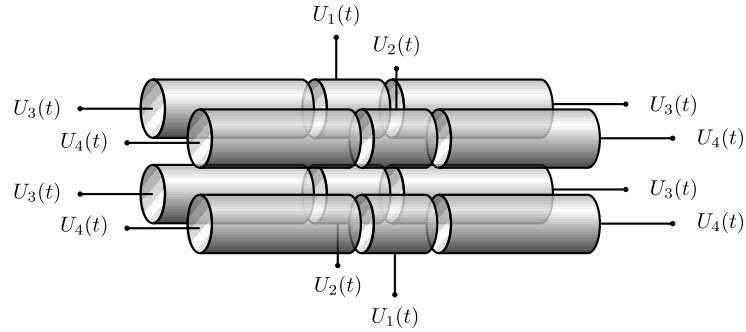


Figure 2.1: Illustration of the linear Paul trap. The potentials on the electrodes are given by: $U_1(t) = U_{\text{rf}} \cos(\Omega t)$, $U_2(t) = -U_{\text{rf}} \cos(\Omega t)$, $U_3(t) = U_{\text{rf}} \cos(\Omega t) + U_{\text{dc}}$ and $U_4(t) = -U_{\text{rf}} \cos(\Omega t) + U_{\text{dc}}$

Paul in 1953 [1].¹ Paul’s original mass filter used an oscillating RF-field to trap charged particles in two dimensions, but it was early realized that the same technique could be used to trap charged particles in three dimension, a device they called “Ionenkäfig”, for which Paul shared the 1989 Nobel Prize in physics [34].

“Ionenkäfig” used a 3D oscillating field to localize the ion, but later a modification of this trap, called the linear Paul trap, has become a popular tool in atomic physics.

2.1 The linear Paul Trap

The linear Paul Trap consists of a set of electrodes configured to confine the particle in two dimensions by an oscillating RF-field (like the original mass filter) and in the third by a static DC-field. With this configuration, there is not only one point in space with zero RF amplitude but instead a line. This opens a possibility to trap several ions along this axis without imposing further micromotion on the ion. In addition, this configuration has a more open geometry which provides better access for laser beams. A typical experimental realization of the linear Paul trap is illustrated in Figure 2.1.

To obtain a quadrupole field as in Equation 2.1, the surface of the electrodes must be hyperbolic (following the quadrupole potential curves). In practice, it is much easier to construct a trap with cylindrical electrodes as illustrated in the figure. The resulting potential will then deviate from a pure quadrupole potential, but if the dimensions of the trap are chosen correctly

¹ An intuitive understanding of the dynamic stabilization by a time-varying potential can be gained from a similar mechanical analog with a ball in a saddle trap. The rotating potential is a bit different but gives a nice demonstration experiment which shows the idea [33].

these deviations will be small. With $r_e = 1.03r_0$, the contribution from anharmonic terms is less than 0.1% in the range from the trap axis to $0.2r_0$ [35].

In the dynamically stabilized trap, the quadrupole potential can be written as:

$$\begin{aligned} \phi = & \frac{1}{2}U_{dc}(\alpha_{dc}x^2 + \beta_{dc}y^2 + \gamma_{dc}z^2) \\ & + \frac{1}{2}U_{rf}\cos(\Omega t)(\alpha_{rf}x^2 + \beta_{rf}y^2 + \gamma_{rf}z^2), \end{aligned} \quad (2.3)$$

where U_{dc} is the DC potential at the end electrodes and U_{rf} is the amplitude of the RF signal oscillating at frequency Ω . The geometric factors (α, β, γ) are included as arbitrary constants. In practice, they depend on the geometry of the trap and are typically found through numeric simulation of the trap potentials.² The potential has to fulfill the Laplace equation ($\nabla^2\phi = 0$) at all instants in time. This restricts the values of the parameters to:

$$\begin{aligned} \alpha_{dc} + \beta_{dc} + \gamma_{dc} &= 0 \\ \alpha_{rf} + \beta_{rf} + \gamma_{rf} &= 0 \end{aligned} \quad (2.4)$$

In the linear Paul Trap, the RF parameters are identical to the parameters of the mass filter ($\alpha_{rf} = -\beta_{rf} \equiv \alpha$).

The DC potential in the z-direction results in defocusing in the two other directions with the parameters $-\alpha_{dc} - \beta_{dc} = \gamma_{dc} \equiv \gamma$. Naturally, γ must be positive in order to achieve confinement in the z-direction. With Newton's 2nd law, the equations of motion of a particle with mass m and charge q can be written as:

$$\begin{aligned} \frac{d^2x}{dt^2} &= -\frac{q}{m} \left(-\frac{1}{2}U_{dc}\gamma + U_{rf}\alpha \cos(\Omega t) \right) x \\ \frac{d^2y}{dt^2} &= -\frac{q}{m} \left(-\frac{1}{2}U_{dc}\gamma - U_{rf}\alpha \cos(\Omega t) \right) y \\ \frac{d^2z}{dt^2} &= \frac{q}{m} (-U_{dc}\gamma)z \end{aligned} \quad (2.5)$$

With the substitutions

$$\begin{aligned} a_x = a_y &= -\frac{2qU_{dc}\gamma}{m\Omega^2}, \quad q_x = -q_y = -\frac{2qU_{rf}\alpha}{m\Omega^2}, \quad \xi = \frac{\Omega_{rf}t}{2}, \\ a_z &= \frac{4q\gamma U_{dc}}{m\Omega^2} \quad \text{and} \quad q_z = 0, \end{aligned} \quad (2.6)$$

the equations of motion take the standard form of the Mathieu equation:

$$\frac{d^2r_i}{d\xi^2} + (a_i - 2q_i \cos(2\xi))r_i = 0, \quad r_i = x, y, z \quad (2.7)$$

² The specific factors of the trap used in this work are described in [Chapter 11](#).

The Mathieu equation has been studied widely throughout the literature (see for example [36]), and according to Floquet's theorem, solutions to this equation take the form

$$w_1(\zeta) = e^{\mu\zeta}\Psi(\zeta), \quad w_2(\zeta) = e^{-\mu\zeta}\Psi(\zeta), \quad (2.8)$$

where $\Psi(\zeta)$ is a π -periodic function and $\mu = \alpha + i\beta$ where α and β are real functions of a and q . If the ion-path inside the trap is to be bound, the solution to the Mathieu equation must be periodic; in the mathematical literature these solutions are termed stable. Looking at Equation 2.8, it appears that if the solutions are to be stable, α must be 0. If $\alpha \neq 0$, the solution will contain an exponential term. Since α depends solely on a and q , it is clear that these depict the stability of the trap. A stability diagram of the Mathieu equation is shown in Figure 2.2a.

Stable solutions only exist for certain pairs of a, q , and these must be chosen correctly to trap ions. In a multidimensional trap, the particles are only confined when the solutions to the Mathieu equation are stable in all directions. In the case of the linear Paul trap, the stability diagram is the same for both the x- and y-axis because $a_x = a_y$, $q_x = -q_y$, and the diagram is symmetric around $q = 0$. The resulting stability diagram is therefore the same for these directions combined. In the z-direction, q is zero, and the equation reduces to that of the normal harmonic oscillator, hence the particle is bound in this direction for all pairs of a, q as long as $a_z > 0$ ($a_x, a_y < 0$). The combined stability diagram for all 3 dimensions is shown in Figure 2.2b.

Stable solutions exist for all values of q , but the stability range for a gets very narrow for large q 's. This is different from the stability diagram of the original mass filter. Here $a_x = -a_y$ and $q_x = -q_y$, and because the stability

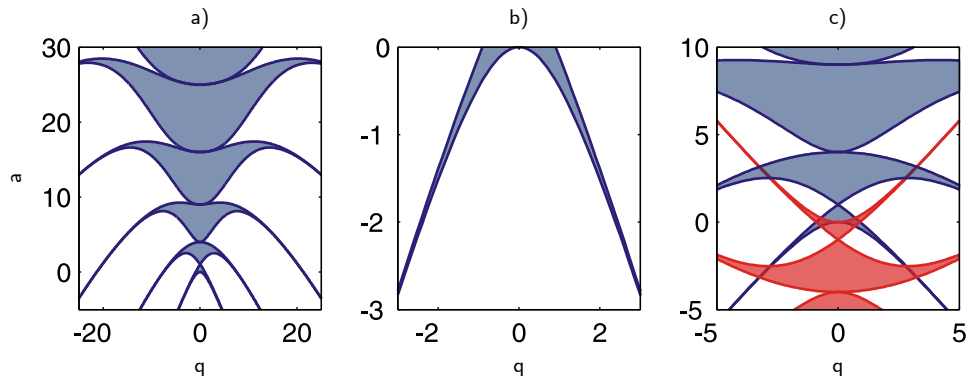


Figure 2.2: Stability diagram of the Mathieu equation. The shaded areas contain stable solutions of the equation (bound ion trajectories). a) A single dimension b) Combined equations for the linear Paul trap. c) Combined equations for the mass filter.

diagram is not symmetric around the q -axis, the resultant solutions which are both x - and y -stable reduces for the mass filter, as shown in Figure 2.2c.

The Mathieu equation belongs to a general group of differential equations with periodical coefficients. The stable solutions are given by [37]

$$r_i(\xi) = A_i \sum_{n=-\infty}^{\infty} C_{2n}^i \cos((2n \pm \beta_i)\xi) + B_i \sum_{n=-\infty}^{\infty} C_{2n}^i \sin((2n \pm \beta_i)\xi), \quad (2.9)$$

where the real-valued β_i and the coefficients C_{2n}^i are functions of a_i and q_i only. The coefficients A and B are arbitrary constants that can be used to satisfy boundary conditions. The coefficients C_{2n}^i satisfy a recursion relation given by:

$$C_{2n+2}^i - D_{2n}^i C_{2n}^i + C_{2n-2}^i = 0, \quad D_{2n}^i = (a_i - (2n + \beta_i)^2) / q_i \quad (2.10)$$

Given a_i and q_i , β_i and C_{2n}^i can be calculated, but the recursion relation results in an infinite series. To better understand the physical principles governing the dynamical containment of the ion, approximations to the equation can be introduced.

2.1.1 Pseudo-potential Model

According to Equation 2.9, the ion oscillates at a number of different frequencies given by $\omega_n = (2n + \beta)\Omega/2$. When the trap is operated with $\beta \ll 1$, the fundamental frequency, $\omega_0 = \beta\Omega/2$, will be much smaller than the higher order frequencies, $\omega_n \approx n\Omega$. Additionally, the amplitude of the low-frequency secular motion will be larger than the amplitude of the high-frequency micromotion.³ This suggests that simplification can be obtained by separating the amplitude of the motion into two components given by

$$r_i = R_i + \delta_i \quad (2.11)$$

where R_i and δ_i represents the secular- and micro-motion respectively. With the assumptions $a_i \ll 1$ and $q_i \ll 1$, the equations of motion can be separated into two equations⁴

$$\begin{aligned} \frac{d^2 R_i}{dt^2} &= -\omega_i^2 R_i \\ \delta_i &= -\frac{q_i R_i}{2} \cos(2\xi), \end{aligned} \quad (2.12)$$

³ The trap described in Part III has typical values of $q = 0.86$ and $a = 0.04$ with frequencies $\omega_z = 2\pi \cdot 0.6$ MHz, $\Omega = 2\pi \cdot 3.7$ MHz and $\beta = 0.88$. In this case, $\beta \ll 1$ is not satisfied, but the pseudo-potential model provides an intuitive understanding of the trapping dynamics.

⁴ See Appendix A for an equivalent derivation.

where ω_i is the secular frequency in the i 'th direction given by:

$$\omega_i = \frac{\Omega}{2} \sqrt{\frac{q_i^2}{2} + a_i} = \frac{\Omega}{2} \beta_i \quad (2.13)$$

Solving the equations of motion gives an ion trajectory given by

$$r_i = r_i^0 \cos(\omega_i t + \phi_i) \left(1 - \frac{q_i}{2} \cos(\Omega t)\right) \quad (2.14)$$

where r_i^0 and ϕ_i is determined by initial conditions. The resulting ion motion is a harmonic motion at frequency ω_i , amplitude modulated at the RF-drive frequency Ω . The equations have been derived from physical approximations, but the same results are obtained by assuming that $C_{\pm 4} = 0$ [38, p. 284].

For small q_i , the micromotion can be neglected, and the motion of the ion is identical to the motion of a particle in a harmonic pseudo-potential:

$$\Psi_i = \frac{1}{2} m \omega_i^2 r_i^2 \quad (2.15)$$

When ions are loaded in the trap from a thermal beam ($\sim 500^\circ\text{C}$), they have a thermal energy of 0.03 eV. In the trap discussed in [Part III](#), the distance to the electrodes is 2.7 mm. With a radial oscillation frequency of $\omega_r = 2\pi \cdot 1$ MHz this gives a trap potential depth of 60 eV; more than enough to trap a beam of thermal ions.

2.1.2 Micromotion

Micromotion gives rise to modification of the absorption spectrum from an ion and can also introduce heating [39], and is generally unwanted.⁵

In an ideal Paul trap, micromotion is only present as a result of the secular motion [see [Equation 2.14](#)]. Quantum mechanics elucidates, that the secular motion will always be present due to the zero-point motion. The micromotion due to this effect is not significant, but excess micromotion can be imposed on the motion by external forces.

In the derivation of the motion, only the quadrupolar terms (contributing quadratically to the electric field) were considered. If stray electric charge is present in the neighborhood of the trap, the potential minimum will not necessarily be located at the point where the quadratic RF-terms vanish, and the ion will exhibit additional micromotion. This can be seen by adding an extra force term to [Equation 2.5](#)

$$\ddot{x} = -\frac{q}{m} (-U_{dc}\gamma + U_{rf}\alpha \cos(\Omega t))x + \frac{E_i q}{m}, \quad (2.16)$$

⁵ Micromotion has also been exploited to deterministically modify the Rabi frequencies of two ions and produce entanglement [40].

where E_i is the electric field due to the stray electric charge. In the pseudo-potential model this term is easily included, and the resulting ion motion is given by (see [Appendix A](#) for a derivation):

$$r_i = (r_i^e + r_i^0 \cos(\omega_i t + \phi_i)) \left(1 - \frac{q_i}{2} \cos(2\xi)\right). \quad (2.17)$$

The stray electric fields give rise to increased micromotion. Even if the ion is cooled to the motional ground state, the ion will still experience excess micromotion due to the term r_i^e . Stray fields can occur for example if ions accumulate on the electrodes or if the trap is exposed to ultraviolet light. To suppress this excess micromotion, additional DC voltage can be applied to the electrodes (or separate compensation electrodes) to overlap the potential minimum with the line where the RF-field vanishes.

Another source of excess micromotion can be phase or amplitude differences of the RF-potentials at the electrodes.⁶ Phase differences of the RF-potentials can occur if the wires from the RF-source are of different length or if the impedance matching is different. In addition, asymmetry of the electrodes also changes the potential minimum.

The kinetic energy of the ion in the trap can be reduced by laser cooling as described in [Chapter 4](#). When the energy of the ion becomes comparable to $\hbar\omega_i$, the motion has to be treated quantum mechanically. This simplifies significantly in the regime of small q_i (and without excess micromotion), since the system can then be treated as a regular 3-dimensional harmonic oscillator.

2.2 Quantum Mechanics of the Ion Motion

In the pseudo-potential model, the motion of the ion is treated as a harmonic oscillator. In this case, the potential can be quantized following the usual textbook approach. In this section, the quantum mechanical results will be summarized; for a derivation consult for example [\[42\]](#).

The Hamiltonian of the harmonic oscillator is given by

$$H = \frac{p^2}{2m} + \frac{1}{2}m\omega^2 r^2 \quad (2.18)$$

This can be rewritten in terms of the usual creation and annihilation operators

$$\hat{a}, \hat{a}^\dagger = \sqrt{\frac{m\omega}{2\hbar}} r \mp \frac{i}{\sqrt{2m\hbar\omega}} p, \quad (2.19)$$

⁶ Amplitude difference of the RF-voltages can also be exploited to compensate for micromotion by moving the RF-null into the potential minimum [\[41\]](#).

and the Hamiltonian of the trap takes the form:

$$H_t = \hbar\omega \left(\hat{a}^\dagger \hat{a} + \frac{1}{2} \right) \quad (2.20)$$

By inspection of this equation, it is evident that the lowest level, $|0\rangle$, has an energy of $\hbar\omega/2$ and exhibits zero-point motion. With aid of the position operator given by

$$r = \sqrt{\frac{\hbar}{2m\omega}} (\hat{a} + \hat{a}^\dagger), \quad (2.21)$$

the spread of the wavefunction can be calculated to:

$$\sqrt{\langle n|r^2|n\rangle} = \sqrt{(2n+1)} \sqrt{\frac{\hbar}{2m\omega}} \quad (2.22)$$

This will be important in the treatment of the interaction with light discussed in [Chapter 3](#). In a trap with secular frequency $\omega = 2\pi \cdot 500$ kHz, the equation shows that a single $^{40}\text{Ca}^+$ ion in the ground state of the trap will be confined within 15 nm.

If micromotion is not compensated correctly, the pseudo-potential approximation is not applicable. In this case, the quantum-mechanics of the motion can be treated by introducing a time-dependent harmonic potential $\omega(t)$ [38]. In this treatment, the position operator is given by

$$r = \sqrt{\frac{\hbar}{2m\omega}} (\hat{a}u^*(t) + \hat{a}^\dagger u(t)), \quad (2.23)$$

where $u(t) = e^{i\beta\Omega/2} \sum_{n=-\infty}^{\infty} C_{2n} e^{in\Omega t}$.

2.3 The Motion of Two co-trapped Ions

In the experiments described in this thesis, we primarily focus on the motion along the axis of the trap. For a single ion in a harmonic potential, this gives a trivial harmonic motion with frequency ω_z . The motion is however more complicated if two ions are confined along the axis. In this case, the combined motion of the ions can be separated into two normal modes with frequencies given by [43]:

$$\omega_{\pm}^2 = \omega_z^2 \left(1 + \frac{1}{\mu} \pm \sqrt{1 - \frac{1}{\mu} + \frac{1}{\mu^2}} \right), \quad (2.24)$$

where $\mu = \frac{m_2}{m_1}$ is the ratio between the mass of the two ions. In case the ions have identical mass ($\mu = 1$), the frequencies will reduce to $\omega_- = \omega_z$ and $\omega_+ = \sqrt{3}\omega_z$. In this case, the two modes can be pictured as the ions moving together in phase (center of mass mode) or out of phase (stretch mode). For different masses, ω_- will not be the genuine center of mass motion, but for similar masses it resembles the center of mass mode well.

Atom-Light Interactions

Light is an indispensable tool for manipulating the states of an atom and can be used to cool the motion of trapped ions. The purpose of this chapter is to introduce the basic interaction between atoms and light.

The theory is developed for an ideal atom containing two levels. In practice, this can be realized if the frequency of the electromagnetic fields are close to resonance for only two internal levels and if the Rabi frequencies are much smaller than the detunings for off-resonant transitions.

3.1 The Free Two-Level Atom

The electronic structure of the two-level atom is described by the ground state, $|g\rangle$, and the excited state, $|e\rangle$, with energies $\hbar\omega_g$ and $\hbar\omega_e$ respectively. The corresponding atomic Hamiltonian is:

$$H_a = \hbar\omega_g|g\rangle\langle g| + \hbar\omega_e|e\rangle\langle e| \quad (3.1)$$

The atomic wavefunction can be written as a superposition of the two eigenstates $|\psi\rangle = c_g|g\rangle + c_e|e\rangle$, where c_g and c_e are complex coefficients.

3.1.1 Interaction with Light

The interaction between a two-level atom and a monochromatic running wave light-field of the form $\mathbf{E}(\mathbf{r}, t) = \mathbf{E}_0[e^{i(\mathbf{k}\mathbf{x} - \omega t)} + e^{-i(\mathbf{k}\mathbf{x} - \omega t)}]$ can in general be described by the interaction Hamiltonian, H_i . The total Hamiltonian of the system is then:

$$H = H_a + H_i \quad (3.2)$$

By applying the dipole¹ and the rotating wave approximation², the interaction Hamiltonian can be written as [38]

$$H_i = \frac{\hbar}{2}\Omega(|g\rangle\langle e|e^{-i(\mathbf{k}\cdot\mathbf{x}-\omega_l t+\phi)} + |e\rangle\langle g|e^{i(\mathbf{k}\cdot\mathbf{x}-\omega_l t+\phi)}), \quad (3.3)$$

where \mathbf{k} is the wave-vector, \mathbf{x} is the position of the atom, ω_l is the angular frequency of the light, ϕ is a phase relevant to the given transition and Ω is the Rabi-frequency which depends on the matrix-element of the transition. For a dipole-transition this is given by $(\hbar/2)\Omega = e\langle g|\mathbf{E}_0 \cdot \mathbf{x}|e\rangle$.

Application of the time-dependent Schrödinger equation $i\hbar\partial\Psi/\partial t = H\Psi$ yields:

$$i\hbar\frac{d}{dt}\begin{bmatrix} c_g \\ c_e \end{bmatrix} = \frac{\hbar}{2}\begin{bmatrix} 2\omega_g & \Omega e^{-i(\mathbf{k}\cdot\mathbf{x}-\omega_l t+\phi)} \\ \Omega e^{i(\mathbf{k}\cdot\mathbf{x}-\omega_l t+\phi)} & 2\omega_e \end{bmatrix}\begin{bmatrix} c_g \\ c_e \end{bmatrix} \quad (3.4)$$

To simplify the problem, the energy can be rescaled to $\omega_g = 0$ and $\omega_a = \omega_e - \omega_g$. If the atom is at rest, the complex phase $e^{i(\mathbf{k}\cdot\mathbf{x}+\phi)}$ does not vary in time. It can be absorbed in the coefficients by converting to a rotating frame given by $\tilde{c}_g = c_g$ and $\tilde{c}_e = c_e e^{-i(\mathbf{k}\cdot\mathbf{x}-\omega_l t+\phi)}$. This gives the following equations for the coefficients:

$$i\hbar\frac{d}{dt}\begin{bmatrix} \tilde{c}_g \\ \tilde{c}_e \end{bmatrix} = \frac{\hbar}{2}\begin{bmatrix} 0 & \Omega \\ \Omega & 2\Delta \end{bmatrix}\begin{bmatrix} \tilde{c}_g \\ \tilde{c}_e \end{bmatrix}, \quad (3.5)$$

where $\Delta = \omega_l - \omega_a$ is the detuning of the laser relative to the atomic resonance. Differentiation and back substitution of Equation 3.5 gives the time evolution of the atomic eigenstate population:

$$\begin{aligned} |c_g(t)|^2 &= |\tilde{c}_g(t)|^2 = \cos^2\left(\frac{\chi t}{2}\right) + \frac{\Delta^2}{\chi^2}\sin^2\left(\frac{\chi t}{2}\right) \\ |c_e(t)|^2 &= \frac{|\Omega|^2}{\chi^2}\sin^2\left(\frac{\chi t}{2}\right), \end{aligned} \quad (3.6)$$

where $\chi = \sqrt{|\Omega|^2 + \Delta^2}$ is the off-resonant Rabi-frequency. The interaction has introduced time dependence to the coefficients, and the populations of the atomic eigenstates now oscillate at a frequency χ , which depends on both the Rabi frequency and the detuning. For a fixed interaction time, this gives rise to an oscillatory line shape as illustrated in Figure 3.1a. The envelope of the oscillations is Lorentzian with a Full Width at Half Maximum (FWHM) width of 2Γ .

The time dependence of the coefficients is illustrated in Figure 3.1b. This shows a perfect transfer (for $\Delta = 0$) of all population to the excited state

¹ The dipole approximation neglects the spatial phase change of the wave over the atom, $e^{i\mathbf{k}\cdot\mathbf{r}} \approx 1$. For blue light and $^{40}\text{Ca}^+$ this amounts to a phase shift of $\sim 2 \cdot 10^{-3}$ rad.

² The rotating wave approximation neglects all terms rotating at a frequency $\sim 2\omega$, the error due to this (termed the Bloch-Siegert shift) is in the order of 10^{-10} [44].

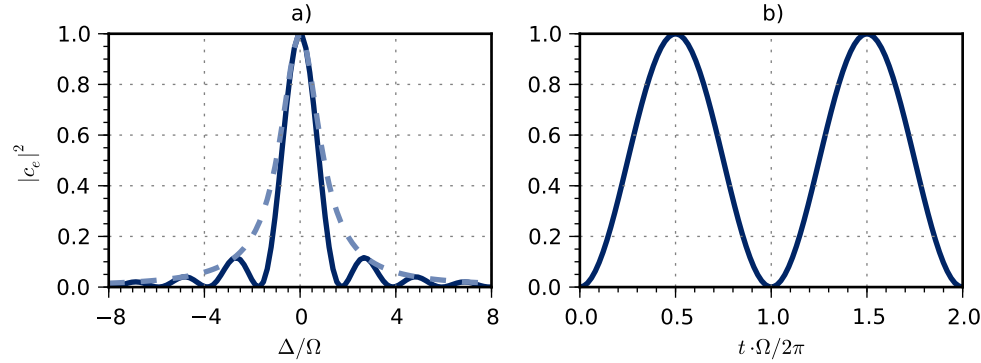


Figure 3.1: a) Line shape with a variable detuning and a fixed pulse length ($t = 2\pi/\Omega$). The dashed line illustrates the Lorentzian envelope with FWHM width of 2Γ . b) Rabi oscillations with a variable interaction time and a fixed detuning ($\Delta = 0$).

after an interaction time corresponding to $t\Omega = \pi$; a so-called π -pulse. The population transferred between the two states at a given time depends on both the Rabi frequency and the interaction time. When the atom is exposed to light pulses with a varying intensity, it is relevant to introduce the rotation angle:³

$$\Theta(t) = \int_{-\infty}^t |\Omega(t')| dt'. \quad (3.7)$$

Equation 3.6 show that when $\Delta = 0$, $\Theta(t)$ is a measure of the transferred population. When the area of the light pulse satisfies $\Theta(t) = \pi$, the population is inverted, and all population in $|g\rangle$ is transferred to $|e\rangle$. With aid of light pulses, one can tailor the atom into any superposition of the two eigenstates. With no other interactions present, the atom will stay in this superposition, but in the next section it will be clear that spontaneous decay can limit the this coherence.

This chapter is based on an ideal two-level atom, but real atoms contain many levels, and the radiation will couple to all these levels. Equation 3.6 indicates a measure of the valid range of the two-level approximation. If $\Omega \ll \Delta$ for all except the addressed transition, the population transfer to these states is small and can be neglected. The two-level approximation is valid if the frequency of the radiation is close to only one atomic resonance.

A typical addressed transition in $^{40}\text{Ca}^+$ is $S_{1/2} \leftrightarrow P_{1/2}$. The nearest level is the $P_{3/2}$ -level which is offset by $2\pi \cdot 7.7$ THz, and coupling to this level will rarely be important. Off-resonant coupling between motional levels (which

³ Until now, it has been assumed implicit that Ω is independent of time. This is not true for a light pulse, but if Ω varies slowly, so the rotating wave approximation is still applicable, the derived equations will still be valid with the substitution of $\Theta(t)$ for Ωt .

are typically separated $\sim 2\pi \cdot 0.5$ MHz) might however be important, and can in some cases limit the efficiency of sideband cooling.

3.1.2 Spontaneous Emission

In the previous section, it was established that interaction with monochromatic light gives rise to coherent transfer of population between the atomic eigenstates. In practice, the atom will also couple to the vacuum-field which will induce spontaneous emission, and for a dipole-allowed transition, this decay rate is often hundreds of megahertz. The atomic populations are easiest treated through the density-matrix formalism when spontaneous decay is involved. The density matrix for the two-level atom is given by:

$$\rho = \begin{bmatrix} \rho_{gg} & \rho_{ge} \\ \rho_{eg} & \rho_{ee} \end{bmatrix} = \begin{bmatrix} c_g c_g^* & c_g c_e^* \\ c_e c_g^* & c_e c_e^* \end{bmatrix} \quad (3.8)$$

The equations for ρ can easily be found by application of Equation 3.5.⁴ Including the spontaneous emission rate, Γ , gives the following equations [45]:

$$\begin{aligned} \frac{d}{dt}\rho_{gg} &= -\frac{i}{2}(\Omega\rho_{ge} - \Omega^*\rho_{eg}) + \Gamma\rho_{ee} \\ \frac{d}{dt}\rho_{ee} &= \frac{i}{2}(\Omega\rho_{ge} - \Omega^*\rho_{eg}) - \Gamma\rho_{ee} \\ \frac{d}{dt}\rho_{ge} &= i\Delta\rho_{ge} + \frac{i\Omega^*}{2}(\rho_{ee} - \rho_{gg}) - \frac{\Gamma}{2}\rho_{ge} \\ \frac{d}{dt}\rho_{eg} &= -i\Delta\rho_{eg} - \frac{i\Omega^*}{2}(\rho_{ee} - \rho_{gg}) - \frac{\Gamma}{2}\rho_{eg} \end{aligned} \quad (3.9)$$

The solution to these equations can be found numerically and shows damped Rabi-oscillations which will reach steady state after a time $t \gg 1/\Gamma$. In steady state, the population of the upper level can be written as:

$$\rho_{ee} = \frac{|\Omega|^2/4}{\Delta^2 + |\Omega|^2/2 + \Gamma^2/4} \quad (3.10)$$

Rewriting the equation in terms of $s = \frac{|\Omega|^2/2}{\Delta^2 + \Gamma^2/4}$ gives $\rho_{ee} = \frac{1}{2} \frac{s}{s+1}$, which shows that a population inversion greater than 1/2 cannot be achieved in an ensemble of two-level systems. It is often useful to define the on-resonance saturation parameter $s_0 = s(\delta = 0) = 2\Omega^2/\Gamma^2$. It can be shown that this relates to the intensity according to [46]

$$\frac{I}{I_{sat}} = \frac{2|\Omega|^2}{\Gamma^2}, \quad (3.11)$$

⁴ These equations are the same as in Equation 3.9 except the last terms containing Γ .

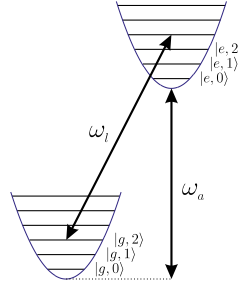


Figure 3.2: The atomic and motional levels of the trapped ion.

where $I_{sat} = \frac{\pi\hbar c\Gamma}{3\lambda^3}$. A transition is referred to as saturated when $I = I_{sat}$, which gives $\rho_{ee} = 1/4$.

Until now, the atom has been treated as stationary. If the atom is moving at a constant velocity, it will experience a Doppler shift of $\Delta\omega = kv$, where v is the velocity of the ion. This is easily included in the previous equations by absorbing the shift in the detuning: $\Delta' = \Delta + kv$.

When the ion is trapped, it will oscillate back and forth in the trap potential, and this makes new phenomena appear which will be treated in the next section.

3.2 Interaction with a Trapped Ion

The interaction between a trapped ion and light will be affected by the motion in the trap potential. The total Hamiltonian of the system will be the sum of the Hamiltonian for the atom and the trap:

$$H_{tot} = H_t + H_a \quad (3.12)$$

If it is assumed that the various degrees of freedom do not couple, the atomic eigenstates will be the combined states of the form $|g\rangle \otimes |n\rangle \equiv |g, n\rangle$ as illustrated in Figure 3.2.

The derivations in the previous section neglected movement of the ion by assuming that $d\mathbf{x}/dt = 0$. For a trapped ion, this is not true. In the classical picture, the ion oscillates back and forth in the trap potential. For these derivations we will focus on an oscillation in a single dimension with frequency ω_z - in reality, ω_z could represent any of the 3D oscillators (ω_x , ω_y or ω_z) or even one of the combined modes in a Coulomb crystal. The harmonic motion will modulate the frequency of the light in the ion's rest frame and give rise to sidebands spaced by the motional frequency ω_z . If these sidebands coincide with the transition frequency ($\omega_l = \omega_a \pm \omega_z$), the ion will absorb light. These so-called sideband transitions will affect the motion of the ion.

The interaction Hamiltonian of this system is still equivalent to the matrix in Equation 3.5, but since \mathbf{x} is time-dependent, the elimination of $e^{i(\mathbf{k}\cdot\mathbf{x}+\phi)}$ is flawed. Instead, the off-diagonal elements should read $\Omega e^{\pm i(\mathbf{k}\cdot\mathbf{x}+\phi-\Delta t)}$. Combining this Hamiltonian with the motion of the ion from Equation 2.23 gives

$$H_i = \frac{\hbar}{2}\Omega(|g\rangle\langle e|e^{-i(\eta[\hat{a}u^*(t)+\hat{a}^\dagger u(t)]-\Delta t+\phi)} + |e\rangle\langle g|e^{i(\eta[\hat{a}u^*(t)+\hat{a}^\dagger u(t)]-\Delta t+\phi)}) \quad (3.13)$$

where $\eta = \mathbf{k} \cdot \mathbf{x}_0 = \mathbf{k} \cdot \hat{\mathbf{x}} \sqrt{\frac{\hbar}{2m\omega_z}}$ is the so-called Lamb-Dicke parameter. The Lamb-Dicke parameter is a measure of the ratio between the recoil energy (of the ion due to photon emission) and the energy separation of the motional states ($\eta = \sqrt{E_{rec}/\hbar\omega_z}$), and it can be interpreted as a measure of the ability of excitation and emission events to change the motional state of the ion. To realize the time dependence of the Hamiltonian, the exponent can be expanded in Lamb-Dicke parameter around $\eta = 0$ to yield⁵

$$e^{i(\phi+\Delta t)} \sum_{m=0}^{\infty} \frac{(i\eta)^m}{m!} \left(\hat{a}^\dagger e^{i\beta\Omega_{\text{rf}}/2} \sum_{n=-\infty}^{\infty} C_{2n} e^{in\Omega_{\text{rf}}t} + \text{h.c.} \right)^m, \quad (3.14)$$

where h.c. denotes the hermitian conjugate of the preceding term. When the detuning satisfies $\Delta \approx (m\beta + n)\Omega_{\text{rf}}$, with n and m as integers, two of the terms in the Hamiltonian will be oscillating slowly. These terms will dominate the contribution to the time evolution of the coefficients, and the rest can be neglected in a second application of the rotating wave approximation. One can then talk about tuning to the n' 'th micro-motional- and m' 'th secular sideband. The frequency in the first exponential term, $\beta\Omega_{\text{rf}}/2$, may be recognized as the fundamental frequency of the trap, ω_0 from Section 2.1.1. Normally, the RF-sidebands are not addressed, and should be highly suppressed if the ion is in the middle of the trap. In that case, the terms containing $e^{in\Omega_{\text{rf}}t}$ with $n \neq 0$ can be neglected, and the entire Hamiltonian can be written as

$$H_i \simeq \frac{\hbar}{2}\Omega_0|e\rangle\langle g| \sum_{m=0}^{\infty} \frac{(i\eta)^m}{m!} (\hat{a}e^{-i\omega_z t} + \hat{a}^\dagger e^{i\omega_z t})^m e^{i(\phi-\Delta t)} + \text{h.c.}, \quad (3.15)$$

with $\Omega_0 = \Omega C_0 = \Omega/(1 + q/2)$. The expansion shows a series of terms with combinations of $|e\rangle\langle g|$ and $|g\rangle\langle e|$ with k \hat{a} - and l \hat{a}^\dagger -operators oscillating at a frequency $(k-l)\omega_z = s\omega_z$. Choosing a detuning of $\Delta \approx s\omega_z$ makes these combinations resonant and effectively couples the manifolds $|g, n\rangle \leftrightarrow |e, n+s\rangle$. Transitions with $s > 0$ ($s < 0$) are normally referred to as *blue* (*red*) *sidebands* and the transition for $s = 0$ the *carrier*.

If the laser is tuned to a resonance, so only two levels are coupled by the laser, and that $\Omega \ll \Delta$ for all other atomic and motional levels, the results

⁵ Note that the RF frequency of the trap is now denoted Ω_{rf} to avoid confusion with the Rabi-frequency Ω .

from the last section will still be applicable. Using the interaction Hamilton, Equation 3.3, on the product states yield:

$$\langle g, n | H_i | e, n + s \rangle = \frac{\hbar}{2} \Omega e^{i(\phi - \omega t)} \langle n | e^{i(\mathbf{k} \cdot \mathbf{x})} | n + s \rangle \quad (3.16)$$

We can then use the effective Rabi frequency $\Omega_{n, n+s} = \Omega_0 \langle n | e^{i(\mathbf{k} \cdot \mathbf{x})} | n + s \rangle$ to describe the system in the framework developed earlier. Rewriting this equation shows that the change in Rabi frequency comes from the wave-function overlap of the states in momentum space, separated by the photon momentum $\hbar k$, and can be pictured as a constraint of conservation of momentum [47]. The effective Rabi-frequency is given by [38]

$$\begin{aligned} \Omega_{n, n+s} &= \Omega_{n+s, n} = \Omega_0 \langle n + s | e^{i\eta(a + a^\dagger)} | n \rangle \\ &= \Omega_0 e^{-\eta/2} \eta^{|s|} \sqrt{\frac{n_{<}!}{n_{>}!}} L_{n_{<}}^{|s|}(\eta^2), \end{aligned} \quad (3.17)$$

where $n_{<}$ is the lesser of n and $n + s$ and $L_n^\alpha(X)$ is the generalized Laguerre Polynomial, $L_n^\alpha(X) = \sum_{m=0}^n (-1)^m \binom{n+\alpha}{n-m} \frac{X^m}{m!}$. This equation can be simplified greatly in the Lamb-Dicke regime.

3.2.1 The Lamb-Dicke Regime

The Lamb-Dicke regime is defined as the limit where the spread of the motional wave function is much less than the wavelength of the light, that is $\langle n | r^2 | n \rangle \ll 1/k$. Combining Equation 2.22 with the definition of η , it is observed that this limit is satisfied when $\eta \sqrt{2n+1} \ll 1$. Calculating the terms in Equation 3.15 makes it clear that this constraint means that the contribution from the second (and higher) order terms are negligible. In that case, the interaction Hamiltonian can be written as:

$$H_{LD} = \frac{\hbar}{2} \Omega_0 |e\rangle \langle g| \left(1 + i\eta (\hat{a} e^{-i\omega_z t} + \hat{a}^\dagger e^{i\omega_z t}) \right) e^{i(\phi - \Delta t)} + \text{h.c.} \quad (3.18)$$

This Hamiltonian contains only three resonances, the carrier and the first red and blue sidebands. The resonances couple different motional levels e.g., the Hamiltonian for the resonance at $\Delta = -\omega_z$ shows a combination of $\hat{a} |e\rangle \langle g|$ and $\hat{a}^\dagger |g\rangle \langle e|$, hence coupling the manifolds $|g, n\rangle \leftrightarrow |e, n-1\rangle$. The relevant parameters for the three transitions are shown in Table 3.1. These transitions will be important when discussing sideband cooling in Section 4.2.

3.3 The Secular Motion as a State Mediator

From the last sections it is clear that the interaction between light and trapped ions strongly depends on the motional state. We will now take a brief look at

Δ	Hamiltonian	Ω	Transitions
0	$H_{car} = \frac{\hbar}{2}\Omega_0(e\rangle\langle g + g\rangle\langle e)$	Ω_0	$ g, n\rangle \leftrightarrow e, n\rangle$
$-\omega_z$	$H_{rsb} = \frac{\hbar}{2}\Omega_0\eta(\hat{a} e\rangle\langle g + \hat{a}^\dagger g\rangle\langle e)$	$\Omega_0\eta\sqrt{n}$	$ g, n\rangle \leftrightarrow e, n-1\rangle$
$+\omega_z$	$H_{bsb} = \frac{\hbar}{2}\Omega_0\eta(\hat{a}^\dagger e\rangle\langle g + \hat{a} g\rangle\langle e)$	$\Omega_0\eta\sqrt{n+1}$	$ g, n\rangle \leftrightarrow g, n+1\rangle$

Table 3.1: Parameters for the motional transitions in the Lamb-Dicke limit.

how this can be exploited to transfer information between co-trapped ions in two different regimes.

As mentioned in the introduction, one way to realize spectroscopy of ions lacking cycling transitions is to use quantum logic to transfer state information between a *spectroscopy* ion and a co-trapped *auxiliary* ion [19]. In this description, the ions will be treated as simple two level systems with an excited state, $|e\rangle$, and a ground state, $|g\rangle$. The combined state of the system is then: $|g\rangle_s|g\rangle_a|n\rangle_m$, where s and a denotes the *spectroscopy* and *auxiliary* ion and m the motional state. If the system starts in the combined ground state $\psi_0 = |g\rangle_s|g\rangle_a|0\rangle_m$, and the *spectroscopy* ion is subsequently excited on the carrier, the new state will be of the form:

$$\psi_1 = (\alpha|g\rangle_s + \beta|e\rangle_s)|g\rangle_a|0\rangle_m, \quad (3.19)$$

where $|\alpha|^2 + |\beta|^2 = 1$. By applying a π -pulse on the red sideband of the *spectroscopy* ion, the new state becomes:

$$\psi_2 = (\alpha|g\rangle_s|0\rangle_m + \beta|g\rangle_s|1\rangle_m)|g\rangle_a. \quad (3.20)$$

The $\alpha|g\rangle_s|0\rangle_m$ part of the wave-function is unaffected because the the red sideband transition does not exist in the ground state. With a π -pulse on the red sideband of the *auxiliary* ion, the final state becomes:

$$\psi_3 = |g\rangle_s(\alpha|g\rangle_a + \beta|e\rangle_a)|0\rangle_m. \quad (3.21)$$

The state of the *spectroscopy* ion is now mapped onto the *auxiliary* ion. This state can be determined with typical procedures as explained in Chapter 5. Quantum logic is a powerful tool, as it provides the ability to determine the original state of the *spectroscopy* ion and hence study coherent dynamics; a tool which has already been utilized to probe a clock transition in $^{27}\text{Al}^+$ using a $^9\text{Be}^+$ *auxiliary* ion [20].

One limitation of spectroscopy with quantum logic is that it requires long-lived states; at least on the time scale of the coherent manipulations. For states with a short life time, full coherent mapping is not possible, but it is possible to realize spectroscopy with a similar technique. Let us initially assume again that the motion is cooled to the quantum mechanical ground

state. In this case, the red sidebands disappear. If one of the ions (the *spectroscopy* ion) scatters a photon on the blue sideband, the motion is excited by a single quantum. Because both ions participate in this motion, this also means that the red sideband appears on the second ion (the *auxiliary* ion); by probing the red sideband of the *auxiliary* ion, it is possible to detect scattering events on the *spectroscopy* ion. This technique does not provide the full state information as quantum logic does, but it enables spectroscopy of co-trapped ions in a simple way without requiring coherent manipulation; we will refer to this idea as Sympathetic Recoil Spectroscopy (SRS).

Utilizing heating to detect scattering event on co-trapped ions has been demonstrated earlier [48]. This demonstration did however rely on significant heating to detect a change in fluorescence during Doppler re-cooling. With initial ground state preparation, significantly fewer scattering events are required for detection.

For a short-lived state, the motional sidebands will typically be unresolved ($\Gamma \gg \omega$). In the ground state, scattering will primarily happen on the carrier and first blue sideband. From Table 3.1, we see that for each photon scattered on the carrier, we expect η^2 scattered photons on the blue sideband; events which increases the motional state by 1 quantum. By reading out the motional state with the *auxiliary* ion, it is possible to identify these scattering events and thereby detect transitions in the *spectroscopy* ion.

In principle, SRS does not provide more knowledge than usual spectroscopy does, the main feature is that it provides the high precision of single ion spectroscopy together with a high detection efficiency. With typical operating conditions as described in Chapter 14, realizing a recoil kick from 400 nm photons only requires ~ 18 scattering events on average; realizing the same collection efficiency by detecting the scattered photons is not a trivial task.

Cooling of Trapped Ions

In experiments with trapped ions, the ions are often obtained from an atomic beam, evaporated in an oven at high temperature $\sim 500^\circ\text{C}$. The ions therefore have a high kinetic energy, typically around 0.05 eV at the moment of ionization. Compared to the spacing of the motional levels around 10^{-9} eV, this results in a high average quantum number, and the ions must be cooled to a lower motional state.

There exist a number of different techniques to reduce the kinetic energy of the ions, including resistive cooling, collisional cooling and cooling by inelastic scattering of laser light, but only the latter makes it possible to cool to the ground state.¹ Methods for cooling ions with laser light are often separated into two limiting regimes:

$\omega_z \ll \Gamma$ If the secular frequency, ω_z , is lower than the decay rate, Γ , for the transition used for cooling, the timescale on which the velocity of the ion changes will be smaller than the time it takes to emit and absorb photons. In this case, the ion acts as a free particle with a time-modulated Doppler shift of the cooling light. A velocity dependent radiation pressure can then be used to cool the particle. This type of cooling is often termed Doppler cooling.

$\omega_z \gg \Gamma$ In the opposite case, the linewidth of the transition will be smaller than the separation of the motional levels, and distinct sidebands appear. If the laser is tuned so the energy of the absorbed photons is less than the energy of spontaneously emitted photons, the energy of the ion will be reduced. This type of cooling is called sideband cooling.

¹ See for example [37] or [49] for a description of the different cooling techniques.

The complementary dynamics of these two regimes can be used to cool ions to the ground state.

When ions are trapped from a thermal beam, they have a high number of motional excitations, and many photons must be scattered to cool the ions to the ground state; a high scattering rate is advantageous. A high scattering rate can be realized on a dipole allowed transition, for example the $S_{1/2} \leftrightarrow P_{1/2}$ transition in $^{40}\text{Ca}^+$ with $\Gamma = 2\pi \cdot 20.7 \text{ MHz}$. A typical trap frequency around $\omega_z \sim 2\pi \cdot 0.5 \text{ MHz}$ results in $\omega \ll \Gamma$, and it is not possible to cool the ion to the ground state. The second regime, $\omega \gg \Gamma$, can be realized on the dipole forbidden $S_{1/2} \leftrightarrow D_{5/2}$ transition with $\Gamma = 2\pi \cdot 0.15 \text{ Hz}$. On this transition, it is possible to reach the ground state, but the scattering rate will be much lower. Cooling to the ground state therefore normally employs both types of cooling. The following two sections are focused on describing the dynamics of these different cooling techniques.

4.1 Doppler Cooling

In the limit where $\omega_z \ll \Gamma$, the timescale, on which the ion absorbs and emits photons, is much shorter than the timescale on which the ion changes its velocity. The ion can then be considered as free regarding the interaction process. We consider the free ion illustrated in Figure 4.1.

Let the ion absorb a photon with wave vector \vec{k}_l and subsequently spontaneously emit a photon with wave vector \vec{k}_s , thereby changing the velocity of the ion from \vec{v} to \vec{v}_2 . Conservation of momentum and kinetic energy gives the equations:

$$\begin{aligned} m\vec{v} + \hbar\vec{k}_l &= m\vec{v}_2 + \hbar\vec{k}_s \\ \frac{1}{2}mv^2 + \hbar\omega_l &= \frac{1}{2}mv_2^2 + \hbar\omega_s \end{aligned} \quad (4.1)$$

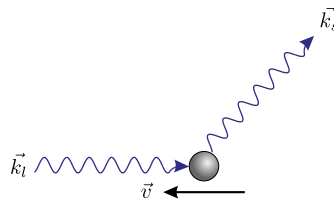


Figure 4.1: Scattering of photons during Doppler cooling. The ion travels towards the laser source and absorbs a photon with wave vector \vec{k}_l . Later, the ion spontaneously emits a photon with wave vector \vec{k}_s , overall reducing the velocity, \vec{v} , of the ion.

Combining these two equations gives:

$$\Delta E_{kin} = \hbar \vec{v} \cdot (\vec{k}_l - \vec{k}_s) + \frac{\hbar^2}{2m} (\vec{k}_l^2 + \vec{k}_s^2 - 2(\vec{k}_l \cdot \vec{k}_s)) + \hbar(\omega_l - \omega_s) \quad (4.2)$$

The average change in kinetic energy per scattering event in the direction of the beam (\vec{k}_l) can, with the assumption $k_l \approx k_s = k$, be written as

$$\langle \Delta E_{kin} \rangle = \hbar \vec{v} \cdot \vec{k}_l + \frac{\hbar^2 k^2}{2m} (1 + \kappa), \quad (4.3)$$

where κ accounts for the probability of photon emission in the given direction. In the case of isotropic emission, κ would be 1/3. The derivative of the energy must be given by the energy change per scatter event multiplied by the scattering rate, $\Gamma \rho_{ee}$. Averaging over a lot of scattering events, the average change in energy is:

$$\frac{dE_{kin}}{dt} = \left\langle \left(-\hbar v k_l + \frac{\hbar^2 k^2}{2m} (1 + \kappa) \right) \Gamma \rho_{ee} \right\rangle_v \quad (4.4)$$

In the final part of the cooling, where the Doppler broadening is much less than the natural linewidth of the transition, a Taylor-expansion of ρ_{ee} around $v = 0$ can be applied. Equation 3.10 with the Doppler shift included gives (discarding terms of 2nd order and higher):

$$\Gamma \rho_{ee} \approx \Gamma \rho_{ee}(v = 0) + \Gamma \left. \frac{d\rho_{ee}}{dv} \right|_{v=0} v = \frac{\hbar k \Gamma \Omega^2}{\Gamma^2 + 4\Delta^2} + \frac{8\Omega^2 \Delta k}{(\Gamma^2 + 4\Delta^2)^2} v \quad (4.5)$$

Keeping in mind that the force on the ion is given by the change in momentum per unit time ($F = \hbar k \Gamma \rho_{ee}$), it is observed that the linearization around $v = 0$ gives a force of the form $F = F_0 + \alpha v$. This is a viscous drag that will slow down the ion. This equation was derived for a free ion. For an ion bound in a trap, it can be assumed that the probability distribution of the velocity is the same in each direction ($P(\vec{v}) = P(-\vec{v})$), so that $\langle v \rangle_v = 0$. Combining Equation 4.4 and Equation 4.5 then gives:

$$\frac{dE_{kin}}{dt} = \frac{8\Omega^2 \Delta \hbar k^2}{(\Gamma^2 + 4\Delta^2)^2} \langle v^2 \rangle_v + \frac{\Gamma \Omega^2}{\Gamma^2 + 4\Delta^2} \frac{\hbar^2 k^2}{2m} (1 + \kappa) \quad (4.6)$$

The first term is the viscous drag as discussed before, which will give rise to cooling when $\Delta < 0$. The second term is always positive and will heat the ion. The second term comes from the discrete nature of the process. Whenever a photon is emitted, the ion recoils and changes its kinetic energy. Even though the recoil kicks averages out to give a mean momentum $\langle p \rangle = 0$, this discrete process gives rise to a random walk in momentum space. This

means that the ion is always moving and does not come to a complete stop. This random walk in momentum space is what sets the lower bound of the cooling process.² In steady state, the change in energy must be zero. Solving the equation for $\langle v^2 \rangle_v$, the kinetic energy in steady state can be written as:

$$E_{kin} = \frac{1}{2}m\langle v^2 \rangle_v = \frac{\hbar(\Gamma^2 + 4\Delta^2)}{32\Delta}(1 + \kappa) \quad (4.7)$$

This value is minimized for $\Delta = \Gamma/2$ and gives:

$$E_{kin} = \frac{\hbar\Gamma}{8}(1 + \kappa) \quad (4.8)$$

If the temperature, T , of the ion is defined through its kinetic energy from the equipartition theorem, $m\langle v^2 \rangle = k_B T$, where k_B is the Boltzmann constant and T the absolute temperature, the corresponding Doppler temperature is given by:

$$k_B T_D = \frac{\hbar\Gamma}{4}(1 + \kappa) \quad (4.9)$$

With laser light from all 3 direction in space, κ will be equal to 1, and the equation reduces to the usual Doppler limit: $k_B T_D = \hbar\Gamma/2$. With only one cooling beam perpendicular to the quantization axis, κ will be 2/5 for an electric dipole transition [51], which gives a lower Doppler limit of $k_B T = \hbar\Gamma 5/4$. This lower limit (than for isotropic scattering) can be understood from the fact that only one direction has been treated in this derivation. The parameter η accounts for photons emitted along the axis of choice, hence $1 - \eta$ photons are emitted in the perpendicular directions, which gives rise to heating. The ion is then cooled to a lower state in the chosen direction but heated in the other two directions.

For a 3-dimensional harmonic oscillator (like the linear Paul trap), the ion can be cooled in all 3 dimensions with a single laser beam. This is done by choosing the angle of the laser beam so \vec{k}_l has a finite overlap with all the principal axes; thereby cooling the ion in all 3 dimensions. This requires, however, that all the motional frequencies (Ω_x , Ω_y and Ω_z) are different on a timescale set by the cooling time. Pointing the laser beam at angle of 45° to all the principal axes will result in the normal Doppler limit ($\hbar\Gamma/2$).

Cooling of a single $^{40}\text{Ca}^+$ ion on the $S_{1/2} \leftrightarrow P_{1/2}$ dipole transition results in $T_D = 0.5$ mK, which for a trap potential with frequency $\omega_z = 2\pi \cdot 0.5$ MHz corresponds to $\langle n \rangle \sim 20$. The ion has been cooled from ~ 0.05 eV to only $\sim 4 \cdot 10^{-8}$ eV, but a little energy remains before the ground state is reached.

² Actually there are two terms contributing to the heating ($1 + \kappa$). The κ -term comes from the random walk due to the recoil of the emission process, whereas the "1"-part comes from the random walk in momentum space due to the discreteness of the absorption process. See [50, p. 63] or [46, p. 188] for a description of these contributions.

4.2 Sideband Cooling

Removing the last few quanta is not possible on a broad dipole transition where $\omega_z \ll \Gamma$, but when ω_z becomes larger than Γ (and the laser linewidth), distinct motional sidebands appear. These can be used to further reduce the temperature of the ion below the Doppler limit.

If a laser is addressed to the lower motional sideband of an atomic transition, each excitation to the upper level is accompanied by a reduction in the motional quantum number. In the Lamb-Dicke limit, decay from the excited state will primarily happen on the carrier, giving rise to a net cooling during a cycle. This cooling can continue until the ground state is reached, where excitation on the red sideband is no longer possible as illustrated in Figure 4.2. Without any competing heating effects, the ion is cooled to the ground state and trapped here.

In this simple model, each cooling cycle contains a spontaneous decay to the electronic ground state, and coherence never plays a strong role. The system can then be treated with rate equations.

The Rate Equation Model

How fast the ion is cooled depends on the scattering rate. Each cycle removes one motional quanta, hence the cooling rate must be given as the product of the decay rate, Γ , and the occupation of the upper level, ρ_{ee} . The cooling rate can be calculated with Equation 3.10 and the transition strength on the red sideband from Table 3.1 to give:

$$R_n = \Gamma \rho_{ee} = \Gamma \frac{|\Omega|^2/4}{\delta^2 + |\Omega|^2/2 + \Gamma^2/4} = \Gamma \frac{(\Omega\eta\sqrt{n})^2}{2(\Omega\eta\sqrt{n})^2 + \Gamma^2} \quad (4.10)$$

When the ion reaches the ground state ($n = 0$), the cooling vanishes as expected, and ideally no further excitations occur. In reality, non-resonant excitations will prevent the ground state from being a perfect 'dark state' and

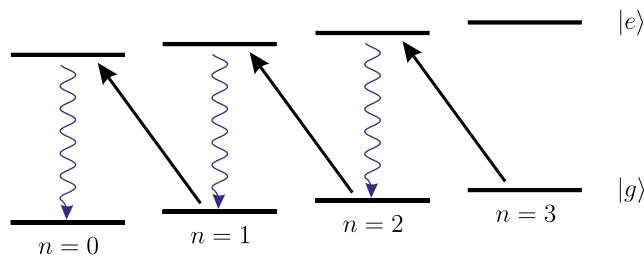


Figure 4.2: Sideband cooling: Each excitation is accompanied by a decrease in the motional quantum number.

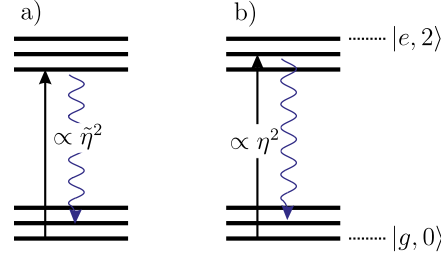


Figure 4.3: Primary heating processes. (a) Absorption on the carrier, re-emission on the blue sideband. (b) Absorption on the blue sideband, re-emission on the carrier.

impose a lower limit on the cooling. Since the coupling strength scales as $\eta^{|\Delta n|}$, transitions on the second sideband in the Lamb-Dicke regime are unlikely; they will be suppressed by a factor η^4 . Two heating processes exist on the first blue sideband as illustrated in Figure 4.3.

The first process starts with excitation on the carrier and re-emission on the blue sideband, the second with absorption on the blue sideband and re-emission on the carrier. Sideband cooling depends on distinct sidebands, hence it is a good approximation that $\Gamma, \Omega \ll \omega_z$. If the final part of the cooling is considered, population in other states than $n = 0$ and $n = 1$ can be neglected. From the coupling strengths in Table 3.1 and the population in the upper level from Equation 3.10, the two heating rates can be written as

$$\begin{aligned} R_1 &= p_0 \frac{\Omega^2/4}{\omega_z^2} \Gamma \tilde{\eta}^2 \\ R_2 &= p_0 \frac{\eta^2 \Omega^2/4}{(2\omega_z)^2} \Gamma, \end{aligned} \quad (4.11)$$

where p_0 is the population in $n = 0$. Note that the Lamb-Dicke factor for spontaneous decay, $\tilde{\eta}$, is different from the Lamb-Dicke factor for absorption, η . This is because the emission process is not limited to the same direction as the absorption process. In a three-level cooling scheme, as discussed later, the emission wavelength can further be different from the absorption wavelength. Combining these rates with the cooling rate from Equation 4.10 gives the change in populations:

$$\begin{aligned} \frac{dp_0}{dt} &= p_1 \frac{\Gamma(\eta\Omega)^2}{2(\eta\Omega)^2 + \Gamma^2} - p_0 \frac{\Omega^2/4}{\omega^2} \Gamma \tilde{\eta}^2 - p_0 \frac{\eta^2 \Omega^2/4}{(2\omega)^2} \Gamma \\ \frac{dp_1}{dt} &= -\frac{dp_0}{dt} \end{aligned} \quad (4.12)$$

In the regime with only two motional levels, the mean quantum number, $\langle n \rangle$, is equal to the population in the first motional state ($\langle n \rangle = p_1$). Solving the

differential equations with this relation gives an equation of the form

$$\langle n \rangle = n_{ss} + (n_0 - n_{ss})e^{-Wt}, \quad (4.13)$$

where n_0 is the mean quantum number at $t = 0$. The cooling rate, W , depends on the parameters of Equation 4.12. With the earlier assumptions applied, this is given by:

$$W = \frac{\Gamma\eta^2\Omega^2}{2\eta^2\Omega^2 + \Gamma^2} \quad (4.14)$$

The steady state quantum number, n_{ss} , is found by setting $dp_i/dt = 0$, which with the same assumptions gives:

$$n_{ss} = \frac{\frac{\Omega^2/4}{\omega_z^2}\Gamma\tilde{\eta}^2 + \frac{\eta^2\Omega^2/4}{(2\omega_z)^2}\Gamma}{\frac{\Gamma\eta^2\Omega^2}{2\eta^2\Omega^2 + \Gamma^2}} \quad (4.15)$$

In the limit where $\eta\Omega \ll \Gamma$, this reduces to:

$$n_{ss} \approx p_1 \approx \frac{\Gamma^2}{4\omega_z^2} \left(\frac{\tilde{\eta}^2}{\eta^2} + \frac{1}{4} \right) \quad (4.16)$$

The steady state value, n_{ss} , is limited by off-resonant scattering. In the limit where $\omega_z \gg \Gamma$, off-resonant scattering becomes negligible, and the ion can be cooled to the ground state with high probability ($\langle n \rangle \approx 0$).

With no external heating mechanisms, only off-resonant excitation on unwanted sidebands can keep the ion from being cooled to the ground state.

Ground state cooling requires $\omega \gg \Gamma$. To obtain this on a dipole allowed optical transition (Γ often tens of MHz) requires a very tightly confining trap. Instead, quadrupole or Raman transitions are often used. An experimental limitation of these transitions is the natural decay rate. Electric quadrupole transitions typically have a decay rate of a few decays per second, limiting the cooling rate dramatically. In this case, coupling the upper level to an auxiliary short-lived level can increase the cooling rate. The resulting decay-rate is in the limit of low saturation given by [52]

$$\Gamma' = \frac{\Omega_{aux}^2}{(\Gamma_{aux} + \Gamma_{nat})^2 + 4\Delta_{aux}^2} \Gamma_{aux}, \quad (4.17)$$

where Γ_{nat} is the natural decay rate, Γ_{aux} the decay rate of the auxiliary level and $\Omega_{aux}, \Delta_{aux}$ are parameters of the auxiliary light field.

The narrow quadrupole transition ($S_{1/2} \leftrightarrow D_{5/2}$) in $^{40}\text{Ca}^+$ has a natural decay rate of $\Gamma = 2\pi \cdot 0.15 \text{ Hz}$. To achieve a higher cooling rate, the upper level can be broadened by coupling it to $P_{3/2}$ which has a natural decay rate of $\Gamma = 2\pi \cdot 21.5 \text{ MHz}$. As long as $\omega_z \ll \Gamma' \approx \Omega^2/\Gamma_{aux}$, ground state cooling

is possible. This has been done by Roos et al. with a resulting final ground state occupation of 99.9% [53]. The first report of ground state cooling in 1988 by the group at NIST, USA, used similar transitions to cool a single trapped $^{198}\text{Hg}^+$ to the ground state with 95% probability [54].

4.3 Determination of the Motional State

Investigating cooling experimentally requires a method to determine the the motional state. This can be realized in several ways depending on the number of excitations. If the ion is in the ground state with a reasonable probability, one method is to compare the strength of the red and blue motional sidebands. When the ion is in the ground state, driving the red sideband does not transfer any population, whereas driving the blue sideband does. By comparing the excitation on the sidebands, the occupation of the ground state can be determined.

4.3.1 Excitation on the Red Sideband

After cooling, the average number of motional excitations, $\langle n \rangle$, is expected to follow a thermal Maxwell-Boltzmann distribution given by [38]:

$$P_n = \frac{\langle n \rangle^n}{(\langle n \rangle + 1)^{n+1}} \quad (4.18)$$

Assume that the ion initially is in the electronic ground state and a thermal motional state, $|\psi\rangle = |g\rangle \sum_{n=0}^{\infty} c_n |n\rangle$ with $|c_n|^2 = P_n$. If a pulse of length t is applied on the red sideband, the probability of finding the ion in the state $|e\rangle$ must be:

$$\rho_{\text{RSB}} = \sum_{n=1}^{\infty} \frac{\langle n \rangle^n}{(\langle n \rangle + 1)^{n+1}} \sin^2(\Omega_{n,n-1}t/2) \quad (4.19)$$

This population can be measured experimentally using the shelving technique described in Section 5.3. A similar calculation for a pulse on the blue sideband gives:

$$\rho_{\text{BSB}} = \sum_{n=0}^{\infty} \frac{\langle n \rangle^n}{(\langle n \rangle + 1)^{n+1}} \sin^2(\Omega_{n,n+1}t/2) \quad (4.20)$$

The ratio between the excitation on the two sideband can be calculated to yield:

$$\frac{\rho_{\text{RSB}}}{\rho_{\text{BSB}}} = \frac{\langle n \rangle}{\langle n \rangle + 1} \Leftrightarrow \langle n \rangle = \frac{\rho_{\text{RSB}}}{\rho_{\text{BSB}} - \rho_{\text{RSB}}}, \quad (4.21)$$

or:

$$P_0 = 1 - \frac{\rho_{\text{RSB}}}{\rho_{\text{BSB}}} \quad (4.22)$$

This technique relies on the fact that the population in the motional ground state is not transferred when a pulse is applied on the red sideband; for this to work, the ion must be in the ground state with a reasonable probability. This is observed in the equation where the strength of the sidebands become equal for large $\langle n \rangle$. To measure the population distribution for higher $\langle n \rangle$ requires different techniques.

4.3.2 Rabi Oscillations on Motion-Sensitive Transitions

An alternative way to determine the motional distribution is to investigate Rabi oscillations on a motion-sensitive transition. A finite Lamb-Dicke parameter, η , implies that the coupling strength, $\Omega_{n,n+s}$, depends on the motional state of the ion as illustrated in Figure 4.4. This dependence provides a way to map the motional state of the ion onto the internal state.

Assume again that the ion is in the initial state $|\psi\rangle = |g\rangle \sum_{n=0}^{\infty} c_n |n\rangle$. If the carrier of the $|g\rangle \leftrightarrow |e\rangle$ transition is driven for a period t , the population of $|e\rangle$, ρ_{ee} , will depend on t . With Equation 3.6, the population distribution after the pulse can be calculated and gives the following probability of finding the ion in the state $|e\rangle$:

$$\rho_{ee}(t) = \frac{1}{2} \left(1 - \sum_{n=0}^{\infty} |c_n|^2 \cos(\Omega_{n,n} t / 2) \right) \quad (4.23)$$

An example of the resulting signal is shown in Figure 4.5. The oscillation appear damped due to interference between the different frequencies $\Omega_{n,n}$. This measurement can be performed on a sideband of choice, and typically the blue sideband is chosen due to the high slope at low excitations. At high

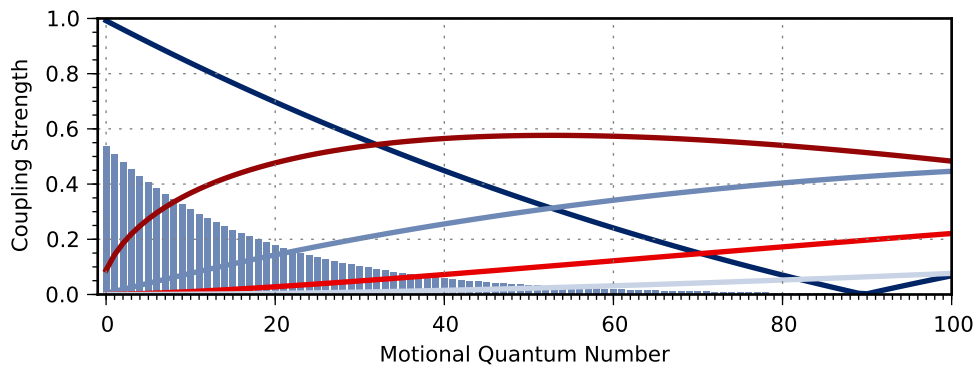


Figure 4.4: Relative coupling strength according to Equation 4.21 for different motional quantum numbers. — Carrier; — 1st red sideband; — 2nd; — 3rd; — 4th for $\eta = 0.127$. The bars in the background (scaled $\times 10$) indicate the thermal occupation for a temperature of 0.5 mK (Doppler Limit, $\langle n \rangle = 17$) with $\omega_z = 2\pi \cdot 585$ kHz .

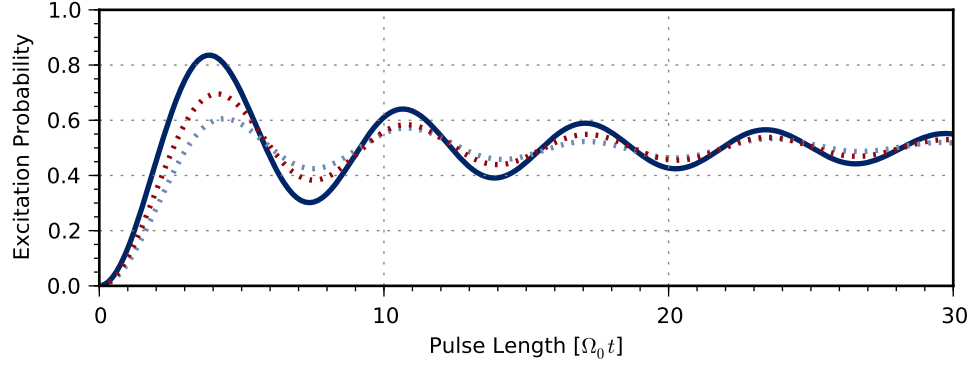


Figure 4.5: Rabi oscillations on the motional carrier with $\eta = 0.127$ for thermal distributions with: $\color{blue}\blacksquare$ $\langle n \rangle = 20$; $\color{red}\blacksquare$ $\langle n \rangle = 35$ and $\color{blue}\blacksquare$ $\langle n \rangle = 50$.

values of $\langle n \rangle$, the carrier is a better choice as the strength of the first sideband is rather constant at high excitations. In this case, the population is spread across many states, and it is necessary to assume a thermal distribution. At low values of $\langle n \rangle$, however, the dephasing method is a very rich tool, as it provides a possibility to determine the occupation of the individual motional states, $|c_n|^2$, by Fourier transforming the signal.

4.3.3 Sideband Strength Comparison

Outside the Lamb-Dicke limit, higher order sidebands starts to appear (see [Figure 4.4](#)). In this regime, the strength of the higher order sidebands can provide information on the motional state of the ion. Opposed to the previous two, this technique always requires a model for the motional distribution; this is clarified by using the temperature, T , as a variable in stead of $\langle n \rangle$. We start by assuming a thermal Maxwell-Boltzmann distribution:

$$P_n = \frac{e^{-(n+\frac{1}{2})\hbar\omega/k_B T}}{Z(T)}, \quad (4.24)$$

where $Z(T)$ is the partition function. With this distribution in mind, we can calculate the expected average excitation on the s 'th sideband for a pulse with length t from [Equation 3.6](#) and [Equation 3.17](#) to:

$$\rho_{ee} = \sum_{n=0}^{\infty} P_n \sin^2(\Omega_{n,n+s} t / 2) \quad (4.25)$$

Due to different Rabi frequencies between the different motional levels, this gives rise to a unique combination of sideband excitations depending on the motional temperature as illustrated in [Figure 4.6](#).

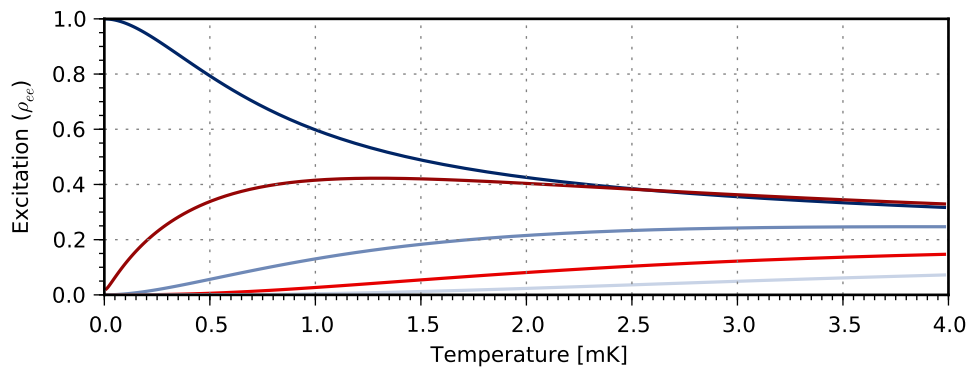


Figure 4.6: Average strength of sidebands for different temperatures according to Equation 4.25 with $\omega_z = 2\pi \cdot 585$ kHz, $\eta = 0.127$. The pulse length is set to match a perfect π -pulse on the carrier in the ground state (evident by unity excitation). ■ Carrier; ■ 1st red sideband; ■ 2nd; ■ 3rd; ■ 4th.

This technique can be a valuable tool for everyday evaluation of Doppler cooling; it only requires a rough scan around the sidebands to notice changes in the temperature of the ion.

Manipulating the $^{40}\text{Ca}^+$ ion

Calcium belongs to the alkaline earth metals and has the electron configuration $[\text{Ar}] 4s^2$. The singly charged Ca^+ ion has a single electron outside the closed shells, and can for most purposes be considered as a one-electron atom. The diagram of the five lowest levels of $^{40}\text{Ca}^+$ is shown in Figure 5.1.

These transitions can be used to cool the ion by the techniques described in Chapter 4. Doppler and sideband cooling of the $^{40}\text{Ca}^+$ -ion will be described in the next sections along with a method to determine the internal state of the ion.

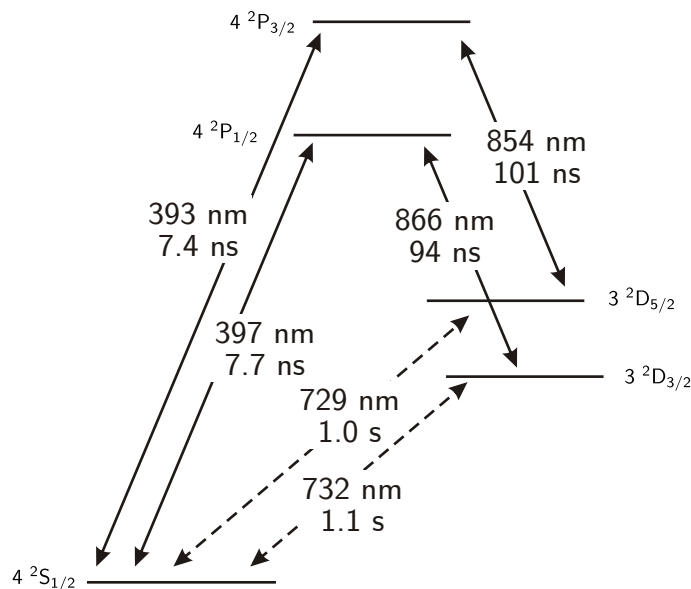


Figure 5.1: The five lowest levels of $^{40}\text{Ca}^+$ with transition wavelengths and lifetimes [55]. The solid arrows indicate dipole allowed transitions and the dashed arrows electric quadrupole transitions.

5.1 Doppler Cooling

The purpose of Doppler cooling is to remove a lot of kinetic energy. After trapping, the ion is extremely hot with $\langle n \rangle \sim 10^7$, and many motional quanta must be removed; a high scattering rate is preferred. This can be obtained by cooling on the dipole allowed transition, $S_{1/2} \leftrightarrow P_{1/2}$, which has a natural decay rate of $2\pi \cdot 20.7$ MHz. When the ion is in the $P_{1/2}$ state, it can decay to both $S_{1/2}$ and $D_{3/2}$. Decay to $D_{3/2}$ will interrupt the cooling as the lifetime of the $D_{3/2}$ level is long (1 s). This can be avoided by *repumping* on the $D_{3/2} \leftrightarrow P_{1/2}$ transition. The theory in Section 4.1 was developed for a closed system, but given that decay to $D_{3/2}$ only occurs 1 out of 12 cycles and the momentum of the infrared photon is roughly half the momentum of the blue photon, it is expected that the final temperature is given by the Doppler limit on the blue transition. Equation 4.9 then gives a final temperature of:

$$T_D = 0.5 \text{ mK} \quad (5.1)$$

For $\omega_z = 2\pi \cdot 500$ kHz, this temperature corresponds to $\langle n \rangle \sim 20$, and further cooling is needed to reach the ground state.

5.2 Sideband Cooling

Sideband cooling requires distinct motional sidebands. This can be realized on the narrow $S_{1/2} \leftrightarrow D_{3/2}$ or $S_{1/2} \leftrightarrow D_{5/2}$ quadrupole transitions with natural lifetimes of 1 s. The coupling strength on such transitions is significantly lower than on dipole allowed transitions and requires a significantly higher field strength. This is however readily available with commercial solid state laser systems. Either transition is perfectly suited for sideband cooling, but the $S_{1/2} \leftrightarrow D_{5/2}$ transition also provides the ability to easily discriminate between the two states. Due to the long life time of the $D_{5/2}$ level, a descent cooling rate requires broadening by coupling it to an auxiliary level. This can be achieved by driving the $D_{5/2} \leftrightarrow P_{3/2}$ transition at 854 nm. If this transition is driven strongly, the sideband resolution is compromised. This can be overcome by using a low power or using interleaved pulses with excitation on the $S_{1/2} \leftrightarrow D_{5/2}$ and subsequent repumping to the $S_{1/2}$ level via the $P_{3/2}$ level.

5.3 Detecting the Internal State

Trapped ions are often detected by light scattered during Doppler cooling. At saturation, a single ion can scatter many million photons every second, which makes it possible to detect the presence of the ion in short time. The

fluorescence can also be used to detect the internal state of the ion by a technique called *electron shelving*, suggested by Dehmelt in 1975.

The idea behind this technique is to ‘shelve’ the electron in a state in which it does not fluoresce, e.g. the metastable state $D_{5/2}$ in $^{40}\text{Ca}^+$. If the ion is in the electronic ground state and the $S_{1/2} \leftrightarrow P_{1/2}$ transition is driven, the ion will fluoresce from the scattered 397 nm photons. If the ion is in the $D_{5/2}$ state on the other hand, it will not fluoresce. The $D_{5/2}$ state has a lifetime of 1 s, which makes it possible to distinguish the states with high fidelity. On the narrow transition, it is possible to selectively transfer the ion depending on the motional state, and in this way the motional state can be mapped onto the internal state and read out.

Part II

Laser Stabilization

CHAPTER 6

Introduction

Probing dynamics on a narrow transition, like the 729 nm quadrupole transition in $^{40}\text{Ca}^+$, requires a laser with a narrow linewidth and absolute frequency stability. Typical grating stabilized diode lasers have linewidths of a few hundred kHz and can drift up to several MHz within a few minutes. This is too much to probe motional dynamics, and further stabilization is required.

One way to reduce the linewidth and improve the absolute stability is to continuously monitor the light and feed any frequency deviations back to the laser for adjustment. This technique requires a way to determine the absolute frequency. For work with neutral atoms, this can be realized by probing the intended atomic transition. Unfortunately, this is not possible for transitions in ions, and it is necessary to resort to other frequency references. One such reference is the optical resonator, which uses interference effects between two mirrors to discriminate wavelengths. If designed carefully, such a resonator can serve as a good frequency reference and be a valuable tool in laser stabilization. This part of the thesis is dedicated to describing a system utilizing such an optical resonator for stabilizing the short and long term frequency fluctuations of the laser. The first two chapters introduce the general theory of frequency discrimination with optical resonators and feedback loops, and after that, the actual design of the optical resonator and the electronic stabilization system is described in more detail.

There exist excellent literature on both feedback theory and laser stabilization. The link between these fields is, however, not always obvious. The first chapters are therefore not only intended to provide the required framework for the final chapters, but also as a brief introductory material for anyone interested in the practical aspects of laser stabilization. The discussion of control theory is brief but should hopefully provide enough insight to grasp the interplay between these fields and apply textbook control theory to laser stabilization.

Laser Stabilization using Optical Resonators

Laser stabilization using optical resonators can be realized in many different ways, but a common method to achieve low linewidth is the so-called Pound-Drever-Hall (PDH) technique. This chapter starts with an introduction to the optical resonator and the physics required to understand the PDH theory explained in the following section. Finally, a brief section provides a few important considerations for realizing a PDH lock in practice.

7.1 The Optical Resonator

The physics of the optical resonator can simply be described by interference effects between different reflections, but even so, it exhibits many interesting phenomena. This chapter will skip many of those phenomena explored in other experiments and focus on results necessary to understand the theory behind the PDH technique. The results will only be briefly summarized as they can be found in several textbooks on optics and lasers. The formulae stated here can be found in [56, sec. 5.5].

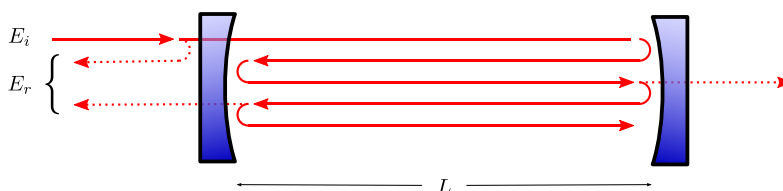


Figure 7.1: An optical resonator with two concave mirrors separated by a distance L .

An optical resonator consists of two mirrors separated by a distance L as illustrated in Figure 7.1. When light is incident on the entry mirror, a part of it is reflected and the rest leaks through and enters the resonator where it bounces back and forth between the front and back mirrors. The light is only resonant with the cavity if it interferes constructively after each round trip, that is, the optical length should match an integer number of wavelengths ($2L = N\lambda$). This gives rise to a frequency dependent transmission profile with a set of equidistant peaks as illustrated in Figure 7.2a. The separation between these peaks is termed the free spectral range given by

$$\nu_{\text{FSR}} = \frac{c}{2L}, \quad (7.1)$$

where c is the speed of light.¹ The width of the transmission peaks depend on the reflectivity of the mirrors. The ratio between this linewidth, $\nu_{1/2}$, and the free spectral range

$$\mathcal{F} = \frac{\nu_{1/2}}{\nu_{\text{FSR}}} \quad (7.2)$$

is termed the finesse. In the low loss limit, this finesse can be calculated as

$$\mathcal{F} = \frac{\pi r}{1 - r^2}, \quad (7.3)$$

where r is the amplitude-reflectivity of the mirrors.² The light leaking back out through the resonator will interfere with the directly reflected part, and depending on the detuning this introduces both a change in amplitude and phase given by

$$E_r = F(\omega)E_i, \quad F(\omega) = r \frac{1 - e^{i\delta}}{1 - r^2 e^{i\delta}}, \quad (7.4)$$

where E_i and E_r are the electric field amplitudes of the incident and reflected optical fields and $\delta = \omega/\nu_{\text{FSR}}$.³ This reflection coefficient is illustrated in Figure 7.2b (the frequency scale corresponds to a small range just around one of the resonances in Figure 7.2a). The imaginary part is antisymmetric and close to linear just around resonance and provides a good frequency reference for feeding back deviations. With the PDH technique described in the following section it is possible to extract this imaginary part.

¹ c should be corrected by the refractive index for propagation outside vacuum (c/n).

² It is important to note that r is reflectivity of the electric field amplitude, not the optical power, for which the reflection coefficient would be r^2 .

³ Be aware that ω is defined in angular frequency where as ν_{FSR} is not.

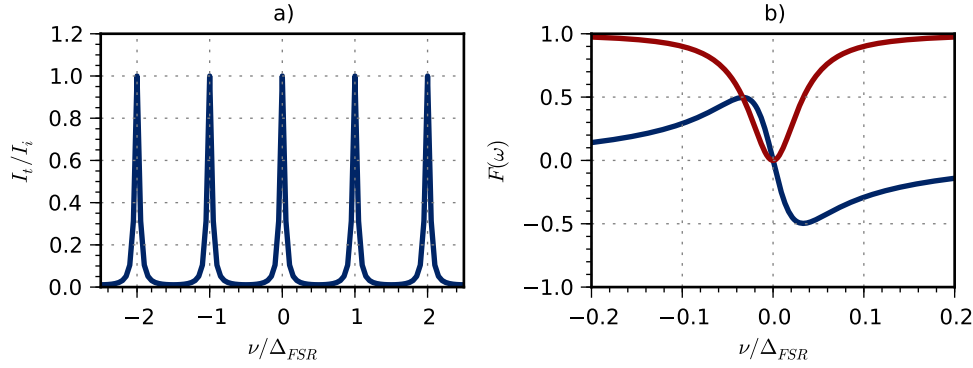


Figure 7.2: The resonator response for $R = 0.9$ ($\mathcal{F} = 15$). a) The relative intensity transmitted through the cavity ($1 - |F(\omega)|^2$) b) The ■ imaginary and ■ real part of $F(\omega)$ close to a resonance.

7.2 The Pound-Drever-Hall Technique

The Pound-Drever-Hall technique relies on sideband modulation to extract the phase of the reflected carrier. Sidebands can be imposed on the light by modulating the phase of the light periodically. This can be realized for example with an Electro-Optic Modulator (EOM) where the refractive index depends on the applied electric field.⁴ If the phase is modulated with an angular frequency Ω , the resulting electric field will be given by

$$E = E_0 e^{i(\omega t + \beta \sin(\Omega t))}, \quad (7.5)$$

where E_0 is the electric field amplitude and ω the angular frequency of the light. β is the so-called modulation index indicating the peak phase shift of the field.⁵ This expression can be expanded using Bessel functions, and for a low modulation ($\beta \ll 1$), only the first two terms will be significant, giving:⁶

$$E = E_0 \left(J_0(\beta) e^{i\omega t} + J_1(\beta) e^{i(\omega + \Omega)t} - J_1(\beta) e^{i(\omega - \Omega)t} \right). \quad (7.6)$$

⁴ An alternative is to modulate the frequency of the laser. In this case the sidebands will also be present in the light used in the experiments, but this is typically not a problem when broad transitions are addressed. When addressing narrow transitions these sidebands are generally unwanted and in this case an EOM in a separate branch is preferable.

⁵ In the case where the laser is used for modulation the result is actually not phase modulation but rather frequency modulation [$E_0 e^{i(\omega + m \sin(\Omega t))t}$]. The two types are however related, and the resulting fields are identical with the substitution $\beta = m/\Omega$. It is worth noting that modulation of the diode current also introduces amplitude modulation which will give a slight asymmetry in the signal [57].

⁶ Truncating the Bessel series at the first two terms is equivalent to the small angle approximation $e^{i(\omega t + \beta \sin(\Omega t))} \approx e^{i\omega t} (1 + i\beta \sin(\Omega t)) = e^{i\omega t} (1 + \beta(e^{i\Omega t} - e^{-i\Omega t})/2)$.

This shows the presence of a carrier with frequency ω and two first order sidebands with frequencies $\omega \pm \Omega$.⁷ When this field is incident on the resonator, the reflected field will be given by:

$$E_r = E_0 \left(F(\omega) J_0(\beta) e^{i\omega t} + F(\omega + \Omega) J_1(\beta) e^{i(\omega + \Omega)t} - F(\omega - \Omega) J_1(\beta) e^{i(\omega - \Omega)t} \right) \quad (7.7)$$

This field is detected on a photo diode which generates an electric current proportional to the optical power, $|E|^2$. The signal on the detector is then given by:⁸

$$\begin{aligned} |E_r|^2 = & |E_0|^2 \left(|F(\omega) J_0(\beta)|^2 + |F(\omega + \Omega) J_1(\beta)|^2 + |F(\omega - \Omega) J_1(\beta)|^2 \right) \\ & + 2J_0(\beta) J_1(\beta) \Re \left[F(\omega) F^*(\omega + \Omega) - F^*(\omega) F(\omega - \Omega) \right] \cos(\Omega t) \\ & + 2J_0(\beta) J_1(\beta) \Im \left[F(\omega) F^*(\omega + \Omega) - F^*(\omega) F(\omega - \Omega) \right] \sin(\Omega t) \quad (7.8) \\ & + 2J_1^2(\beta) \Re \left[F(\omega - \Omega) F^*(\omega + \Omega) \right] \cos(2\Omega t) \\ & + 2J_1^2(\beta) \Im \left[F(\omega - \Omega) F^*(\omega + \Omega) \right] \sin(2\Omega t) \end{aligned}$$

The resulting signal is a wave with nominal frequency ω but with a beating pattern oscillating at two distinct frequencies Ω and 2Ω . Without the cavity, the phase of the different terms match up to a pure phase modulation which is undetected by the photo diode. This is seen by setting all the $F(\omega)$ -terms to unity, in which case the sine and cosine terms disappear i.e., the beating pattern vanishes.⁹ With the cavity, the phase is frequency dependent (as we saw in Figure 7.2) and this gives rise to a beating pattern when the light is slightly detuned from resonance. The important term is the $\cos(\Omega t)$ term, as this samples the phase of the carrier (this will be clear in the next paragraph). This term can be isolated with a mixer and a low pass filter:

A mixer is a device with two inputs and one output, where the output is the product of the inputs - in this case the reference oscillator $[\sin(\Omega t)]$ and the PDH signal from Equation 7.8. The PDH signal contains several harmonic frequencies, for now we will write it as $\sum_i A_i(t) \sin(\Omega_i t + \phi_i)$. The output of

⁷ When β is not much smaller than unity, higher order sidebands must be included for a correct description of the field.

⁸ This derivation is straight forward algebra if one remembers that $z - z^* = i\Im(z)$ and vice versa.

⁹ The 2Ω terms will actually still be left, but this is a result from truncating the Bessels series; including higher order terms would make those terms cancel out too.

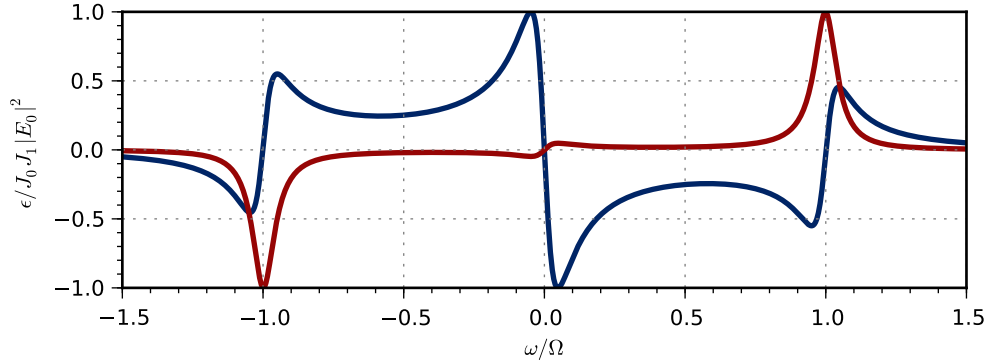


Figure 7.3: The error signal for different phases: $\blacksquare \phi = 0$; $\blacksquare \phi = \pi/2$ with $\mathcal{F} = 30$. A higher finesse results in narrower features around the carrier and sidebands.

the mixer is then:

$$\begin{aligned} \epsilon &= \sin(\Omega t) \sum_i A_i(t) \sin(\Omega'_i t + \phi_i) \\ &= \frac{1}{2} \sum_i A_i(t) (\cos((\Omega'_i - \Omega)t + \phi_i) - \cos((\Omega'_i + \Omega)t + \phi_i)) \end{aligned} \quad (7.9)$$

For an input with a single frequency of Ω' , the output will be a sum of two frequencies $\Omega + \Omega'$ and $\Omega - \Omega'$. If $\Omega = \Omega'$, the term $\cos((\Omega - \Omega')t + \phi)$ is a stationary signal which can be isolated with a low pass filter. In Equation 7.9 the amplitude is explicitly time dependent $[A_i(t)]$, but as long as the amplitude varies slower than the cutoff of the low pass filter these variations will pass through; it is possible to extract the amplitudes of the signals oscillating at frequency Ω . In Equation 7.9, we looked at the product of two sine waves, but in Equation 7.8 we have both a sine and a cosine wave oscillating at frequency Ω . This can be incorporated in the phase ϕ and combining these equations we get:

$$\epsilon = |E_0|^2 J_0(\beta) J_1(\beta) \left(\Re[\mathcal{I}(\omega)] \sin(\phi) + \Im[\mathcal{I}(\omega)] \cos(\phi) \right), \quad (7.10)$$

where $\mathcal{I}(\omega) = F(\omega)F^*(\omega + \Omega) - F^*(\omega)F(\omega - \Omega)$. This signal is illustrated in Figure 7.3. Depending on ϕ , the error signal, ϵ , is a linear combination of the two illustrated signals. The signal for $\phi = 0$ has a large slope and is close to linear just around the resonance; this is exactly what we want to determine the frequency of the light. Experimentally, ϕ is determined by the phase difference between the optical and electrical paths. $\phi = 0$ is then realized by including an adjustable phase delay on the reference oscillator.

When the carrier is near resonance and the modulation frequency is high enough that the sidebands are not, the sidebands will be totally reflected

$[F(\omega \pm \Omega) = 1]$. In this case Equation 7.10 reduces to

$$\epsilon = 2|E_0|^2 J_0(\beta) J_1(\beta) \Im[F(\omega)] \quad (7.11)$$

for $\phi = 0$. The error signal basically samples the phase of the reflected carrier, $\Im[F(\omega)]$ (pictured in Figure 7.2b).

Close to a resonance, δ will be close to a multiple of 2π , and we can write $\delta = 2\pi N + \Delta\omega/\nu_{\text{FSR}}$, where N is an integer and $\Delta\omega$ is the detuning from resonance. For small $\Delta\omega$ we can expand $e^{i\delta}$ from Equation 7.4 in a power series, and if we truncate this after the first two terms we get:

$$F(\Delta\omega) \approx r \frac{i\Delta\omega/\nu_{\text{FSR}}}{1-r^2} = \frac{\mathcal{F} i\Delta\omega}{\pi \nu_{\text{FSR}}} = \frac{i \Delta\omega}{\pi \nu_{1/2}}. \quad (7.12)$$

Combining this with Equation 7.11 gives:

$$\epsilon = 2|E_0|^2 J_0(\beta) J_1(\beta) \frac{\Delta\omega}{\pi \nu_{1/2}}. \quad (7.13)$$

The amplitude of this error signal depends on the modulation depth, the incident optical power, the gain in the photo detector etc. By realizing that the peak-to-peak amplitude of Equation 7.10 is $\epsilon_{pp} = 2|E_0|^2 J_0(\beta) J_1(\beta)$ we get a relation between the frequency deviation ($\Delta\nu = \Delta\omega/2\pi$) and the error signal given by:

$$\Delta\nu = \frac{\nu_{1/2}}{2\epsilon_{pp}} \epsilon \quad (7.14)$$

This result is valid for small frequency detunings just around resonance and can be used to translate fluctuations in the error signal to fluctuations in the frequency of the laser, and thereby to evaluate the lock performance and estimate the linewidth of the laser.

With the PDH technique, we have realized an antisymmetric signal with strong dependence on the detuning close to resonance; we have a good frequency reference for feeding back unwanted deviations. The next chapter is focused on describing the theory of using such a signal to improve the performance of a system using a feedback loop. Before diving into this theory, a few experimental considerations for realizing the PDH technique in practice are discussed:

7.3 Experimental Considerations

Power Fluctuations

The PDH technique benefits from the fact that the error signal on resonance is independent of the optical power. This is important to avoid offset changes which could otherwise change the frequency of the laser.

Fluctuations in the optical power will, however, change the slope of the error signal and hence the gain in the feedback loop. As will be clear in the next chapter, this can affect the performance of the lock, and power fluctuations should therefore be kept to a minimum.

Polarization

The PDH technique in itself is insensitive to changes in the polarization, but if polarization dependent optical components are used, these can result in a modified error signal. It is particularly worth noting that if the polarization of the light is not perfectly matched to the axes of the EOM crystal, residual amplitude modulation can appear after polarization dependent elements. This modulation will oscillate with frequency Ω and therefore give rise to an offset in the lock signal. For a constant offset (constant amplitude modulation) this can simply be compensated electronically. With a fluctuating offset this will however translate into fluctuations in the frequency of the light. It is therefore advantageous to obtain a clean polarization before the EOM; for example with a Glan-Thompson Polarizer.

Modulation Frequency

The modulation frequency, Ω , can in principle be chosen arbitrarily but it will limit the operating range and bandwidth of the final system. Instantaneous frequency fluctuations larger than Ω will give rise to an error signal with the wrong sign and cannot be corrected - the laser jumps out of lock. Additionally, the low pass filter used to isolate the amplitudes in front for the harmonic Ω terms will limit the bandwidth of the system. To correct high frequency fluctuations it is required to use a high modulation frequency.

Electronic Bandwidth

In order to achieve a narrow and/or stable lock, the bandwidth of the entire system should be as large as possible. There are typically limits in the physical system itself, but it is important to keep the bandwidth of the electronics significantly above these limits. As discussed in [Chapter 8](#), it is important to reduce possible phase delays in the entire system to achieve good performance. A typical first order system has significant phase contribution below the cutoff as seen in [Figure 8.1](#). This clearly indicates that the bandwidth of the electronics should always be kept at least one decade above the intended bandwidth of the entire system to avoid additional phase delay and degraded performance. In addition, low phase delay also requires short cables and optical paths e.g., a single meter adds roughly 4° phase delay at 1 MHz due to the propagation of the electric signal.

CHAPTER 8

Control Theory

This chapter serves as a brief introduction to control theory and its application for laser stabilization. Large parts of classical control theory rely on concepts used in electronics engineering, and a good understanding necessarily requires basic knowledge of these concepts. This chapter provides a brief introduction to control theory in the frequency domain using these concepts, but for the reader interested in a deeper understanding, consulting a more general textbook, for example [58], is recommended.

8.1 Transfer Functions

A central concept in control theory is the so-called transfer function. A transfer function is a mathematical model of a system relating its output to its input, simply put $G = \frac{V_{out}}{V_{in}}$.¹ For an ideal wire the transfer function would simply be $G = 1$; the output equals the input. If the circuit contains anything but ideal resistors, both the amplitude and phase of the output will depend on the frequency of the input. Analysis of such circuits is greatly simplified in the frequency domain using Laplace transformation. Laplace transformation will not be discussed here;² it suffices to know that the impedance of regular components (electronic or mechanical) can be transformed to the frequency/Laplace domain. In the electronic domain, this makes it possible to investigate complex circuits with capacitors and inductors just as one would analyze a network of resistors - this makes the Laplace transform a very important tool in such analysis. It is not necessary to be able to calculate transfer functions for electronic circuits to understand the theory of feedback, but

¹ In this example it relates input voltage to output voltage, but it could just as well describe other physical parameters e.g., frequency. These quantities are, though, usually converted to an electric current with appropriate transducers for use in feedback systems.

² Consult for example [59] for an introduction to Laplace transformation for electronic circuits.

for the reader interested in getting a deeper understanding of transfer functions, [59, chap. 10] and [58, chap. 2] are recommended. With a well-known transfer function, the response of a circuit can be evaluated for different frequencies as $G(i\omega)$, where amplitude and phase can be extracted as:

$$\begin{aligned} A &= |G(i\omega)| \\ \theta &= \arg(G(i\omega)) \end{aligned} \quad (8.1)$$

To illustrate the purpose of transfer functions, we start with a simple example with a RC low pass circuit (illustrated in Figure 8.3a). In the frequency domain, the transfer function of such a circuit can be calculated to $G(s) = 1/(1 + RCs)$. Figure 8.1 shows the amplitude and phase of this function for different frequencies according to Equation 8.1. This type of plot is normally called a Bode plot. Transfer functions are typically discussed with regards to their zeros and poles, that is the points where either the numerator or denominator go to zero. In the case of the low pass filter, we have a pole at $s = 1/RC$ (in the figure $\omega_c = 1/RC = 2\pi \cdot 10 \text{ kHz}$) which gives rise to the damping at high frequencies. Inspecting the figure tells us that applying an input at frequency $\nu = 10 \text{ kHz}$ results in an output signal reduced by 3 dB and with a 45° phase delay.³ For frequencies significantly above the cutoff frequency, the system show a 90° phase lag and an amplitude decreasing as $1/\nu$. A transfer function with a zero would exhibit similar behavior, but in this case the amplitude increases above the cutoff frequency and we observe a positive phase (phase advance); essentially a mirror image of Figure 8.1.

³ 3 dB corresponds to half the power or a factor of $\sqrt{2}$ in amplitude.

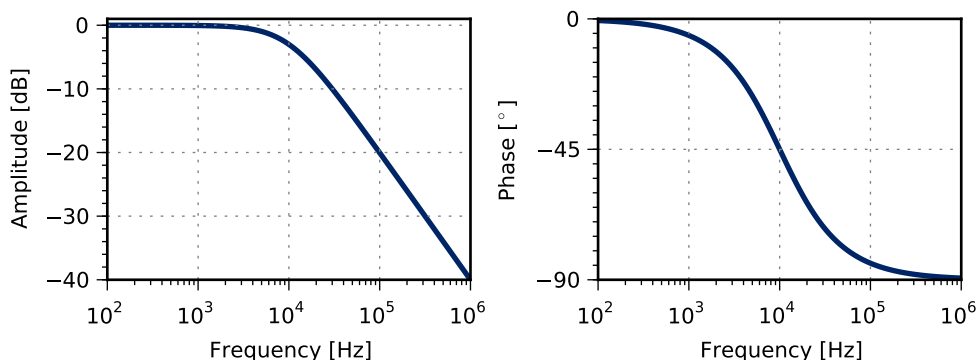


Figure 8.1: Amplitude and phase response of an ideal RC low pass filter with a cutoff frequency of $\nu_c = 1/2\pi RC = 10 \text{ kHz}$.

8.2 The Feedback Loop

The low pass circuit discussed in the previous section is typically designed to suppress high frequencies, but it could just as well be an unwanted feature of the system we want to control (e.g. the current regulation of a diode). For now we will continue to use the low pass circuit to demonstrate the idea of the feedback loop, keeping in mind that it could just as well be a laser system.

We can analyze how fast the system can respond to a change in input by applying a step signal at the input and monitor the signal at the output as a function of time. This response can be calculated through inverse Laplace transform, which for the low pass circuit gives: $c(t) = 1 - e^{-t/RC}$. This output is illustrated in Figure 8.2 together with the input [the lines noted open loop response / input]. We observe that the response is limited by the low pass characteristic of the circuit and settling to the final value takes approximately $t = 1/\nu_c = 2\pi RC$.

It is possible to improve the speed of the circuit by placing it in a closed loop as illustrated in the block diagram in Figure 8.3b. In a closed loop, the output, $C(s)$, is subtracted from the input, $R(s)$, in the summing junction (the round symbol). The error, $e(s)$, is then sent through a controller with transfer function $G_c(s)$ and finally through the system we want to regulate [with transfer function $G_l(s)$] - we will call this system the laser, though for now it is modeled by the low pass filter. The controller essentially receives a signal corresponding to the deviation of the output from the input, and with this signal, the controller generates an input to the laser to drive the output towards the input. To achieve good performance, the controller must be optimized for the given system.

By analyzing the block diagram, we see that $e(s) = R(s) - C(s)$ and

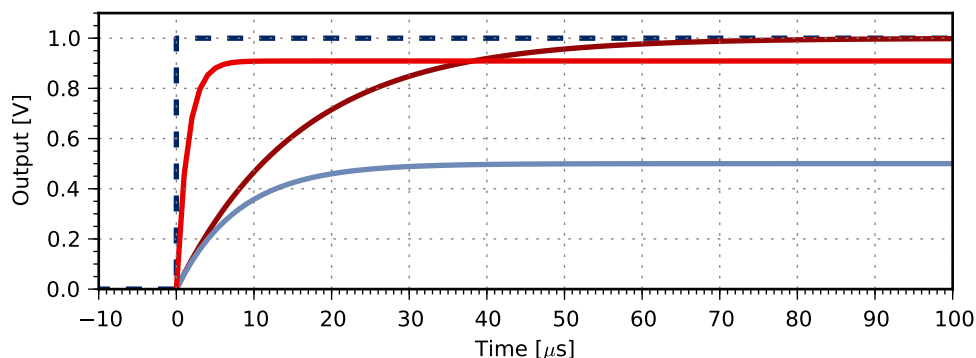


Figure 8.2: Step response of the low pass circuit from Figure 8.1. - Input; - Open loop response; - Closed loop response [$G_c(s) = 1$]; - Closed loop response [$G_c(s) = 10$].

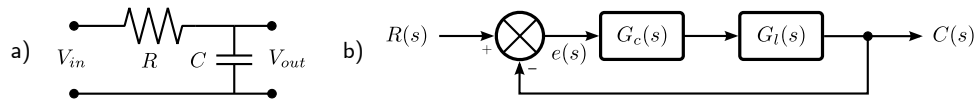


Figure 8.3: a) The RC low pass circuit. b) Block diagram of the closed loop system with $G_c(s)$ representing the controller and $G_l(s)$ the laser (in this case just the low pass filter).

$C(s) = G_l(s)G_c(s)e(s)$. With ordinary arithmetic, we can calculate the transfer function of the entire system from $R(s)$ to $C(s)$:

$$T(s) = \frac{C(s)}{R(s)} = \frac{G_c(s)G_l(s)}{1 + G_c(s)G_l(s)} \quad (8.2)$$

We can now analyze this system and compare the response to that of the system without feedback (open loop) as seen in Figure 8.2. In the simple case with a unity gain controller, $G_c(s) = 1$, we observe a faster response, but we also introduce a steady state error of 50% (the final amplitude of the output is only half that of the input).⁴ Increasing the gain, $G_c(s) = 10$, makes the system even faster and reduces this error. In this ideal case, we can actually continue to increase the gain to improve performance, with the output converging towards an actual step function. In reality, there are always additional poles in the system, and these poles will limit the amount of gain that can be applied. This will be clear when we model the actual laser system, but before that, we will just discuss how this model looks for an actual laser system.

8.2.1 Transfer Function of a Laser System

For the low pass filter we can imagine the input, $R(s)$, as an electrical signal (voltage). This signal is modified in the controller and applied to the input of the low pass circuit and we then observe the potential at the output; in this case all signals can be considered as potential differences. For a laser system

⁴ We continue to label the transfer function of the controller $G_c(s)$ for consistency, though in this case it is independent of s .

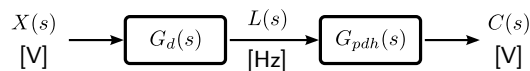


Figure 8.4: The internal components of $G_l(s)$. The electric signal $X(s)$ is converted in the diode to an optical frequency $L(s)$ which is determined using the PDH scheme and converted back to an electric signal $C(s)$.

the signal is converted between different physical quantities as illustrated in Figure 8.4. Let us imagine a diode laser where we control the output frequency, $L(s)$, by regulating the current in the diode, $X(s)$. We basically convert the electric signal to an optical frequency in $G_d(s)$, the transfer function of the diode. Whereas $X(s)$ was expressed in units of electric potential (V), $L(s)$ is expressed in units of frequency (Hz). The conversion, $G_d(s)$, can itself have a non-trivial frequency dependence due the underlying semiconductor physics or limits in the electronics. The optical signal is then reflected on a resonator and demodulated using the PDH technique. This process [with transfer function $G_{PDH}(s)$], converts the optical signal back to an electrical signal corresponding to $C(s)$ in Figure 8.3b. Though the internal structure is more complex than for the low pass filter, the system basically still have a an electrical input and output, and the system can be modeled in the same way.⁵ In principle, it is not even necessary to know the physical processes inside $G_l(s)$. For regulation purposes it suffices to know the transfer function itself, and as we will see in Section 10.3.1, this can be determined experimentally.

8.2.2 Feedback in Systems with Two Poles

To illustrate the problems that arise with two or more poles, we will model the actual laser system. The transfer function is determined in Section 10.3.1, but for now we will just treat it as a mathematical model with two poles at $\omega_1 = 2\pi \cdot 140$ KHz and $\omega_2 = 2\pi \cdot 700$ kHz:

$$G_l(s) = \frac{1}{(s/\omega_1 + 1)(s/\omega_2 + 1)} \quad (8.3)$$

This transfer function is illustrated in Figure 8.5 [the curve for $G_c(s) = 1$]. If additional poles are present in the system, high gain will result in feedback oscillations. This is observed as an output which does not rise monotonically towards the final value but exhibit damped oscillations; typically termed overshoot. The amount of overshoot is related to the phase margin of the open loop system. The phase margin is defined as the margin between the phase delay at the unity gain frequency and 180° as illustrated in the figure.

For unity gain, $G_c(s) = 1$, the phase margin is 180° and there is no overshoot as seen in Figure 8.6. The low gain does, however, result in a significant

⁵ In laser locking, the input is typically just set to zero (the zero crossing of the PDH signal). This can be a bit confusing, as in a linear system this would result in an optical frequency of 0 Hz. In practice though, the system is not linear, and we just modulate the current slightly around an offset. Because the PDH signal is also zero at this offset, the model is fine as long as we work within a small detuning with respect to the resonance.

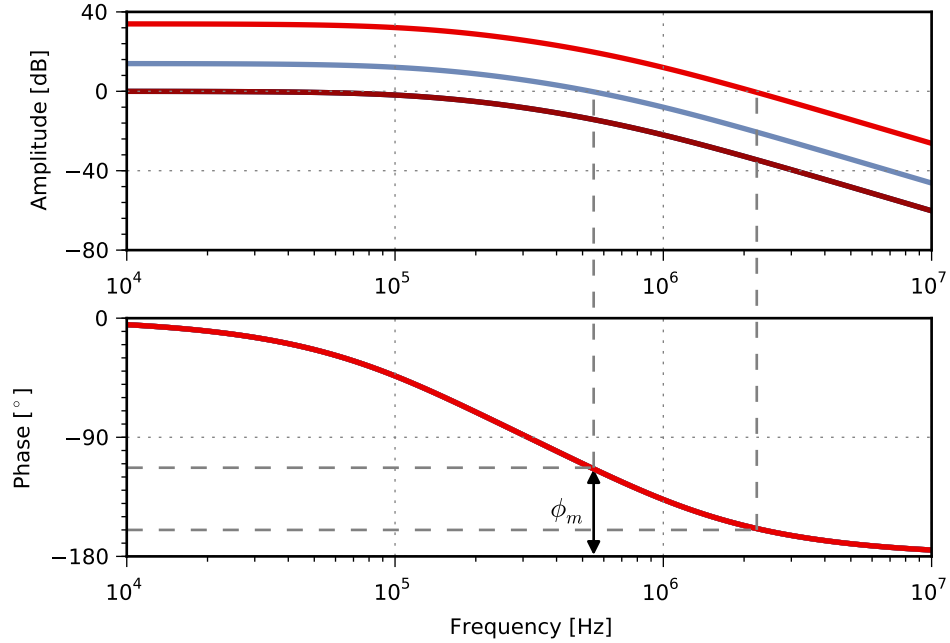


Figure 8.5: Amplitude and phase of the open loop transfer function $[G_I(s)G_c(s)]$ with $\blacksquare G_c(s) = 1$; $\blacksquare G_c(s) = 5$; $\blacksquare G_c(s) = 50$. The dashed lines indicate the unity gain frequencies and phase margins for $G_c(s) = 5$ and $G_c(s) = 50$. The phases are identical in the three cases and therefore overlap.

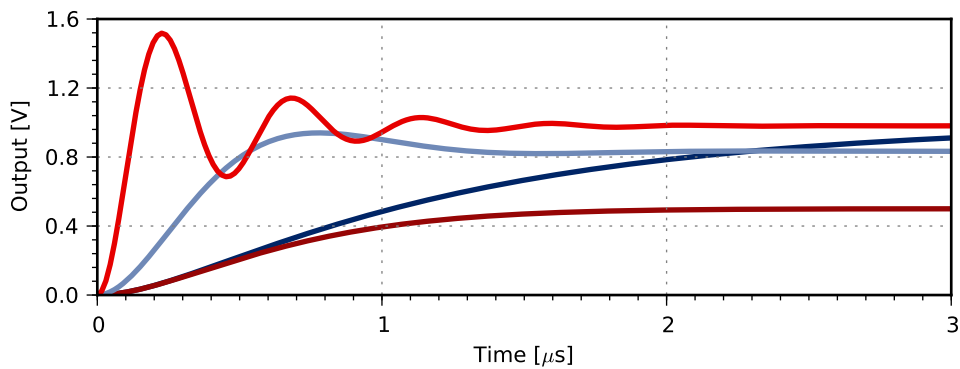


Figure 8.6: System response with poles at $\nu_c = 140$ kHz and $\nu_{\text{FET}} = 700$ kHz. \blacksquare Open loop response; \blacksquare Closed loop response $[G_c(s) = 1]$; \blacksquare Closed loop response $[G_c(s) = 5]$; \blacksquare Closed loop response $[G_c(s) = 50]$.

steady state error of 50%. Increasing the gain to $G_c(s) = 5$ reduces this error, but at the same time reduces the phase margin to 67° degree and increases the overshoot slightly. Increasing the gain even further to $G_c(s) = 50$ results in a significant overshoot. With a decreasing phase margin the overshoot increases - the system appear more oscillatory.⁶ Choosing the gain of the controller is a compromise between overshoot and steady state error. A way to achieve slightly better performance is to introduce more advanced feedback controllers using so-called lead and lag regulators - the topic of the next section.

8.3 Lead and Lag Regulators

Some readers might be familiar with controllers of the type Proportional-Integral-Derivative (PID). In addition to the proportional regulator discussed in the previous section, this type of controller also contains an integral and derivative regulator. The purpose of these regulators is to reduce the steady state error and the overshoot (respectively). The integral and derivative regulators are just a special case of the more general regulators: the lag and lead regulators, which we will discuss in this section.

The purpose of the lead regulator is to reduce overshoot, and as we saw earlier, the overshoot is closely related to the phase margin: To reduce overshoot, we must reduce the phase delay around the unity gain bandwidth. As briefly mentioned in Section 8.1, a zero in the transfer function will contribute with a phase advance above the cutoff frequency.⁷ This can be used to increase the phase margin in a regulation system. If we introduce a zero at $s = -\omega_{lead}$, we get a positive phase contribution above ω_{lead} as illustrated by the dashed line in Figure 8.7a. This corresponds to the ideal derivative regulator. The more general case, the lead regulator, has an additional pole at higher frequency ω_{lead}/β ($\beta < 1$) with the transfer function:

$$G_{lead}(s) = \frac{1}{\beta} \frac{s + \omega_{lead}}{s + \omega_{lead}/\beta} \quad (8.4)$$

This is illustrated by the solid curve in Figure 8.7a for $\beta = 1/25$. The net effect of the lead regulator is to introduce a positive phase delay to the system. This can be used to compensate a part of the phase delay to reduce overshoot. Figure 8.8 show the Bode plot of the open loop transfer function

⁶ The oscillatory behavior can to some degree be understood from an intuitive model. When the controller senses a disturbance it will try to correct it. For frequency components where the phase delay in the system is close to 180° , the correction signal will be delayed almost half a period. This basically leads to an amplification instead of a suppression. The larger the phase margin, the slower will these components decay.

⁷ Actually the phase advance sets in approximately one decade below the cutoff.

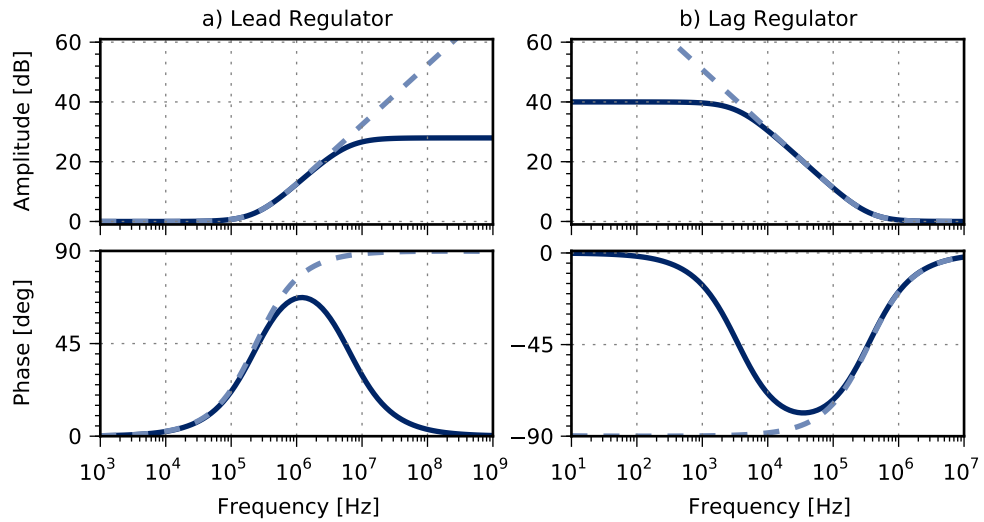


Figure 8.7: Transfer function of the lead regulator ($\omega_{lead} = 2\pi \cdot 250 \text{ kHz}$, $\beta = 1/25$) and the lag regulator ($\omega_c = 2\pi \cdot 10 \text{ kHz}$, $\beta = 100$). The phase and gain contribution from the lead regulator is lower than for the lag regulator due to different values of α and β . For the same value of β the magnitude of the contributions would be the same. The dashed lines indicate the transfer functions of the ideal D/I regulators ($\beta = 0$, $\alpha = \infty$)

of the system with and without a lead regulator with the same parameters as in Figure 8.7a. The lead regulator increases the unity gain bandwidth from 0.9 MHz to 3.5 MHz and at the same time the phase margin from 50° to 70° . This is clearly seen in the step response of the system in Figure 8.9 as a faster settling with less overshoot.

Reversing the position of the pole and zero realizes a so-called lag regulator with an almost identical transfer function:

$$G_{lag}(s) = \frac{s + \omega_{lag}}{s + \omega_{lag}/\alpha} \quad (8.5)$$

In this case, $\alpha > 1$ and the zero is at higher frequency than the pole. The lag regulator is used where higher low frequency gain is required. From Figure 8.7b it is clear that this also introduces an additional phase delay. If the cutoff is placed one decade below the unity gain bandwidth, this additional phase delay will contribute very little to the phase margin as seen in Figure 8.8. In this case, the fast response remains almost unchanged, but the increased low frequency gain has reduced the steady state error as seen in Figure 8.9. The ideal integral regulator is a specific case of the lag regulator with $\alpha = \infty$ (the pole at $s = 0$), where the derivative regulator is a specific case of the lead regulator with $\beta = 0$ (the pole at $s = \infty$).

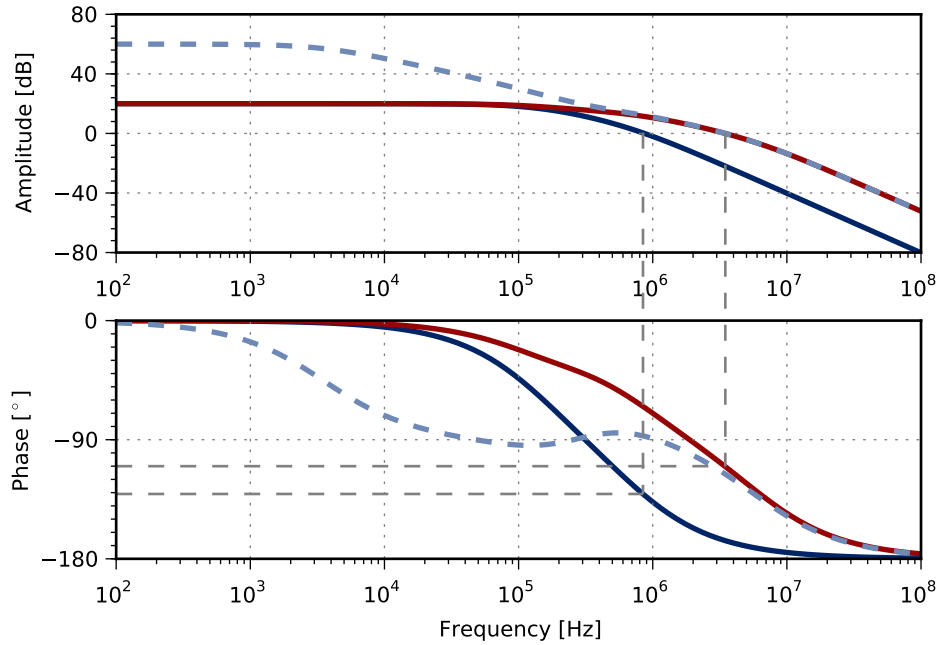


Figure 8.8: Open loop transfer function with different controllers — Proportional [$G_c(s) = 10$]; — Proportional + Lead [$G_c(s) = 10 \cdot G_{lead}(s)$] with $\omega_{lead} = 2\pi \cdot 250$ kHz and $\beta = 1/25$; — Proportional + Lead + Lag [$G_c(s) = 10 \cdot G_{lead}(s) \cdot G_{lag}(s)$] with $\omega_{lag} = 2\pi \cdot 10$ kHz and $\alpha = 100$. The dashed lines indicate the unity gain frequencies and phase margins.

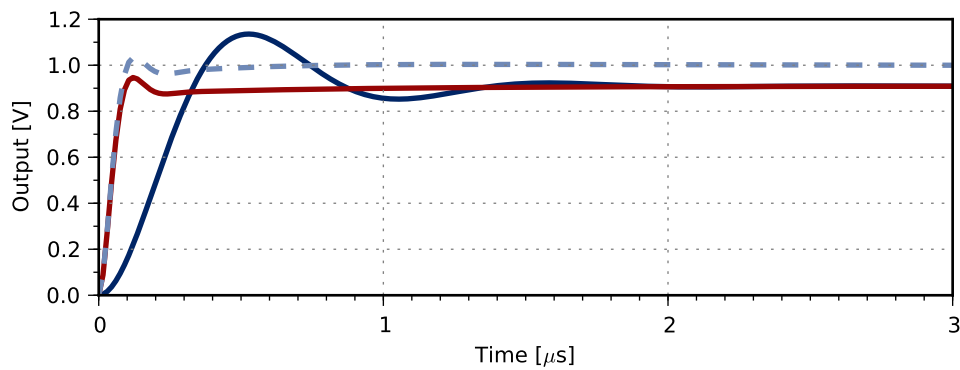


Figure 8.9: System response for different controllers: — Proportional Controller; — Proportional + Lead; — Proportional + Lead + Lag. Parameters as in Figure 8.8

The lead and lag regulators are used to alter the slow and fast response independently, and both these types of regulators can therefore be important to optimize a feedback loop. For a more detailed explanation of these regulator types [58, chap. 11] is recommended.

The lead and lag are probably the most common types of regulators, but other types of regulators can be relevant in specific systems. One example is the so-called notch filter, which can be used to cancel a mechanical resonance to avoid ringing.⁸

8.4 Laser Locking

Until now, we have analyzed the response of the system to a change in input - similar to many textbooks on classical control theory. For laser stabilization, the picture is a bit different: here the frequency is fixed and the feedback system should suppress unwanted disturbances which force the laser away from this frequency. As it turns out, these cases are quite similar:

The actual laser system can be modeled by introducing a disturbance, $D(s)$, to the system as illustrated in Figure 8.10. The output of this system is:

$$C(s) = \frac{R(s)G_c(s)G_l(s) + D(s)}{1 + G_c(s)G_l(s)}, \quad (8.6)$$

When the disturbance is zero [$D(s) = 0$], the transfer function of the system with respect to the input, $T(s) = C(s)/R(s)$, is identical to Equation 8.2. In laser stabilization, $R(s)$ is typically set to zero (i.e. the zero crossing of the PDH error signal) and we are interested in how a disturbance, $D(s)$, affects the system. In this case, it is the transfer function with respect to the disturbance which is relevant, given by:

$$Q(s) = \frac{C(s)}{D(s)} = \frac{1}{1 + G_c(s)G_l(s)}. \quad (8.7)$$

With $G(s) = G_c(s)G_l(s)$ and a slight rearrangement this becomes:

$$Q(s) = \frac{1}{1 + G(s)} = \frac{1 + G(s) - G(s)}{1 + G(s)} = 1 - \frac{G(s)}{1 + G(s)} = 1 - T(s), \quad (8.8)$$

The response of the system to a disturbance is very similar to the response to a change in input. The main difference is that the system finally settles to the new value when the input is changed, whereas a disturbance is eventually

⁸ This is for example the case when a PZT is used for feedback as described in [60]. This thesis is also recommend for the reader interested in a description of the practical aspects of laser stabilization.

canceled out. This is illustrated in Figure 8.11 which shows the response of the two different transfer functions.

This result shows that the standard techniques from control theory can be directly applied in the design of a system to cancel disturbances, such as in laser stabilization.

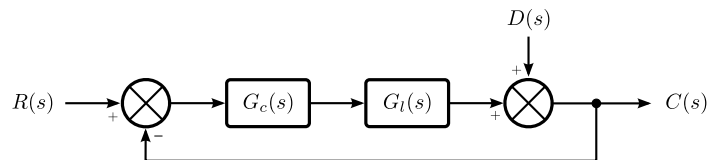


Figure 8.10: Model of the control system for locking a laser. $D(s)$ simulates a disturbance which forces the laser away from the desired frequency. It is this disturbance which the feedback system is supposed to suppress. For a correct intuitive model, the disturbance should be added to $L(s)$ in Figure 8.4, as $C(s)$ is actually the PDH signal. For simplicity, the disturbance is added here as this does not affect the validity of the result.

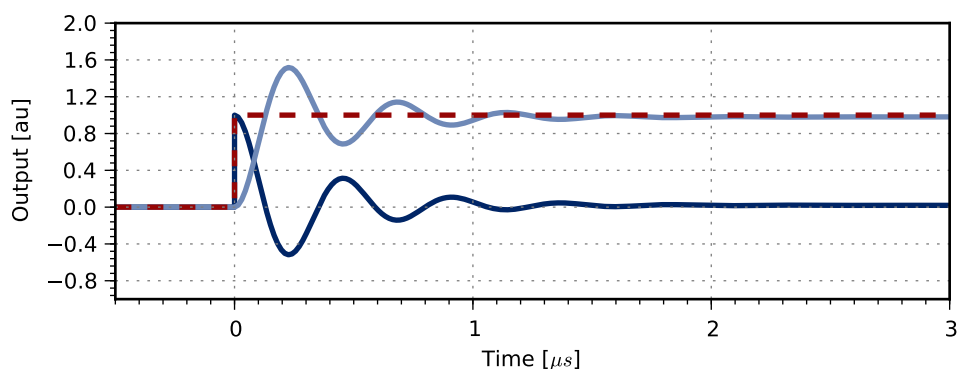


Figure 8.11: The systems response to: \blacksquare a disturbance $[Q(s)]$; \blacksquare a change in input $[T(s)]$. --- the signal applied as either input/disturbance respectively.

Optical Resonator Design

When the laser is locked, its frequency will follow that of the resonator; to realize a stable laser system it is crucial that the frequency of the resonator do not fluctuate. As seen from the resonator equation in [Chapter 7](#), the resonance frequency is affected by changes in the optical distance between the mirrors. These changes originate mainly from temperature fluctuations and acoustic/seismic vibrations transferred to the cavity through the supporting structure. Minimizing these contributions is important to realize long term frequency stability and a narrow linewidth.

9.1 Temperature Stabilization

Due to the thermal expansion of solids, fluctuations in temperature will give rise to changes in the length of the resonator and thereby the resonance frequency. This can be addressed by active temperature stabilization and a proper choice of materials.

9.1.1 Active temperature stabilisation

Over the course of a single day, the temperature in the laboratory typically fluctuates a few degrees, due to thermal dissipation of the equipment and variations in the air conditioning flow. To minimize this contribution, the cavity is placed inside a temperature stabilized housing. The active temperature stabilization consists of two layers as seen in [Figure 9.1](#). The outer layer is realized with a vacuum tube which is temperature stabilized with a heating wire. The temperature is measured by 10 Negative Temperature Coefficient (NTC) thermistors which are evenly distributed along the tube. These NTCs are used in a closed servo loop together with the heating wire. By elevating the temperature of the tube above that of the surroundings, the

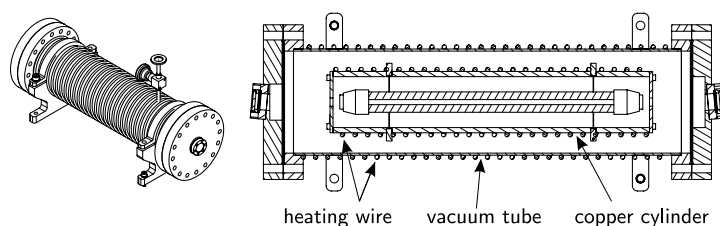


Figure 9.1: The temperature stabilized housing for the cavity consisting of an outer steel tube providing vacuum and an inner copper tube acting as heat shield.

temperature can effectively be controlled by raising or lowering the current in the heating wire. With this setup, it is possible to reduce temperature fluctuations by at least two orders of magnitude.

The second layer is based on a copper cylinder which is mounted inside the vacuum tube. The copper cylinder acts as both a thermal buffer and a heat shield through its large heat capacity and reflecting surfaces. The copper cylinder is actively temperature stabilized in the same way, with a heating wire and NTCs. The copper cylinder plays two important roles: First it acts as a second layer of temperature stabilization, and secondly, it assures a uniform temperature of the cavity spacer. Without this layer, changes in the thermal distribution of the vacuum tube would directly affect the thermal distribution in the spacer.

To avoid metal-to-metal contact (which could give rise to significant heat flow variations with temperature changes) a small piece of Kapton is placed between the vacuum tube and the supports. With this setup, variations below 1 mK are observed inside the copper tube.

9.1.2 Design Considerations

Besides assuring a stable temperature, a proper choice of materials is important to reduce the temperature sensitivity of the cavity. For that reason, the cavity-spacer (see Figure 9.2) and the mirrors were constructed from an ultra low expansion material¹ which has a thermal expansion coefficient of $10^{-8} / \text{K}$. In the chosen cavity configuration with a length of 250 mm, a temperature change of 1 K would then result in a length change of 2.5 nm or a 4 MHz frequency shift. With temperature stability better than 1 mK, these fluctuations should be reduced to a few kHz over the course of a day.

¹ Zerodur, Schott AG

Cavity suspension

The cavity is mounted inside the copper cylinder by 4 wires as pictured in Figure 9.4. To obtain minimum sensitivity to vibrations, the cavity is mounted in the symmetry planes (described in Section 9.2), but this requires that the loads on the supports are equal. To ensure this, the cavity is mounted on a soft support with a deflection larger than the machining tolerances. The cavity is supported by 4 wires acting as beams with a spring constant of 1 N/mm, which results in a 0.6 mm deflection under gravity. The wire is enclosed by a Viton cylinder (see Figure 9.4b) which provides an interface between the cavity spacer and the wire and serves to damp oscillations.

Besides assuring an evenly distributed load on the cavity, the wire support decouples the thermal expansion of the copper cylinder from the cavity spacer: if the support had been rigid, thermal expansion would give rise to significant forces on the spacer which would undermine the low thermal expansion of the spacer. With a force constant of 1 N/mm this contribution should be less than 0.1 nm/K compared to the natural thermal expansion of the spacer of 2.5 nm/K.

Mirror mounting

Another important consideration is the mounting of the mirrors to the spacer. For the cavities previously constructed in the group, the mirrors have been attached to a small metal mount connected to the spacer, but this gives rise to a significant change in the resonator length when the mount expands. Instead the mirrors was mounted with a novel spring load system (Figure 9.2).

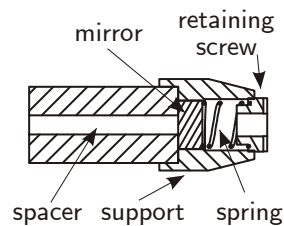


Figure 9.2: The mirror mount

Attached to the spacer is a small support from which a spring presses the mirror against the end of the spacer. With this construction, the mirror surface essentially follows the end of the spacer, and thermal expansion of the mirror mount only affects the resonator length through variations in the induced stress. By choosing a spring with lower force constant than the surroundings, the changes in the resonator length (due to expansion of the mirror mount) are essentially suppressed. For the chosen geometry and with

a spring constant of 5 N/mm, the change in resonator length should be less than 0.1 pm/K.

Apart from the induced axial stress, expansion of the mirror mount also gives rise to radial forces on the spacer which in turn give rise to axial contraction of the spacer through the Poisson effect. Actually, this works opposite to the natural thermal expansion of the spacer, but if the radial expansion is large, this contribution will undermine the good thermal abilities of the spacer.² To reduce this contribution, the mirror mount was constructed from Invar which has a low thermal expansion of 10^{-6} /K. Depending on the type and amount of glue used to fix the support to the spacer, the contraction is estimated to be below 10% of the natural expansion of the spacer.

9.2 Vibration isolation

When the laser is locked to the cavity, any fluctuations in the resonator frequency will be directly transferred to the frequency of the light. On long time scales, this will be dominated by changes in length due to temperature variations, but on short time scales, acoustic/seismic vibrations can couple to the structure and directly change the geometry of the cavity and thereby the resonance frequency. This has two implications: First, if sudden bumps are transferred to the cavity, the laser can jump out of lock, and second, harmonic vibrations can broaden the linewidth of the laser.

Changes in the cavity length can occur either by resonant excitation of the eigenmodes of the structure or by low frequency quasi-static deformation. High frequency vibrations (above 100 Hz) can be suppressed by mounting the setup on a viscous damped platform with a low eigenfrequency,³ and with eigenfrequencies in the kilohertz regime, resonant excitations should be suppressed. When the excitation frequencies are lower than one quarter of the lowest eigenfrequency, the loading can be regarded as quasi-static [61]. In this regime, the forces acting on the structure can be pictured as an acceleration of the entire solid with fluctuations around the basis point resulting from gravity: To reduce the vibration sensitivity of the resonator, this deformation should be minimized.

The cavities previously constructed in the group have been supported from below at the Airy points, and though this does minimize bending of the cavity, it does not suppress axial deformation due to radial compression

² This effect could be exploited to reduce the thermal expansion below the natural, but this would probably require several iterations given the uncertainty in the force distribution in the glue and the thermal expansion coefficients.

³ This is realized by mounting the structure on a platform supported by stud-mounts made from a shock absorbing material (Sorbothane, Sorbothane Inc.). By changing the mass of the platform, the system can be tuned to obtain the desired properties.

through the Poisson effect. The problem is easily illustrated by picturing a square block supported from below or on the top (see Figure 9.3): When the structure is supported from below, the compression in the vertical direction due to gravity will give rise to expansion in the horizontal direction through the Poisson effect (a). If the structure is supported from the top, on the other hand, the Poisson effect will give rise to contraction in horizontal direction (b). Naturally, there must be some point in between where the two effects cancel out (c). In this simple case, this point coincides with the symmetry plane.

The deformation of the cavity with the original support at the Airy points is illustrated in Figure 9.6a. In this configuration, the axial displacement of each mirror amounts to 8 nm/ms^{-2} corresponding to a vibration sensitivity of 13 MHz/ms^{-2} . With typical vibrations in the order of 10^{-3} m/s^2 , this would limit the attainable linewidth to the kHz range, in addition to making the lock very sensitive to disturbances.

To suppress the axial deformation from the Poisson effect, the spacer should be supported in the mid-plane. Inspired by a similar setup [62], the spacer was designed to be supported on four blind holes, as illustrated in Figure 9.4.

Because the length of the cavity is large compared to the diameter, gravity will also give rise to significant bending, as illustrated in Figure 9.6a. This bending changes the angle of the mirrors and thereby the optical length of

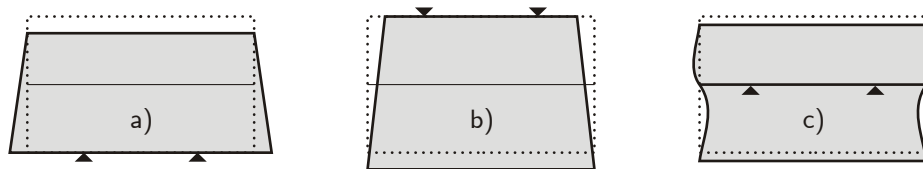


Figure 9.3: Horizontal deformation due to gravity through the Poisson effect. a) supported from below b) supported on the top c) supported in the symmetry plane.

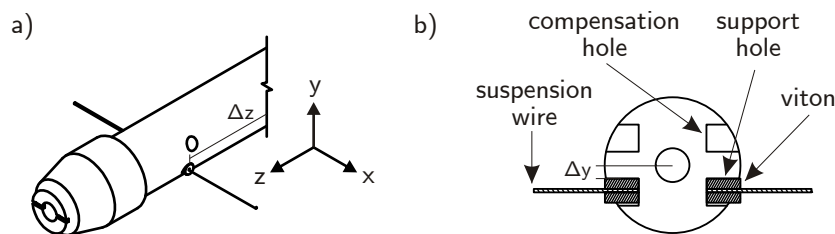


Figure 9.4: Illustration of the cavity support a) isometric view b) cross section of the spacer in the mounting plane. The other end of the suspension wires are attached to the copper cylinder.

the resonator. From [63, p. 768] it is easily shown that for small changes in the mirror angle, α , the change in the optical length is:

$$\Delta L = \frac{L\alpha^2(2 + g_1 + g_2)}{1 - g_1 - g_2} \quad (9.1)$$

where L is the length of the cavity and $g_1; g_2$ are related to the curvature of the mirrors, $R_1; R_2$, through $g_1 = 1 - L/R_1$ and $g_2 = 1 - L/R_2$. In addition to this second order term, a first order term will also be present if the mirrors are not perfectly aligned with the center of spacer. From geometrical considerations it is seen that for a mirror displacement δy this contribution will be:

$$\Delta L = \delta y \sin(\alpha), \quad (9.2)$$

To reduce the frequency change from vibrations, the cavity should be supported in a way which minimize both bending and expansion due to the Poisson effect. For simple structures, this problem can be solved analytically, but for complex structures this is not as simple. Instead, the cavity structure is analyzed with a finite element model using commercial software.

9.2.1 Introduction to Finite Element Analysis

To find the optimum position of the support holes, the deformation of the cavity is studied using a finite element model. In this kind of analysis, the structure is split up in a finite number of elements which are then treated as separate structures connected at the nodes. This is easily illustrated with a bar with length L and area A with one node at each end, where the displacement of these nodes are denoted u_1 and u_2 . The static equations will then be of the form:

$$\begin{bmatrix} k & -k \\ -k & k \end{bmatrix} \begin{Bmatrix} u_1 \\ u_2 \end{Bmatrix} = \begin{Bmatrix} F_1 \\ F_2 \end{Bmatrix} \quad (9.3)$$

Where $k = AE/L$ corresponds to the spring constant of the bar, E is Young's modulus and F_i are the forces at each end. If two of these elements are connected, it results in 3 nodes. For the first element, the equation would then read:

$$\begin{bmatrix} k_1 & -k_1 & 0 \\ -k_1 & k_1 & 0 \\ 0 & 0 & 0 \end{bmatrix} \begin{Bmatrix} u_1 \\ u_2 \\ u_3 \end{Bmatrix} = \begin{Bmatrix} F_1 \\ F_2 \\ F_3 \end{Bmatrix} \quad (9.4)$$

A similar equation can be written for the second element, and since the displacement is linear in the force, the equations for the entire system is obtained by adding these two matrices:

$$\begin{bmatrix} k_1 & -k_1 & 0 \\ -k_1 & k_1 + k_2 & -k_2 \\ 0 & -k_2 & k_2 \end{bmatrix} \begin{Bmatrix} u_1 \\ u_2 \\ u_3 \end{Bmatrix} = \begin{Bmatrix} F_1 \\ F_2 \\ F_3 \end{Bmatrix} \quad (9.5)$$

In a similar fashion, several elements could be attached one after another. The solution is found by imposing boundary conditions and solving the linear equation system. Imposing the boundary conditions: $u_1, u_3 = 0$ and $F_2 = 0$, for example, gives the simple solution $u_2 = 0$, simply because it is required that $F_2 = 0$, which will intuitively only be the case if it rests in its equilibrium position.

General structures containing more elements can be modeled in the same way. In 3D models, however, not only linear translation of the nodes is considered but also rotation around the nodes. A 3D model therefore contains six degrees of freedom per node. In exactly this manner, the cavity-structure can be split up in a number of elements, and the effect of gravity can be analyzed.

The listed approach is only valid when the deformation is elastic (the force is linear in displacement). Depending on the material, this is only the case for small displacements, but as the deformation of the structure only amounts to a few nanometers, this is a good approximation.

9.2.2 Analysis setup

The influence of gravity on the structure is analyzed by applying a force to each node corresponding to an acceleration of each element of 10 m/s^2 . Due to symmetry around the two planes in the centroid of the structure (yz,yx [Figure 9.4](#)), it suffices to simulate one quarter of the structure. This corresponds to imposing boundary conditions preventing movement of the nodes normal to these planes. All boundary conditions on the material interfaces are simply set by constraining the nodes to each other, except at the interface between the spacer and the Viton cylinder. This interface is difficult to describe correctly in linear analysis because the contact area depends on the deformation of the Viton cylinder. To determine a valid representation of the support, the contact area was determined iteratively to an area corresponding to a 5° angle at the top of the cylinder. The nodes on the spacer and the Viton cylinder were constrained on this area, and the center of the Viton-cylinder was constrained to zero vertical movement. The material properties were specified as given in [Table 9.1](#).

The static deformation of the cavity was analyzed for different combinations of the vertical and horizontal position of the support hole in order to determine the point where both tilt and axial deformation are minimized. It turned out, however, that the two had no common minimum. Due to the material removed to create the support holes, bending of the cavity also gave rise to a significant axial displacement due to asymmetry in the forces. This was solved by adding another four blind holes which compensate this displacement (see [Figure 9.4](#)).

9.2.3 Results

The calculated deformation of the cavity for varying location of the support hole is illustrated in Figure 9.5. The two graphs show that varying the vertical position of the hole only affects the tilt negligibly, and similarly for the horizontal position and the axial displacement of the mirror. Tilt and axial deformation is minimised with the support hole located at $\Delta y = 2.74$ mm and $\Delta z = 99.3$ mm, as measured vertically and horizontally, respectively, from the spacer center of mass. The deformation of the structure with the optimized support is illustrated in Figure 9.6b.

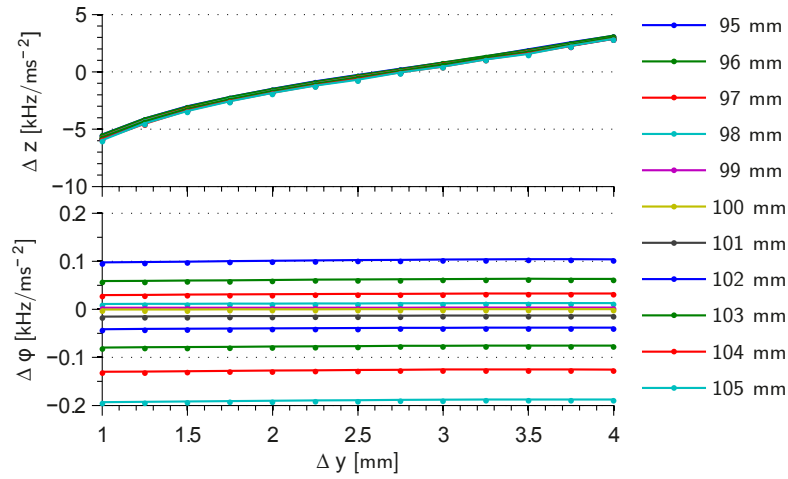


Figure 9.5: Axial deformation and tilt with varying position of the support hole. The horizontal axis corresponds to varying vertical distance between the centre of the spacer and the top of the support-hole. The different series correspond to varying horizontal distance from the middle of the spacer to the centre of the support hole (Figure 9.4).

Material	Young's Modulus	Poisson Ratio	Density
Zerodur	90.3 GPa	0.243	2.53 g/cm ³
Invar	140 GPa	0.29	8.15 g/cm ³
Steel	200 GPa	0.30	7.85 g/cm ³
Viton	0.5 GPa	0.45	2.15 g/cm ³

Table 9.1: Properties of materials used in the analysis. Youngs modulus of Viton is in reality much closer to 8 MPa; the modulus was artificially increased to reduce the deformation in the vertical direction which does not contribute to the result. It has been verified that this only affects the vibration sensitivity in the order of 3 Hz/ms⁻².

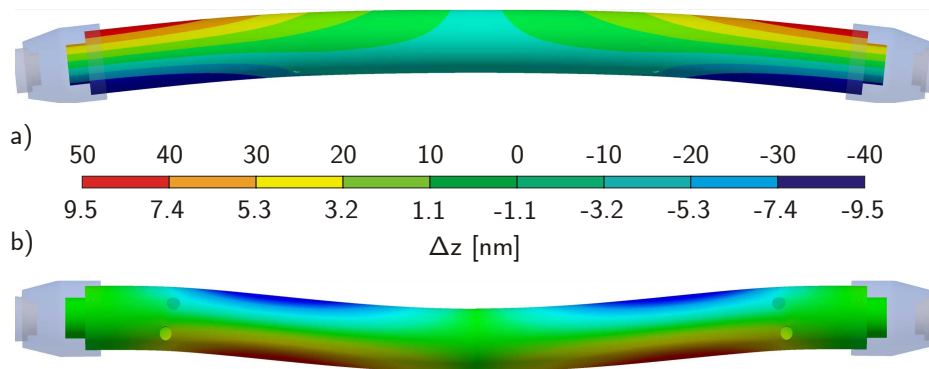


Figure 9.6: Illustration of the cavity deformation: a) supported at the Airy points b) with optimised support. Notice the different color-index scales. The deformation has been magnified to illustrate the deformation, but by different scales: a) 25.000 b) 100.000.

Evaluation of the expected accuracy

The deformation depends on the properties of the materials, and uncertainties in these will affect the results. In addition, inaccuracy in the description of the boundary conditions could further affect the accuracy of the results. By evaluating the vibration sensitivity with changing material properties, this uncertainty has been estimated to less than 1 kHz/ms^{-2} for a 10% variation.⁴ Changing the contact area (between the support hole and the viton cylinder) from 5° to 20° changes the result by 0.4 kHz/ms^{-2} .

In addition to deviations in the material properties, uncertainties in the results are expected due to the finite element nature of the analysis, but as the number of elements are increased, these variations are expected to decrease. Figure 9.7 illustrates the calculated vibration sensitivity with varying element size. The last point corresponds to the mesh used in the calculation of Figure 9.5, for which the uncertainty is estimated to 0.2 kHz/ms^{-2} .

Besides the uncertainties in the simulation, machining tolerances will affect how closely the actual structure resembles the model. By determining the derivatives in Figure 9.5, these tolerances can be translated to variations in the vibration sensitivity: $\Delta\nu/\Delta y = 2.4 \text{ kHz/ms}^{-2}/\text{mm}$ and $\Delta\nu/\Delta z < 4 \text{ Hz/ms}^{-2}/\text{mm}$ for $\Delta z = (99 \pm 1) \text{ mm}$. With expected machining tolerances significantly below 0.1 mm we expect a maximum deviation of 0.2 kHz/ms^{-2} .

Combing all the contributions, an overall uncertainty in the vibration sensitivity of the actual structure is expected to be less than 2 kHz/ms^{-2} . Compared to the calculated 1.3 MHz/ms^{-2} for the setup supported from below, this indicates a significant reduction in the vibration sensitivity.

⁴ The single most important property is the Poisson ratio of Zerodur, which for a 10% deviation changed the result by 0.6 kHz/ms^{-2} .

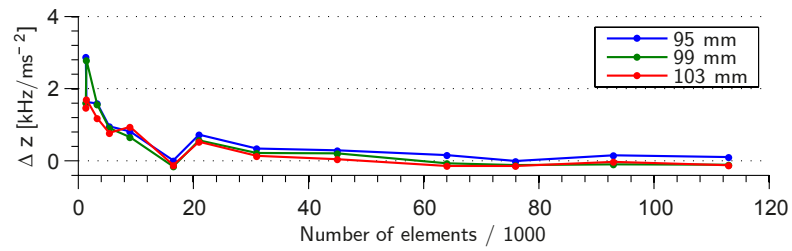


Figure 9.7: Vibration sensitivity with varying number of elements for $\Delta y = 2.74$ mm. The number of elements refers to the number of elements representing the cavity spacer. As the number depends on the geometry it is only approximate. The three series represent different horizontal positions of the support hole.

Setup and Measurements

The actual setup for stabilizing the laser is based on the principles of the previous chapters. This chapter contains a technical description of the realization of these techniques.

10.1 The Laser Source and Setup

The laser used to generate the 729 nm light is a commercial solution from Toptica.¹ The light is generated in an Anti-Reflection (AR) coated diode stabilized with feedback from a grating in the Littrow configuration. The grating is mounted on a Piezo-Electric Transducer (PZT) providing a mode-hop-free tuning range of ~ 60 GHz through feedforward to the current in the diode. The current in the diode is controlled externally with a knob and around this offset through a Field Effect Transistor (FET) mounted close to the diode for high frequency modulation. At maximum current, the diode produces 80 mW of light which is used to seed a Tapered Amplifier resulting in a maximum optical power of 0.5 W.

The light from the laser is separated in three branches, one for the experiment, one the resonator and one for the wavelength meter, as illustrated in Figure 10.1. The light for the resonator is deflected in a 600 ± 150 MHz Acousto-Optic Modulator (AOM) in double pass configuration providing a tuning range of 600 MHz for bridging between the modes of the resonator. After deflection in the AOM, the light is coupled to a Single Mode Polarization Maintaining (SM/PM) fiber which guides the light to the resonator platform. The experimental branch also uses an AOM in double pass for frequency shifting (200 ± 50 MHz) and pulse shaping, after which the light is guided to the experiment through an SM/PM fiber. The waist is matched to

¹ TA-100 Pro, Toptica GmbH.

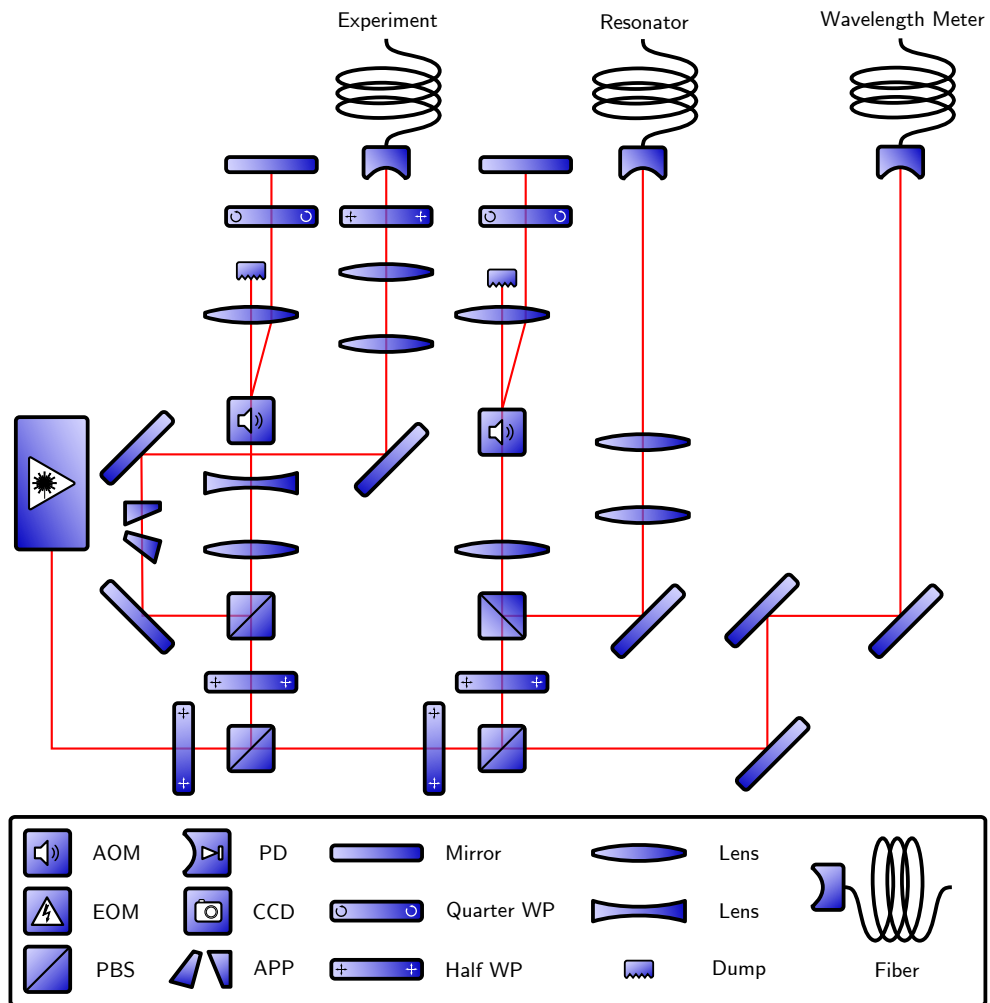


Figure 10.1: The optical setup for preparing the 729 nm light. The two branches for the resonator and experiment contain AOMs in double pass configuration for frequency shifting the light. The power is balanced between the branches with the half wave plates and polarization beam splitters.

the AOM with a telescope consisting of one convex ($f = 100$) and one concave ($f = -30$) lens and then retro-reflected by a mirror placed in the focal point of a third convex lens. Opposed to the common setup with the AOM placed in the focus of a 1:1 telescope, this configuration provides a large collimated beam in the AOM without requiring long focal length lenses which would otherwise be necessary to obtain good diffraction efficiency [64]. With this specified setup, a total double pass diffraction efficiency above 70% has been realized.

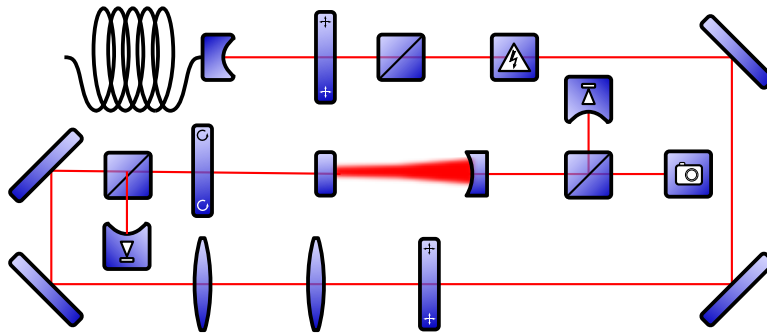


Figure 10.2: The optical setup for PDH detection. The entire setup is placed on a vibration damped platform to reduce low frequency deformation of the resonator.

10.2 The Optical Setup for Stabilization

The optical resonator is placed on a vibration damped platform to reduce low frequency deformation. The low frequency damping is realized with a heavy breadboard matched to shock absorbing feet² resulting in attenuation of frequencies below 30 Hz. To avoid misalignment problems due to the soft support, the light is delivered to the platform through an SM/PM fiber. After leaving the fiber the polarization of the light is purified with a half wave plate and a Glan Thompson Polarizer. This is important to avoid residual amplitude modulation in the following Electro-Optic Modulator (EOM)³. The EOM is driven with a frequency of $\Omega = 2\pi \cdot 20 \text{ Mhz}$ at an amplitude of 500 V_{pp} , resulting in modulation index of $\beta = 0.7$. The varying refractive index of the EOM modulates the phase of the light and introduces the required sidebands for PDH detection. Afterward, the light is guided around the chamber and matched to the cavity mode with two lenses. A quarter wave plate in front of the resonator rotates the polarization so that the reflected light is incident on the Photo Detector (PD). The light transmitted through the resonator is split by a 50:50 beam splitter onto a PD and a Charge-Coupled Device (CCD) based camera used for mode matching.

10.3 The Electronic System

The signal from the PD in reflection is mixed and low pass filtered to extract the amplitudes as discussed in Section 7.2. This signal is sent through a servo controller⁴ providing a variable lead and three lag regulators. The controller has a bandwidth of 100 MHz which is important to avoid additional phase

² Stud mounts made from Sorbothane, Sorbothane Inc.

³ PM25, Linos

⁴ FALC, Toptica

contribution from the controller itself. The signal from the servo controller is fed back to the FET controlling the current in the laser diode with a bandwidth from DC to 1 MHz. A separate branch is connected via an integrator to the PZT to aid compensation of slow deviations (< 10 Hz). Both branches are DC connected, but when the integrator is engaged, the large low frequency gain in this branch will eventually compensate slow drifts.

10.3.1 Transfer function of the open-loop system

As made clear in [Chapter 8](#), it is beneficial to know the transfer function of the open loop system in order to optimize the performance. For electronic circuits, this can be measured by modulating the input and measuring the output in the desired frequency range. For a laser system, this is not as trivial as it requires a measurement of the actual frequency with high accuracy. We have such a tool available with the resonator and the PDH technique, but when the laser is unlocked, its intrinsic frequency fluctuations are significantly larger than the linewidth of the cavity, and this will basically hide the actual modulation. One way to resolve this is to instead measure the closed loop transfer function for a well-known controller setting.⁵ The transfer function of the laser system can then be calculated as:

$$G_l(s) = \frac{T(s)}{(1 - T(s))G_c(s)}, \quad (10.1)$$

where $T(s)$ is the closed loop transfer function and $G_c(s)$ the transfer function of the controller, just as in [Chapter 8](#). It should be noted that this transfer function includes poles from both the laser system as well as the detection system (PDH). The result is shown in [Figure 10.3](#) including a theoretical model with poles at $\nu_c = 140$ kHz and $\nu_{\text{FET}} = 700$ kHz. These poles correspond well to the expected contributions from the cavity signal⁶ and the FET controlling the current in the diode. The increased phase delay at high frequencies is due to an intrinsic time delay in the system (optical + electrical propagation) and is modeled as a phase corresponding to a delay of 70 ns.

10.3.2 The Servo Controller

With a model of the open loop transfer function, the controller can be optimized with the techniques from [Chapter 8](#). To increase the bandwidth of the system and reduce overshoot, a lead regulator is introduced with a resulting phase advance around 1 MHz ($\nu_{\text{lead}} = 250$ kHz, $\beta = 1/6$). This makes it

⁵ It is crucial to disable all integrators/lag regulators and have a low feedback gain; otherwise the modulation will be small and difficult to detect.

⁶ For a cavity used in reflection, the sensitivity to frequency fluctuations will exhibit low pass behavior with a cutoff corresponding to the linewidth of the cavity $\nu_c = \nu_{1/2}$ [65].

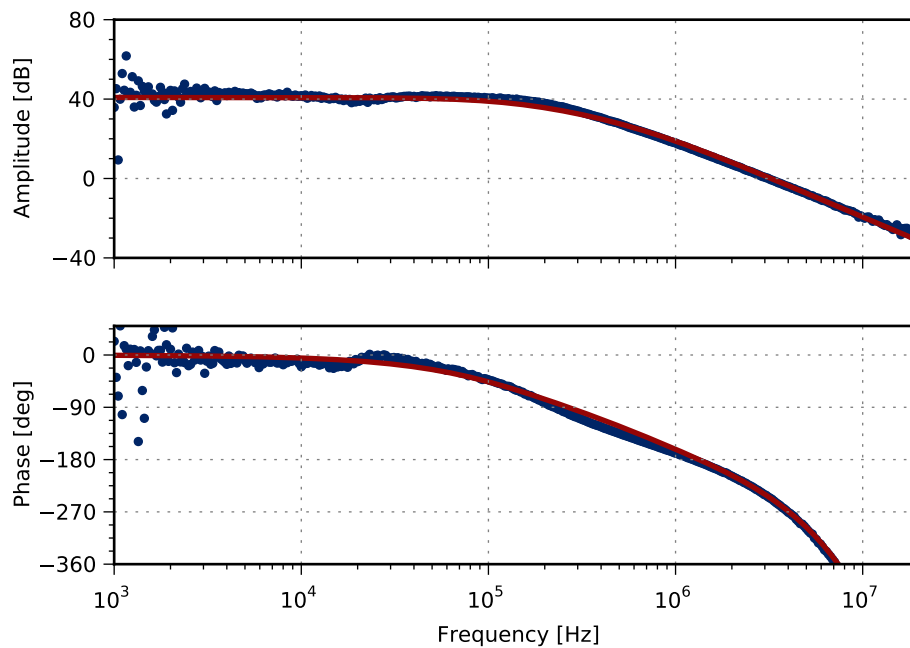


Figure 10.3: Open loop transfer function of the combined laser and PDH system • measured data; and — model with poles at $\nu_c = 140$ kHz and $\nu_{\text{FET}} = 700$ kHz (corresponding to the low pass characteristic of the cavity and the FET regulating the current in the diode) and a delay of 70 ns. At low frequencies, acoustic laser noise appears in the signal.

possible to increase the unity gain bandwidth to 3.7 MHz without significant overshoot.

Laser noise is typically dominated by large amplitude fluctuations at low frequency due to acoustic and thermal noise;⁷ to cancel these fluctuations a high gain at low frequency is advantageous. To achieve this, two lag regulators are introduced with $\nu_{\text{lag}} = 50$ kHz, $\alpha = 7$ and $\nu_{\text{lag}} = 3$ kHz, $\alpha = 60$ with a resulting DC gain increased by 50 dB. The cutoff of the high frequency lag regulator is chosen as high as possible without introducing additional phase delay at the unity gain frequency. The signal from the controller is used to modulate the current in the diode. A separate branch with an integrator is used to achieve even higher DC gain for compensating slow drifts. This signal is used to control the grating via the PZT.

⁷ This is actually seen in Figure 10.3 where the feedback loop is unable to compensate these fluctuations which appear as noise in the measurement.

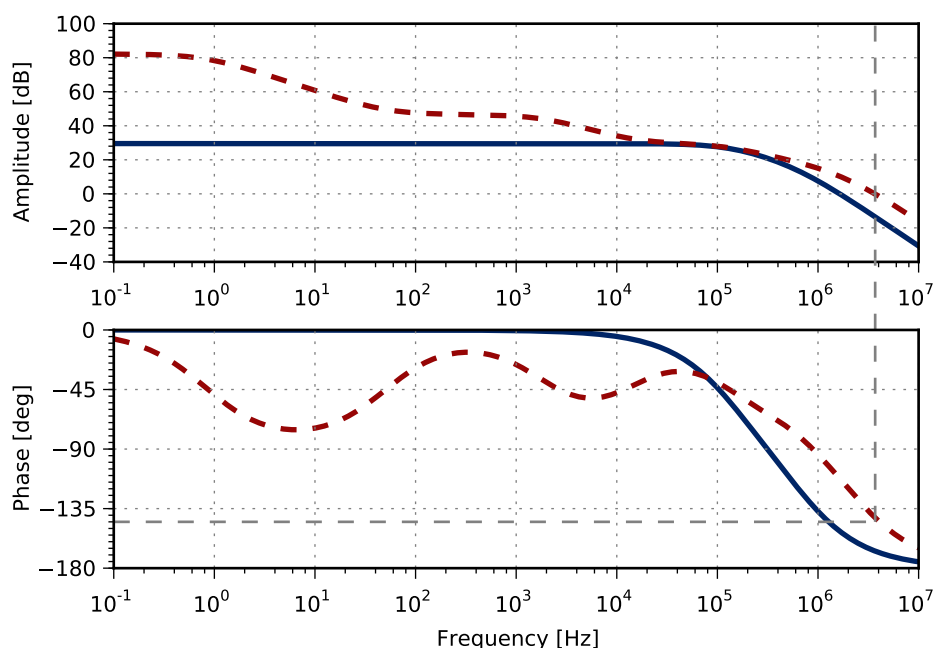


Figure 10.4: Transfer functions of — the laser system with an additional 30 dB gain; and - - the laser + controller. The lead regulator reduces the phase delay above 100 kHz and allows a larger unity-gain bandwidth. The lag regulators increase the low frequency gain by 50 dB.

10.4 The Stabilized Linewidth

The linewidth of the laser can be measured with spectroscopy on a resonator with narrower linewidth than the laser or by performing a heterodyne beat measurement with a similar laser system. Unfortunately, neither are readily available. Another alternative is to perform a homodyne beat measurement using an optical delay. This requires a delay comparable to the coherence length of the laser which for a linewidth of 100 Hz amounts to 3.000 km - also challenging to realize. Fortunately, it is possible to estimate the linewidth of the laser from the in-loop error signal keeping a few limitations in mind:

When the laser is locked, the feedback loop essentially suppresses frequency fluctuations at the resonator. If the resonator itself is noisy⁸ or additional noise is imposed somewhere in the system,⁹ this noise will be imprinted on the light from the laser without appearing in the error signal. As

⁸ The result in Section 9.2 indicates that the resonator noise should only contribute at the single Hz level.

⁹ One such source could for example be phase noise imposed in the fiber guiding the light to the resonator. This can be canceled through active compensation if required [66].

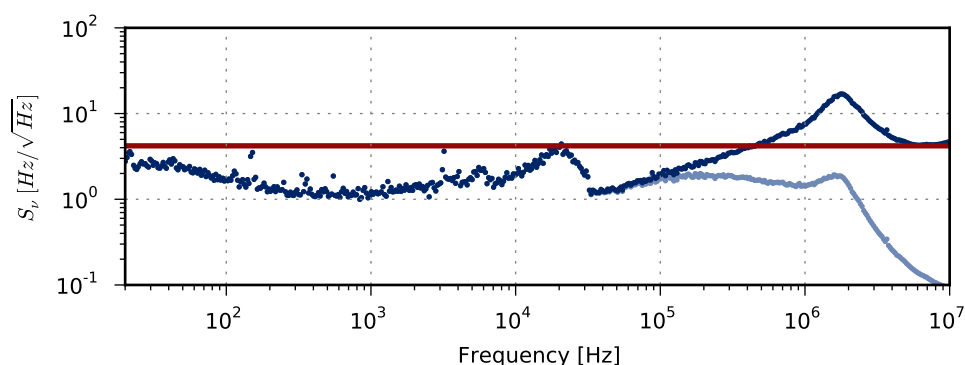


Figure 10.5: Noise Spectral Density of the PDH error signal. • the measured error signal; • corrected for low pass characteristic of the cavity ($\nu_c = 140$ KHz); - $S_v = 4.2$ Hz/ $\sqrt{\text{Hz}}$. Data above 10 kHz has been acquired with a calibrated spectrum analyzer and below through fast fourier transform of the signal from an oscilloscope. With $10 \mu\text{W}$ of light in the reflected sidebands, the shot noise limit is $\approx 10^{-2}$ Hz $\sqrt{\text{Hz}}$ [67].

long as these contributions are low, the linewidth measurement should be accurate.

Close to a resonance, the error signal is proportional to the frequency fluctuations of the laser as described in Section 7.2. Using Equation 7.14, it is possible to transform the in-loop error signal into absolute frequency variations of the light. The measured error signal transformed this way is shown in Figure 10.5.¹⁰

The spectrum reveals a pronounced peak around 1.7 MHz which originates from relaxation oscillations of the fast circuit branch due to increasing phase delay in the FET controlling the current in the diode. The red line corresponds to a white frequency noise floor of 4.2 Hz/ $\sqrt{\text{Hz}}$, which represents an upper bound for the noise density - except for the feedback oscillations. For white frequency noise, the optical power density is known to yield a Lorentzian lineshape with a width [68]

$$\Delta\nu = \pi S_v^2, \quad (10.2)$$

where S_v is the spectral density of the noise. For the indicated white noise floor this corresponds to a linewidth of 55 Hz. Even though the noise density is significantly larger around 1.7 MHz, this noise will not contribute much to the linewidth, as the modulation frequency is high. Integrating the noise density of the peak (200 kHz to 4 MHz) gives a total power of $7.9 \cdot 10^8$ Hz² corresponding to an RMS deviation of 28 kHz. Picturing this as a single frequency

¹⁰ In addition to estimate the linewidth such measurements are crucial for optimizing the feedback loop. By inspecting the error signal with a spectrum analyzer it is possible to determine in which frequency ranges the servo loop is struggling to suppress deviations.

modulation at 1.7 MHz indicates a modulation index of 0.016 which corresponds to fractional power in the sidebands of only $7 \cdot 10^{-5}$: this modulation only introduces minor sidebands around a central carrier with a linewidth of 55 Hz.¹¹

10.4.1 Actual Linewidth in the Experiments

The linewidth data was acquired one year ago. The experiments described in Part III were carried out with a significantly larger linewidth: Due to electronic problems with the amplified diode used to detect the PDH signal, high noise levels resulted in a linewidth closer to 40 kHz. With a non-amplified diode and increased optical power in the resonator, it was possible to reduce the linewidth to 4 kHz, required for the mass spectroscopy in Chapter 14 - though at the cost of increased thermal drift. The detector will be replaced in the near future and should allow the system to reach its original performance.

10.5 Long Term Stability of the Resonator

After realizing spectroscopy on the $S_{1/2} \leftrightarrow D_{5/2}$ transition, the long term stability of the resonator was investigated. The temperature sensitivity of the resonator is evaluated by changing the temperature of the copper tube surrounding the resonator. Figure 10.6 shows the evolution of the resonance frequency with respect to the $S_{1/2} \leftrightarrow D_{5/2}$ transition after a temperature change of 0.68 °C. The response shows a frequency change of 1.2 MHz corresponding to a temperature sensitivity of 1.8 MHz/K. This corresponds to a fractional expansion of the resonator of $4 \cdot 10^{-9}$ /K, which is below the maximum specified thermal expansion of the spacer (10^{-8} /K), indicating that the support and mirror mounts do not affect the performance negatively.

With the resonator placed in a temperature-stable environment, long term thermal expansion of the spacer is suppressed which is important for day to day frequency stability. An amorphous material such as Zerodur does however exhibit long term creep after a change in the loading conditions [71], which results in a gradual change in the length of the spacer. This is observed as a drift in the resonance frequency of the cavity as evident in Figure 10.7. The contraction is exponentially decaying with a half time of 150 ± 1 days resulting in a present drift rate of 5 Hz/s. This drift is predictable and used to calculate the expected position of the transitions on a daily basis.

¹¹ In experiments relying on ultra low linewidth and a series of short pulses (Ramsey-type experiments) these high frequency fluctuations can affect the interrogation through the optical Dick effect [69]. In this case it is possible to remove the high frequency noise using an optical resonator for filtering [70].

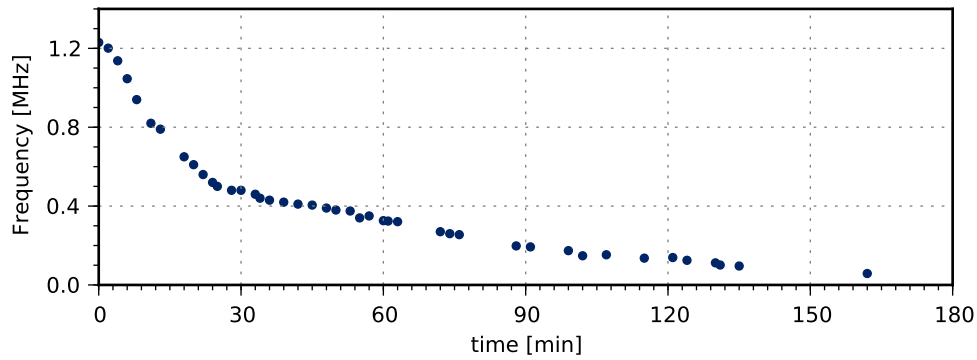


Figure 10.6: The evolution of the resonator frequency after an offset change in the temperature stabilization corresponding to $0.68\text{ }^{\circ}\text{C}$.

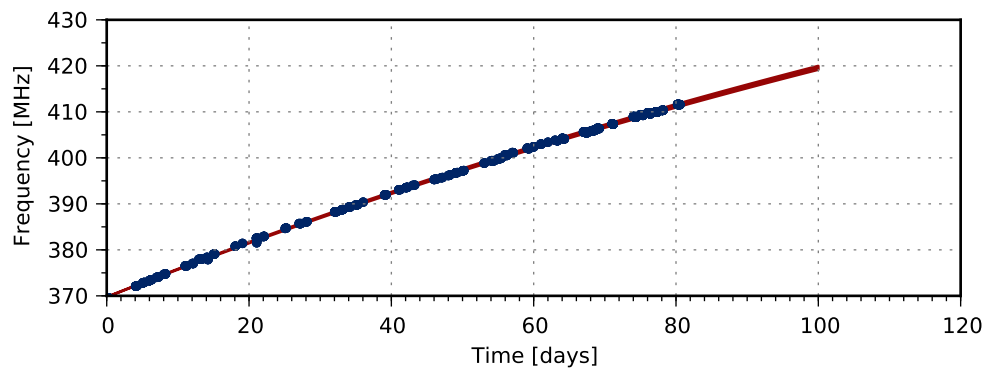


Figure 10.7: The position of the $S_{1/2}(m_J = -\frac{1}{2}) \leftrightarrow D_{5/2}(m_J = -\frac{5}{2})$ transition with respect to the resonator. The red colored area corresponds to an exponential fit and related uncertainties.

Part III

Experiments with Trapped Ions

Experimental Equipment and Methods

Experiments with trapped ions require equipment for generating, trapping and detecting ions in addition to several laser sources to achieve full control of the internal and external state of the ions. This chapter provides a brief description of these different parts of the apparatus and the general procedures used in the experiments.

11.1 Confinement of Ions

The ions used in the experiments are trapped in a linear Paul trap as described in [Chapter 2](#). This section contains a technical description of the actual trap apparatus and the technique used to obtain single atomic ions.

11.1.1 The Linear Paul Trap

The ions are confined in a linear Paul trap consisting of 4 segmented rods providing both RF and DC confinement (illustrated in [Figure 11.1](#)). The electrodes are made from gold coated stainless steel and are supported on a macro structure.

All electrodes are supplied with an RF potential for radial confinement and an axial-symmetric DC potential for axial confinement, connected as illustrated in [Figure 2.1](#). In addition to the symmetric potentials described in the figure, an offset potential can be applied to the individual rods to overlap the pseudo-potential with the DC minimum and minimize micromotion (and break the asymmetry in the radial oscillation frequencies). The DC potentials are supplied from a homemade linear supply providing potentials from 0 to 100 V.

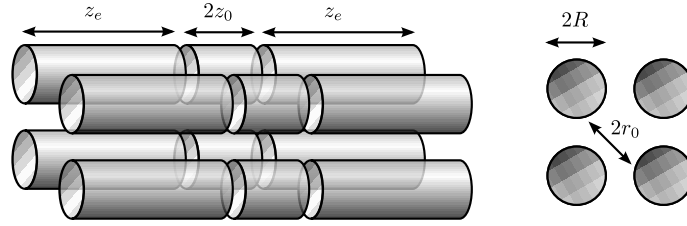


Figure 11.1: Illustration of the symmetrically driven linear Paul Trap in 2:1 scaling. The RF phase is identical on the individual segments of the rods and all eight endcap electrodes are at same DC potential. The four center electrodes are DC grounded. $r_0 = 3.5$ mm, $R = 4$ mm, $z_0 = 2.7$ mm and $z_e = 20$ mm.

The RF field is provided by an RF synthesizer¹ followed by an amplifier with an output up to 1 W. This signal is enhanced by a resonant RC circuit with a Q-factor of 12 resulting in RF voltages at the electrodes of up to 1.5 kV_{pp}. The RF signal is coupled to the electrodes through variable capacitors allowing individual adjustment of the amplitudes (phases) at each electrode. This allows the cancellation of dipole fields and has proved to be an important tool to minimize micromotion.

With the geometry illustrated in Figure 11.1, the geometric factors from Chapter 2 are $\gamma = 2 \cdot 0.248/z_0^2$ and $\alpha = 1/r_0^2$. For typical single ion experiments the trap is operated with $U_{RF} = 1.2$ kV_{pp} at $\Omega_{RF} = 2\pi \cdot 3.73$ MHz resulting in $q = 0.86$. With an endcap potential of $U_z = 80$ V this gives secular oscillation frequencies of $\omega_r = 1$ MHz and $\omega_z = 0.6$ MHz. Micromotion has been minimized to a modulation index below 10^{-1} in all directions by measuring the Rabi frequencies on the micromotional sidebands.

11.1.2 Vacuum System

The trap is operated inside a vacuum chamber at a typical background pressure of $3 \cdot 10^{-10}$ mbar maintained by a Leybold IZ 270 triode ion getter pump. The background pressure is continuously monitored by a AML UHV Bayard-Alpert ion gauge. The chamber is fitted with a leak valve which makes it possible to supply a continuous gas flow to the chamber with control of the final pressure with an accuracy better than 10^{-10} mbar. The leak valve is connected to two containers which are be filled with H₂ and D₂ for selective formation of ⁴⁰CaH⁺ and ⁴⁰CaD⁺.

¹ Agilent, 33210A

11.1.3 Generation of Ions

Single calcium atoms are obtained from metallic calcium placed inside a resistively heated oven at a temperature between 400 °C and 500 °C. At these temperatures the vapor pressure is sufficient to establish a constant flow of calcium atoms through a small opening. This opening is directed towards the center of the trap with additional skimmers to avoid unnecessary contamination of the electrodes. The atomic beam is overlapped with laser light at 272 nm in the center of the trap. The 272 nm light is generated by frequency quadrupling of infrared light from a commercial fiber laser [72]. Single calcium ions are generated by resonance-enhanced two photon ionization from $4s^2 \ ^1S_0$ through $4s5p \ ^1P_1$ to the continuum. Due to isotope shifts of the electronic levels, this ionization method makes it possible to selectively ionize different isotopes [73, 74].

11.2 Imaging System

When the atoms are ionized, they become resonant with the light at 397 nm and 866 nm, and they begin fluorescing. This fluorescence is used to detect the presence of the ions in the trap.

The fluorescence is collected with a custom lens system ($f = 70$ mm, $NA = 0.28$) onto a MCP based image intensifier² with a magnification of ~ 10 . The light from the image intensifier is imaged on a CCD chip³ with a commercial camera objective giving a final magnification of ~ 5 . The imaging system is placed above the trap (basically seeing the same image as in [Figure 11.2](#)). The Quantum Efficiency (QE) of the image intensifier is specified from the manufacturer to 20%, but independent measurements have indicated QEs closer to 5% with this intensifier type. The QE of this specific image intensifier has not been measured but will be investigated in future to optimize the data acquisition rate.

11.3 Optical Geometry and Light Sources

A geometric overview of the vacuum chamber is seen in [Figure 11.2](#). The axial direction of the trap is in the plane of the paper and the two radial axes are both aligned at angle of 45° to the plane of the paper. A single coil placed above the trap provides a magnetic quantization axis perpendicular to the plane of the paper. At a current of 2 A this gives a magnetic field

² Proxitronic, BV 2581 BY-V 1N

³ Sencicam QE, PCO

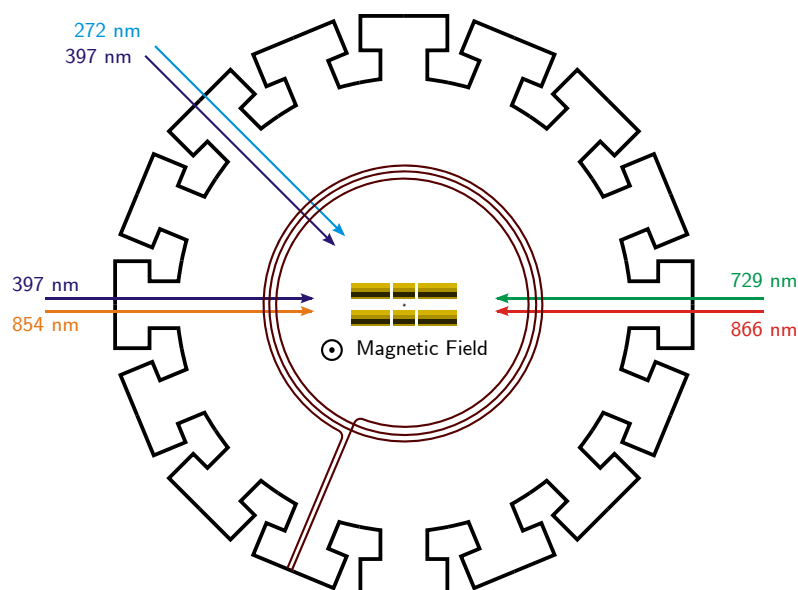


Figure 11.2: The optical paths near the trap. The trap is placed in the middle of the chamber with two of the principal axes of the trap aligned at 45° to plane of the paper and the axial direction in the paper plane. Power, spot sizes and polarizations are listed in table Table 11.1. A coil is placed above the vacuum chamber to generate a magnetic field perpendicular to the plane of the paper.

of approximately 0.4 mT corresponding to a Zeeman-splitting of the ground state of approximately $2\pi \cdot 10$ MHz.

To achieve full control of the internal state of the ions, it is necessary to address the $S_{1/2} \leftrightarrow P_{1/2}$, $S_{1/2} \leftrightarrow D_{5/2}$, $D_{3/2} \leftrightarrow P_{1/2}$ and $D_{5/2} \leftrightarrow P_{3/2}$ transitions as indicated in Figure 11.3. Typical powers, waists and polarization angles of the beams, which are all linearly polarized, are indicated in Table 11.1.

The light fields enter the vacuum chamber from different ports as indicated in Figure 11.2. All beams are perpendicular to the magnetic field and it is hence not possible to address specific magnetic sub-levels with polarization; the light will either be pure π -polarized or contain both σ^+ and σ^- components. State preparation is therefore achieved on the $S_{1/2} \leftrightarrow D_{5/2}$ transitions using frequency discrimination as discussed later.

The 397nm light used to address the $S_{1/2} \leftrightarrow P_{1/2}$ transition is split into two parts which enter the trap along the symmetry axis (0°) and at 45° . Most of the optical power is in the 45° beam which is used for ordinary Doppler cooling. With a 45° degree overlap with all three fundamental axes of the trap, this enables cooling of all the fundamental modes. The light field at 0° is unfocused and aids loading of new ions by illuminating of a larger part of the trapping volume. When the ions are cooled to the center of the trap, the

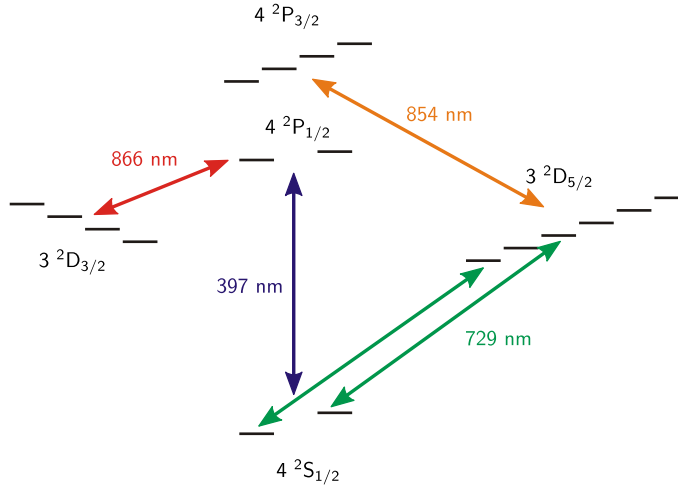


Figure 11.3: Level diagram of the $^{40}\text{Ca}^+$ -ion with driven transitions indicated by arrows; only the 729 nm transition addresses specific magnetic sub-states. The colors are consistent with Figure 11.2.

	397nm	866nm	854nm	729nm
w_0	600 μm	1 mm	1 mm	20 μm
P	800 μW	1.5 mW	2 mW	150 mW
γ	0°	90°	90°	45°

Table 11.1: Typical power, waist and angle between the polarization vector and the magnetic field vector for the different light fields (γ defined as in Section B.3).

light field at 45° will dominate the cooling with a much higher field intensity.

The 729nm light enters the chamber along the axis of the trap and is hence only sensitive to the motion of the ion along this direction. Two additional paths have been used to minimize micromotion in the perpendicular directions, but all results presented in this thesis have been obtained with the axial path. The light is polarized at $\gamma = 45^\circ$ with respect to the magnetic field. This enables coupling on all Zeeman transitions except for $\Delta m_J = 0$ transitions (see Appendix B.3 for a description of the geometric dependence of the coupling strengths).

11.3.1 Diode for 397nm

The light used to drive the $S_{1/2} \leftrightarrow P_{1/2}$ transition at 397nm is generated by a home built laser based on an AR-coated laser diode providing up to 20 mW of light. Lasing is achieved by external feedback from a grating in the Littrow configuration which gives a short term linewidth of a few hundred kHz. The

grating is placed on a small piezo stack for fine-tuning the wavelength. Slow fluctuations in the laser frequency are corrected with a feedback loop from a Fizeau-interferometer-based wavelength meter⁴ onto the piezo. With this setup the laser is absolutely stable within a few MHz. For shuttering and frequency control the light is deflected in an AOM in double pass configuration. This provides an extinction ratio above 10^9 , which is important to avoid unintentional scattering on the strong $S_{1/2} \leftrightarrow P_{1/2}$ transition. The light is finally coupled into an SM/PM fiber going to the trap table with a maximum power in the chamber just below 1 mW.

11.3.2 Diodes for 854nm and 866nm

The lasers for 854nm and 866nm light are constructed similarly to the 397nm laser and drift compensated with feedback from the wavelength meter as well. Shuttering is also obtain with AOMs, but in single pass configuration as the extinction ratio is not as important on these transitions. Both beams are coupled to SM/PM fibers guiding the light to the trap table.

11.3.3 Amplified Diode for 729nm

The laser driving the quadrupole transition at 729nm is based on a grating stabilized diode laser followed by a tapered amplifier providing 0.4 W optical power.⁵ The laser system is described in more detail in [Part II](#), which indicates the potential to reach linewidths below 100 Hz. Due to a malfunctioning photo detector, many of the experiments described in this thesis has however been carried out with a linewidth around 50 kHz. For the final experiments with molecular ions, the laser was optimized to a linewidth around 5 kHz (as discussed in [Section 10.4.1](#)). For pulse shaping and frequency control, the light is diffracted in an AOM in double pass configuration and finally guided to the trap table through a SM/PM fiber, resulting in a final power of up to 180 mW at the trap.

11.4 Control System

A typical sideband cooling sequence involves more than 1.000 optical pulses in a time window of a few milliseconds. To realize this, a new hardware system has been constructed together with a software framework to generate the pulse sequences. This system is described in more detail in [Appendix D](#).

The actual optical pulses are realized with AOMs as mentioned in [Section 11.3](#). The AOM used to modulate the 729 nm light is driven by a synthe-

⁴ WSU-2, HighFinesse, Germany

⁵ TA-100 Pro, Toptica

sizer capable of controlling both frequency and amplitude with a absolute frequency stability below 1 Hz. The other AOMs are used as on/off shutters, realized with Transistor-Transistor Logic (TTL) controlled RF switches. These RF signals are generated with conventional crystal oscillators and have a frequency stability around a few kHz.

11.5 Experimental Procedures

On a software level, each experiment is based on a set of building blocks as illustrated in Figure 11.4. These building blocks are combined depending on the actual experiments.

11.5.1 Doppler Cooling

Each experimental cycle starts with a Doppler cooling step to ensure equivalent starting conditions. Doppler cooling is performed on the 397 nm $S_{1/2} \leftrightarrow P_{1/2}$ transition with repumping on the 866 nm $S_{1/2} \leftrightarrow P_{1/2}$ transition.

In addition to cooling the ions, the scattered light is used to detect the ions. For this purpose a high scattering rate is preferable as this enables quick high fidelity detection. With a high scattering rate, the equilibrium temperature is increased due to power-broadening of the transition. Consequently, different powers and detunings are used in the sequence with 500 μW detuned -20 MHz for readout and initial Doppler cooling followed by 10 μW detuned -40 MHz in the final Doppler cooling stage (illustrated by the broken bar in Figure 11.4).

11.5.2 State Preparation

After Doppler cooling, the ion can be in either of the two magnetic substates of the ground state, $S_{1/2}$ ($m_J = -\frac{1}{2}$ or $m_J = +\frac{1}{2}$), with a slightly higher probability of being in the lower state due to different detunings with respect to the cooling light. To place it in a well defined state ($m_J = -\frac{1}{2}$), the ion is optically pumped on the $S_{1/2} \leftrightarrow D_{5/2}$ transition. This is accomplished by

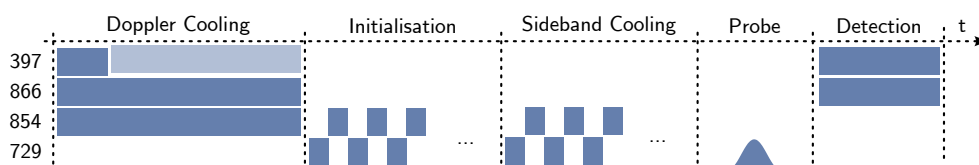


Figure 11.4: Typical experimental sequence. The individual parts are not to scale.

interleaved pulses on the $S_{1/2}(m_J = +\frac{1}{2}) \leftrightarrow D_{5/2}(m_J = -\frac{1}{2})$ transition and the $D_{5/2} \leftrightarrow P_{3/2}$ transition. Since only the population in the $S_{1/2}(m_J = +\frac{1}{2})$ state is excited, the ion will eventually end up in the $S_{1/2}(m_J = -\frac{1}{2})$ state. Typically a set of 50 pulses is used to assure a high fidelity independent of the motional state; more elaborate techniques using for example Rapid Adiabatic Pulses [75] could reduce the required number of pulses. As decay from $P_{3/2}$ to $D_{3/2}$ is also allowed, 866 nm light is applied simultaneously with the 854 nm light to empty the $D_{3/2}$ state.

State initialization on the $S_{1/2} \leftrightarrow D_{5/2}$ transition is slightly more complicated than using circularly polarized light on the $S_{1/2} \leftrightarrow P_{1/2}$ transition, but it comes with a great advantage: On the $S_{1/2} \leftrightarrow D_{5/2}$ transition the magnetic sublevels can be discriminated in frequency. This makes it possible to achieve high fidelity initialization without worrying about geometric alignment with respect to the magnetic field which would otherwise give rise to unwanted polarization components. During sideband cooling this also affects the achievable ground state population as these components would lead to scattering out of the ground state.

11.5.3 State Manipulation

With the ion placed in a well defined state, the actual experiments can be carried out with manipulation of the internal state using for example a single pulse with different frequencies for basic spectroscopy or varying duration to observe Rabi oscillations. The specifics of these manipulations will be described together with the actual experiments.

11.5.4 State Detection

After the state has been manipulated, the internal (or external) state must be determined to extract the result. The external state is determined by mapping it onto the internal state as explained in Section 4.3; in either case this comes down to detecting the internal state which is easily achieved by looking for scattered photons on the $S_{1/2} \leftrightarrow P_{1/2}$ transition as discussed in section Section 5.3. This fluorescence is detected using the CCD camera as mentioned in Section 11.2. Using the CCD chip for detection makes it possible to discriminate different ions spatially but limits the data acquisition rate due to the low quantum efficiency of the intensifier and a long readout time (30 ms) of the camera currently in use. With a typical exposure of 15 ms, the state can be determined with close to unity fidelity as seen in Figure 11.5. With the current quantum efficiency we are in a regime where spontaneous decay from the $D_{5/2}$ state begins to affect the readout fidelity - this is however not significant for the current work.

11.5.5 Averaging

Each successful sequence, as in Figure 11.4, results in a single projection of the atomic populations in the $S_{1/2}$ and $D_{5/2}$ states (bright/dark). This sequence is repeated N times (typically 100) for each data point to extract the population in the $D_{5/2}$ state, ρ_D . The parameters are then changed to match the next data point and the sequence is repeated once again. This happens for each data point in a data set. The variance of ρ_D for each data point is calculated according to the binomial variance $N\rho_D(1 - \rho_D)$.

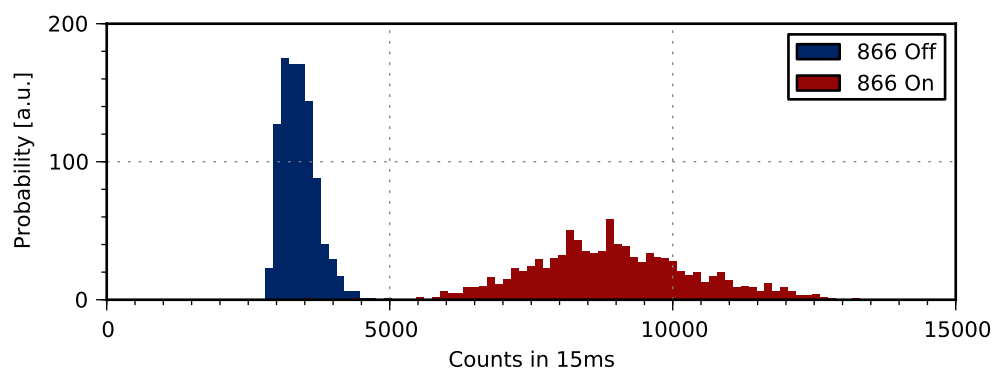


Figure 11.5: Histogram of detected CCD counts with 866 nm repumping on (blue) and off (red) with a detection time of 15 ms. When repumping is off, the ion is shelved in the $D_{3/2}$ state and does not fluoresce. This simulates the expected signal with the ion shelved in the $D_{5/2}$ state.

Sideband Cooling and Motional Dynamics

A large part of the experimental effort has been to characterize the system and optimize the parameters for sideband cooling. This chapter is dedicated to describing these characterizations together with the sideband cooling results for a single $^{40}\text{Ca}^+$ -ion.

12.1 Spectroscopy on the $S_{1/2} \leftrightarrow D_{5/2}$ Transition

The low natural decay rate of the $D_{5/2}$ state makes it possible to use this level for electron shelving, but it also provides sufficient frequency resolution to probe both the motion of the ion and its interaction with a magnetic field.

12.1.1 Zeeman Splitting

In a nonzero magnetic field, the electronic states split into a number of magnetic sub-states. Depending on the geometry between the magnetic field and the light field, different transitions between these sub-levels can be addressed (see Appendix B.3). Figure 12.1 shows one of the first spectroscopic signals acquired with this setup - it clearly shows coupling between different levels depending on the polarization of the light.

It is worth noting that the spectrum is severely affected by micromotion;¹ With no micromotion present, excitation would be limited to a few MHz (motional sidebands) around the different Zeeman transitions. This is particularly noticeable in the center of the spectrum where we would not expect any excitation as $\Delta m_J = 0$ transitions are not allowed in the current geometry.

¹ Compensation performed later indicated micromotion corresponding to a modulation index close to 5.

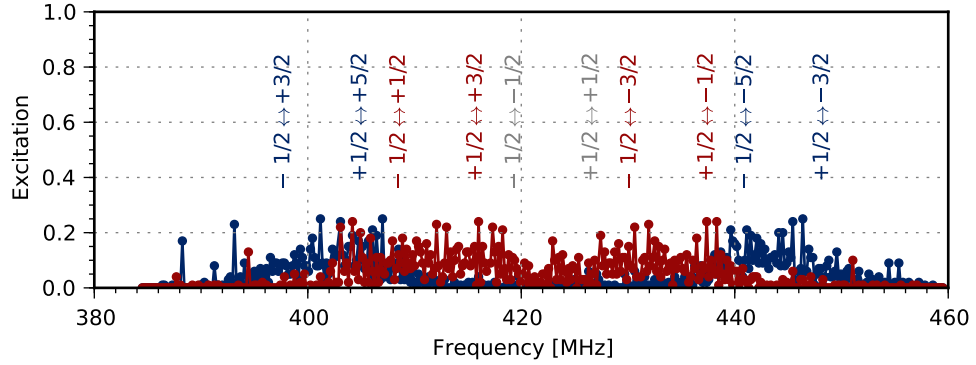


Figure 12.1: Spectroscopy showing magnetic substructure of the $S_{1/2} \leftrightarrow D_{5/2}$ transition with \bullet horizontal polarization ($\gamma = 90^\circ$) and \bullet vertical polarization ($\gamma = 0^\circ$). The expected position of the different zeeman transitions are also indicated.

12.1.2 Motional Sidebands

Below the magnetic structure an even finer structure is present, due to the secular motion of the ion as described in [Chapter 3](#). With an endcap potential of $U_z = 60$ V the theory in [Chapter 2](#) predicts an axial oscillation frequency of $\omega_z = 2\pi \cdot 0.5$ MHz. This is consistent with the separation of the sidebands in [Figure 12.2](#).

With the relatively shallow axial potential, Doppler cooling is only expected to bring the ion down to a final mean excitation number of $\langle n \rangle \sim 20$. This is observed in the spectrum with the first three sidebands clearly visible - the ion is certainly not in the Lamb-Dicke limit.

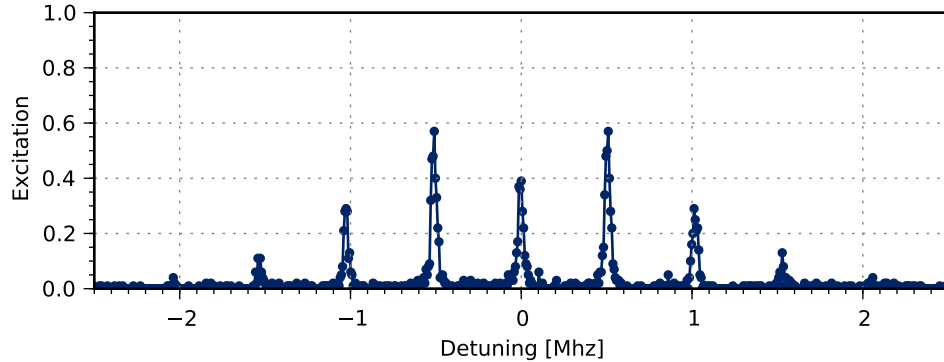


Figure 12.2: Motional sidebands of the $S_{1/2}(m_J = -\frac{1}{2}) \leftrightarrow D_{5/2}(m_J = -\frac{5}{2})$ transition at $U_z = 60$ V with a spacing between the sidebands of $\omega_z = 2\pi \cdot 505$ kHz.

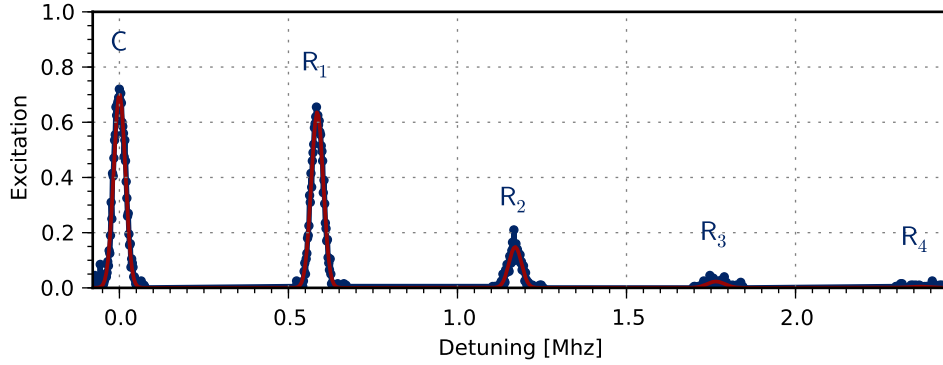


Figure 12.3: Carrier and first four sidebands after Doppler Cooling with a secular frequency of $\omega_z = 2\pi \cdot 0.585$ KHz and corresponding Lorentzian fits.

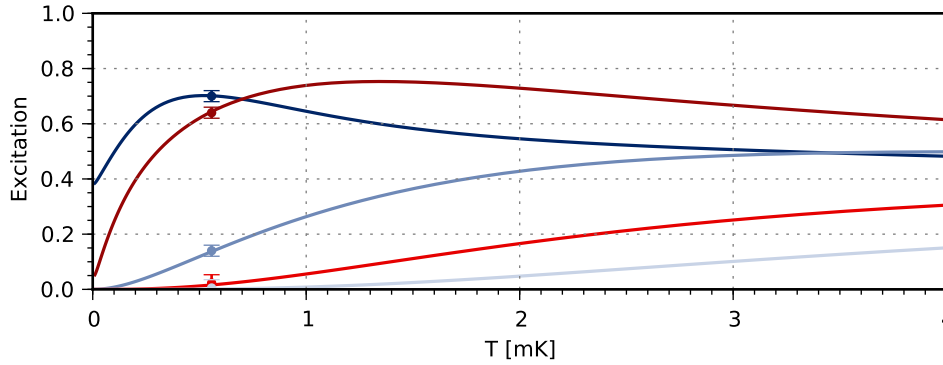


Figure 12.4: Calculated coupling strength [according to (4.25)] fitted to data points from Figure 12.3 with variable temperature, T , and pulse length, t .

12.2 Dynamics after Doppler Cooling

As explained in Section 4.3, the coupling strength on the different sidebands depends of the motional quantum state. By studying these dynamics it is possible to give a quantitative estimate on the motional state after Doppler cooling. Figure 12.3 shows a narrow scan over the carrier and the first four red sidebands after Doppler cooling. By comparing the strength of the sidebands to the theoretical expectations it is possible to get an indication of the temperature after Doppler Cooling. Figure 12.4 show the averaged coupling strength according to equation (4.25). The model has been fitted with variable temperature and pulse length (T, t) to the data points from Figure 12.3 resulting in $T = 0.56 \pm 0.01$ mK and $t = 1.59 \pm 0.01$, consistent with the Rabi frequency on the carrier after sideband cooling (Figure 12.8) and the expected Doppler Limit for $^{40}\text{Ca}^+$ of 0.5 mK.

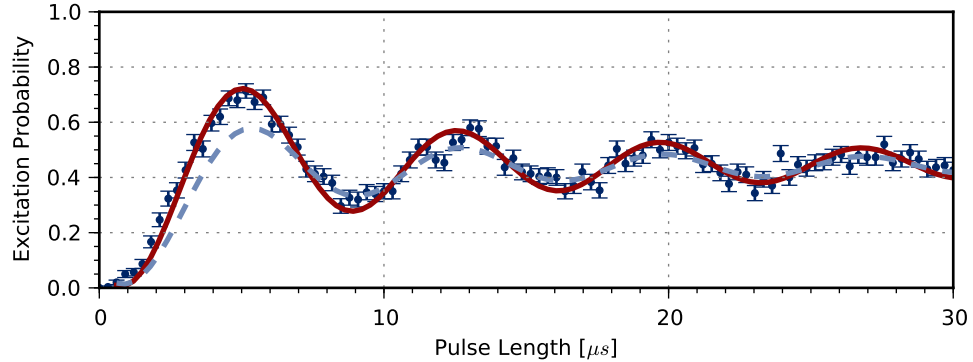


Figure 12.5: Rabi Oscillations on the carrier after Doppler Cooling. — Theoretical model with $T = 0.56$ mK and $\Omega = 2\pi \cdot 142$ kHz from Figure 12.4 and Figure 12.8. An additional offset phase ($\phi = 15^\circ$) is added to correct for initial nonlinear shuttering behavior. - Same model with $T = 1$ mK.

As mentioned in Section 4.3, the dephasing in the Rabi oscillations also reveals information about the motional distribution. Especially at low temperatures, this can be a rich tool as it is possible to map out the exact population of each state without assuming a thermal distribution [76]. In our case, however, the motional distribution is spread across many levels, and it is necessary to rely on a thermal model. With the temperature estimate from Figure 12.4 the expected dephasing can be modeled according to (4.23) which is shown in Figure 12.5.

The two methods might not necessarily agree if the distribution is non-thermal. We do however see a rather good agreement indicating a reliable temperature estimate. It is worth noting that, with a variable Rabi frequency, the data in Figure 12.5 can be matched to model temperatures as high as 0.9 mK. Using the independently measured Rabi frequency from Figure 12.8 does however require temperatures close to 0.56 mK for good agreement (illustrated by the dashed line in the Figure 12.5). This indicates that one should be careful when using the dephasing method to estimate temperatures at these elevated excitations - in this regime the sideband method appear more robust; it is not possible to reproduce the high temperatures with this model, even with a variable pulse length.

12.3 Sideband Cooling

After Doppler cooling the ion is in a thermal state with 20 motional excitations on average. This implies that the one percent of the population has more than 80 motional excitations, and obtaining a ground state population

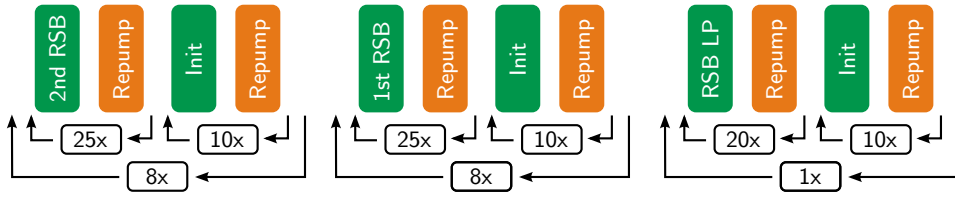


Figure 12.6: Sequence used for sideband cooling. Colors are consistent with Figure 11.3. The boxes indicate the number of repetitions for each sub-sequence.

close to unity requires more than 80 perfect cooling cycles - this naturally makes sideband cooling at low oscillator strengths challenging.

To efficiently transfer population from highly excited states, sideband cooling is initiated on the second red sideband. With alternating pulses on the $S_{1/2}(m_J = -\frac{1}{2}) \leftrightarrow D_{5/2}(m_J = -\frac{5}{2})$ and $D_{5/2} \leftrightarrow P_{3/2}$ transitions, the population is brought down to lower states (see Figure 12.6). Typically, 200 pulse cycles are applied before switching to the first red sideband with another 200 pulse cycles. Finally, the optical power is lowered to decrease off resonant scattering and another 20 cycles are applied to finalize the cooling process.

This specific Zeeman transition is chosen because it provides a nearly closed level scheme. From $D_{5/2}$, the ion is pumped back to $S_{1/2}$ via $D_{3/2}$. On these transitions, only $\Delta m_J = 0, \pm 1$ is allowed, which leaves a single route: $D_{5/2}(m_J = -\frac{1}{2}) \rightarrow P_{3/2}(m_J = -\frac{3}{2}) \rightarrow S_{1/2}(m_J = -\frac{1}{2})$. From $P_{3/2}$, the ion primarily decays back to the ground state, but occasionally, decay back to $D_{5/2}$ or $D_{3/2}$ can occur. In this case it is possible for the ion to eventually end up in $S_{1/2}(m_J = +\frac{1}{2})$. To avoid population trapping in this state, a few additional initialization pulses are applied for every 25 cooling cycles.

After sideband cooling, the sidebands are probed as seen in Figure 12.7, and the ground state population can be deduced according to Equation 4.22. With the current pulse scheme, the ion can be cooled to the ground state in 8 ms with a ground state populations as high as $P_0 = 0.99 \pm 0.01$. The excitation on the red sideband has been estimated from the average excitation around the line center. Inspecting the signal in detail does however reveal a rather constant background. Including this background in a Lorentzian fit results in a ground state population of $P_0 = 0.997 \pm 0.003$. This is slightly below the 0.999 achieved in the Innsbruck group [77], but with an axial oscillation frequency almost 8 times lower.

The coherent features of the system are also apparent in the wings of the blue sidebands as oscillations in the excitation for different detunings. The contrast of these oscillations is limited due to the finite linewidth of the laser and does therefore not extend to zero.

Due to the strong dependence of the Rabi frequency on the motional

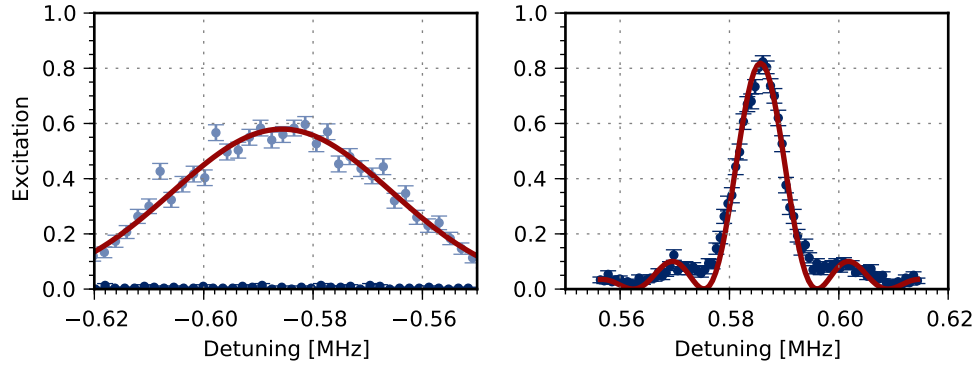


Figure 12.7: Excitation on the red and blue sideband: • before; and • after sideband cooling. The excitation around the blue sideband is modeled according to Equation 3.6. $P_0 = 0.99 \pm 0.01$, $\omega_z = 585$ kHz. The larger coupling strength at high excitations is evident by the broader line shape before sideband cooling.

quantum state (Figure 4.4), not every cooling cycle leads to removal of motional quanta; a significant reduction in the cooling duration could be available with an adaptive cooling scheme.

12.4 Dynamics after Sideband Cooling

After sideband cooling the ion is localized in a single motional state - the ground state. In this case, the coupling strength is well defined and the motional dephasing vanishes. This is observed in the Rabi oscillations in Figure 12.8 and Figure 12.9. Both figures include a fit to an exponentially decaying sinusoid indicating coherence times above 0.5 ms. Detailed inspection of Figure 12.9 indicates sudden jumps in the Rabi frequency (sudden horizontal offsets). This is attributed to problems with the feedback loop of the laser (see Section 10.4.1) due to fluctuating offsets in the lock signal. We observe a faster decay in the contrast than other experiments with $^{40}\text{Ca}^+$ [77], but this is expected with the current laser linewidth.

12.5 Motional Decoherence

If the secular motion is used as a quantum bus, motional coherence is crucial. The heating rate out of the ground state can be measured by sideband cooling the ion to the ground state and performing sideband spectroscopy after a variable delay. At longer delays, more population is excited out of the ground state and the red sideband increases as seen in Figure 12.10. By comparing the strength of the red and blue sidebands, the average number of motional

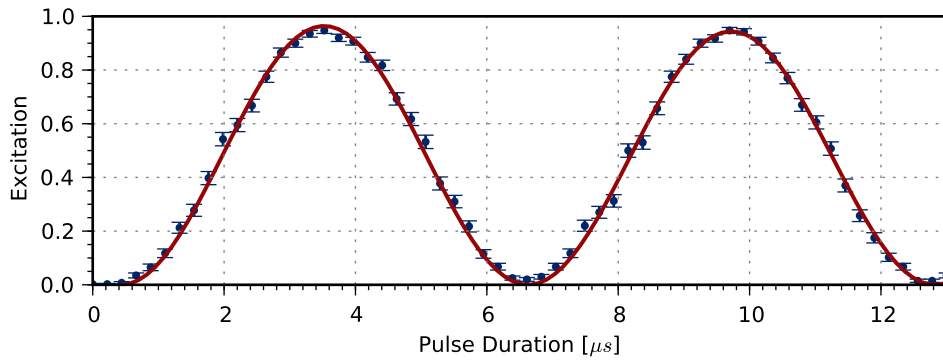


Figure 12.8: Rabi Oscillations on the carrier of the $S_{1/2}(m_J = -\frac{1}{2}) \leftrightarrow D_{5/2}(m_J = -\frac{5}{2})$ transition after sideband cooling.

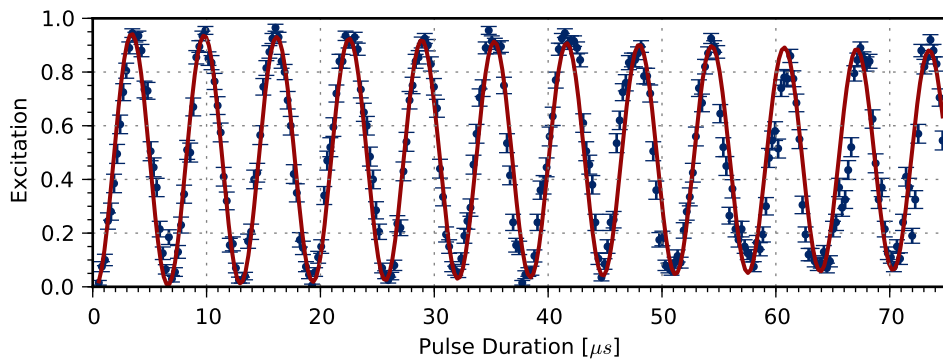


Figure 12.9: Rabi Oscillations on the carrier of the $S_{1/2}(m_J = -\frac{1}{2}) \leftrightarrow D_{5/2}(m_J = -\frac{5}{2})$ transition after sideband cooling.

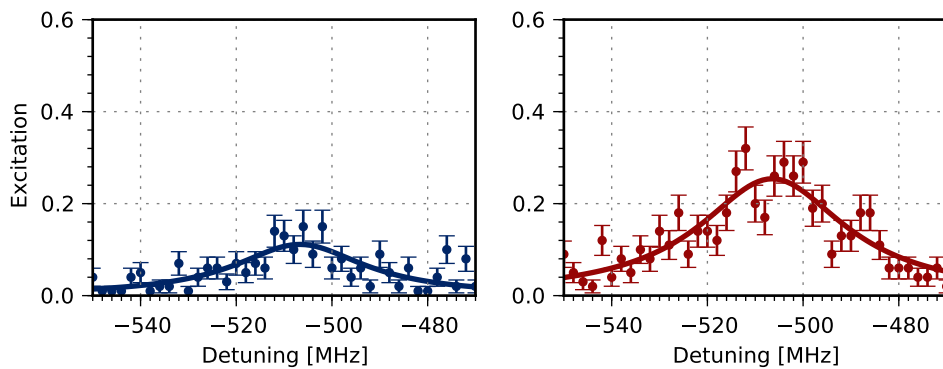


Figure 12.10: Excitation on the red sideband with different delays and an axial oscillation frequency of $\omega_z = 505$ kHz: \bullet $\Delta t = 100$ ms; \bullet $\Delta t = 500$ ms. .

excitations can be deduced for different delays as pictured in Figure 12.11a. This measurement indicates a heating rate of 1.5 ± 0.1 motional quanta per second.

To rule out heating contribution from spurious scattered 397 nm photons, the heating rate was measured with an additional mechanical shutter in the optical path. Due to mechanical inertia, the shutter does not close instantly. Independent measurements show that a maximum exposure of 15 ms should be present and should hence not be important at large delays. The measurements with and without the mechanical shutter are shown in Figure 12.11b with heating rates of 0.83 ± 0.10 /s and 0.84 ± 0.05 /s respectively indicating that contribution from spurious scattered photons are negligible.

The heating rate appears relatively constant over the measured range of secular frequencies except for a single point at 295 kHz as seen in Figure 12.12. The source of this increased heating is still unknown, but it does not appear to be a parametric resonance given that the axial oscillation frequency is not an integer multiple of the RF drive ($\Omega_{\text{RF}} = 2\pi \cdot 3.73$ MHz) and that the heating is consistent for different RF amplitudes. Neither did the DC supply show any extraordinary noise around this frequency. Except for these outliers we observe a rather constant heating rate around 1 motional quanta per second.

Motional heating has been subject to a widespread study in the ion trapping community after it was realized that the actual heating rates were several orders of magnitude higher than that expected from pure Jonson noise [78]. The additional heating, which was termed “anomalous heating”, is expected to arise from thermally activated fluctuating patch potentials on the

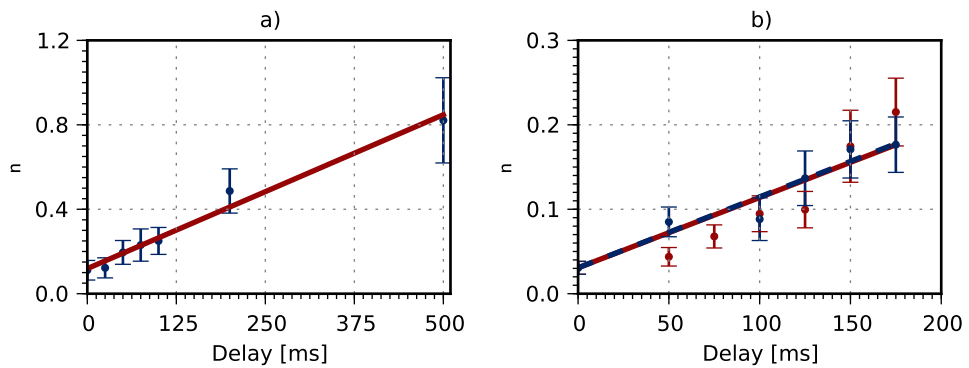


Figure 12.11: Average motional quantum number as a function of delay between ground state cooling and sideband probe. a) $\omega_z = 2\pi \cdot 505$ kHz. ■ linear fit with $d\langle n \rangle / dt = 1.5 \pm 0.1$ /s. b) $\omega_z = 2\pi \cdot 585$ kHz • with mechanical shutter; • without mechanical shutter. Corresponding fits: ■ $d\langle n \rangle / dt = 0.83 \pm 0.10$; • $d\langle n \rangle / dt = 0.84 \pm 0.05$.

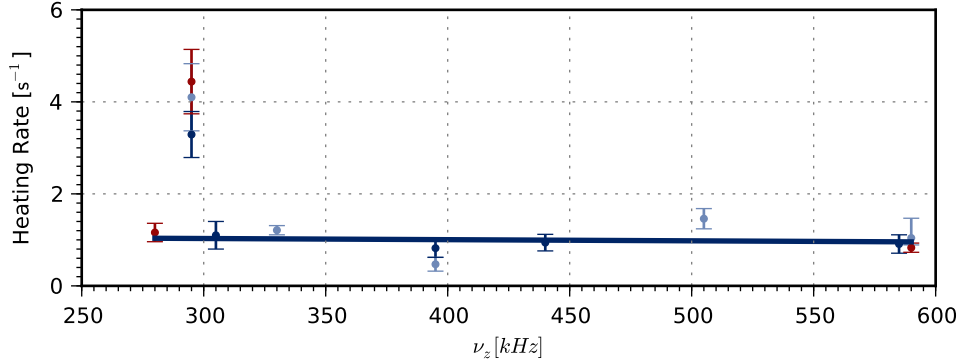


Figure 12.12: Heating rate of the axial motion for different oscillation frequencies. • measured on a single day; • measured on different days within two months • with alternate RF voltage. — linear fit to points except outliers at 295 kHz ($\beta = 1.1 \pm 0.35$ /s).

electrodes with a noise spectral density, $S_E(\omega_z)$, scaling as $1/d^4$ [79]. For heating induced by electric field noise, the heating rate along the rf-free axis is given by [80]

$$\frac{dn}{dt} = \frac{q^2}{4m\hbar\omega_z} S_E(\omega_z), \quad (12.1)$$

where q is the charge and m the mass of the ion. Previous measurements in smaller traps indicated an $1/\omega_z$ scaling of $S_E(\omega_z)$, resulting in a heating rate scaling as $dn/dt \propto 1/\omega_z^2$ [79, 81]. This differs from our measurements where we observe a constant heating rate which indicates an electric field noise density scaling as $S_E(\omega) \propto \omega_z$. The source of this field noise is yet undetermined, but the frequency scaling indicates that another noise source than fluctuating patch potentials is dominating.

To compare the heating rate with other traps, we neglect the frequency scaling observed in our experiment and assume the typical $1/\omega_z$ scaling of the noise density by comparing $\omega S_E(\omega_z)$ as illustrated in Figure 12.13. The rightmost point corresponds to the currently measured heating rate at a secular frequency of $\omega_z = 2\pi \cdot 270$ kHz. Compared with the spread of the measurements, our data is compatible with the $1/d^4$ trend-line. We notice that the electric field noise is almost two orders of magnitude lower than other measurements (the closest measured at cryogenic temperatures) which could explain why another noise source is dominating in our trap.

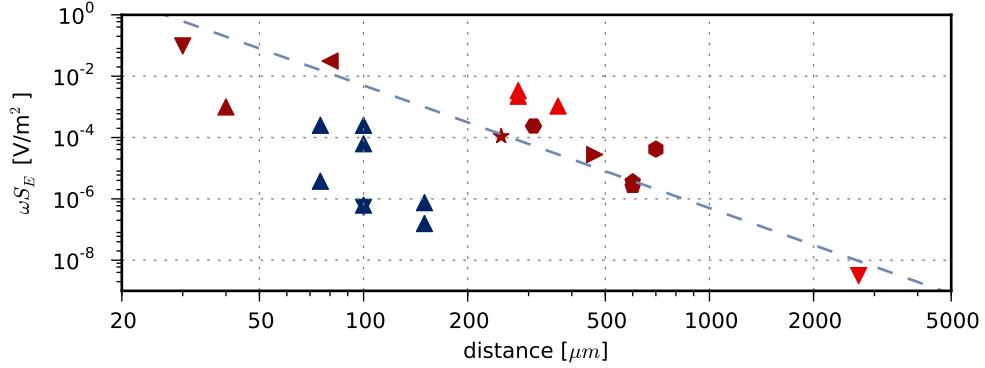


Figure 12.13: Summary of the motional heating in different traps including a $1/d^4$ trend line. Labels indicate ion species and trap material. Red points measured at room temperature and blue points at 6 K. \blacktriangle $^{24}\text{Mg}^+$, Au [82]; \blacktriangledown $^{111}\text{Cd}^+$, GaAs [83]; \blacktriangleleft $^{137}\text{Ba}^+$, Be-Cu [84]; \blacktriangleright $^{198}\text{Hg}^+$, Mo [85]; \blacklozenge $^{40}\text{Ca}^+$, Mo [86]; \star $^{40}\text{Ca}^+$, Au [87]; \bullet $^{171}\text{Yb}^+$, Mo [88]; \bullet $^{174}\text{Yb}^+$, Au [89]; \blacktriangle $^9\text{Be}^+$, Au [90]; \blacktriangle $^{88}\text{Sr}^+$, Ag 6K [80]; \blacktriangledown $^{88}\text{Sr}^+$, Al 6K [91]; \blacktriangledown $^{40}\text{Ca}^+$, Au [Current work].

12.6 Conclusion

The results in this chapter demonstrate the feasibility of performing sideband cooling in a macroscopic trap at low secular potential. This has two obvious advantages: Firstly, a macroscopic trap of this size is easier to combine with other equipment, e.g. for generating molecules or highly charged ions, due to more available room and looser tolerances in the assembly and alignment process. A macroscopic trap furthermore benefits from simpler trapping of ions from external sources with a larger trapping volume and deeper potential. With a typical trap depth in the order of 50 eV, it should be possible to confine ions with an initial energy corresponding to 10^6 K. Comparing this energy with that of the ground state ($2 \cdot 10^{-9}$ eV), ground state cooling essentially reduces the energy by a factor of $2 \cdot 10^{10}$. Secondly, cooling at a low secular potential is valuable if the final kinetic energy is important, since the zero-point energy scales with the secular oscillation frequency. The lower secular potential also makes the motional state more sensitive to recoil from scattered photons due to an increased Lamb-Dicke factor - this is advantageous for SRS of lines where the sidebands are indistinguishable.

The macroscopic size of the trap also results in a low heating rate. In the secular oscillation frequency range from 270 kHz to 590 kHz we observe a very low heating rate, typically around one motional quantum per second - to our knowledge the lowest heating rate measured in a Paul trap, even at cryogenic temperatures. This has several obvious advantages: Firstly, the very low heating rate makes it straightforward to extend the cooling to all

3 dimensions. Cooling of additional modes is typically achieved by subsequent steps, in which heating of the previously cooled modes limits the achievable ground state population. With a low intrinsic heating rate this should not cause problems except for recoil heating which can be counteracted by additional cooling cycles. Additionally, it should be possible to reduce the zero-point energy even further by adiabatically reducing the secular potential as described in the following chapter; with a low heating rate it should be possible to go to very low potentials.

CHAPTER 13

Adiabatic Cooling

For a sideband-cooled ion, the lowest achievable energy is set by the zero point energy of the quantum mechanical ground state. A possible solution to achieve even lower energy is through adiabatic lowering of the trap potential. This was proposed just after the first experiments with sideband cooling were demonstrated [92], but has to our knowledge not yet been studied in detail. A similar technique has however been used recently to realize transport of ions in segmented traps [93, 94, 95]. In addition to reducing the zero-point energy, adiabatic lowering of the potential can be used as a simple tool to achieve temperatures below the Doppler limit - in this chapter, both techniques are investigated.

13.1 Doppler Cooled

Adiabatic cooling of Doppler cooled ions is achieved with the sequence illustrated in Figure 13.1. After the usual Doppler cooling and state preparation, the endcap potential is adiabatically lowered. At low potential the sideband spectroscopy is used to determine the motional distribution and confirm adiabaticity. Finally, the potential is raised and the sequence is repeated.

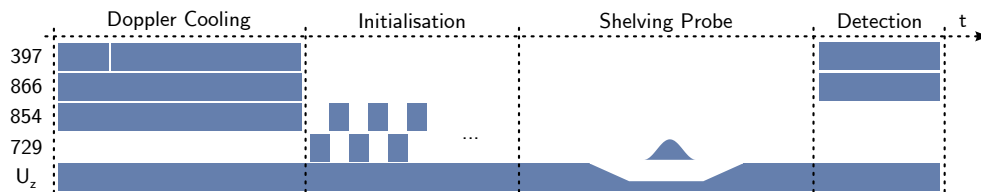


Figure 13.1: Sequence for adiabatic cooling of a single Doppler cooled ion. The individual parts are not to scale.

The carrier and first four red sidebands measured in the initial potential are illustrated in Figure 13.2. It is clear that the higher order sidebands in this measurement are stronger than in Figure 12.3 which is due to less efficient Doppler cooling.¹ The strengths of the sidebands are (as in Section 12.2) used to estimate a final temperature of 1.6 mK (see Figure 13.3).

With perfect adiabatic lowering of the potential, the motional distribution should remain unchanged, but the relative strength of the sidebands should change with the secular frequency. By assuming that the motional distribution is left unchanged, we can calculate the expected excitation on the motional sidebands after lowering the potential from Equation 4.25. This model is shown in Figure 13.4 together with the experimental data for an adiabatic lowering of the potential from $U_z = 80$ V to $U_z = 20$ V.

The dotted curve is calculated for a motional distribution with the same temperature as in Figure 13.3 (energy conserved).² The third and fourth sideband show significantly reduced strength indicating a lower temperature as expected. There is, however, a noticeably disagreement around the carrier. These data points were acquired last, and the discrepancy could be related to laser problems.

The reduced temperature becomes even more apparent when the endcap potential is lowered further to $U_z = 6$ V as illustrated in Figure 13.5. For this data set there is a good correlation between the experimental data and the theoretical model which suggest a temperature reduced by a factor of $\sqrt{80\text{ V}/6\text{ V}} = 3.7$ below the ordinary Doppler limit.

¹ The adiabatic data was acquired before the data presented in Chapter 12. In between a significant improvement in Doppler cooling was achieved with a better combination of detuning and optical power.

² This corresponds to the expected temperature for Doppler cooling in the low potential.

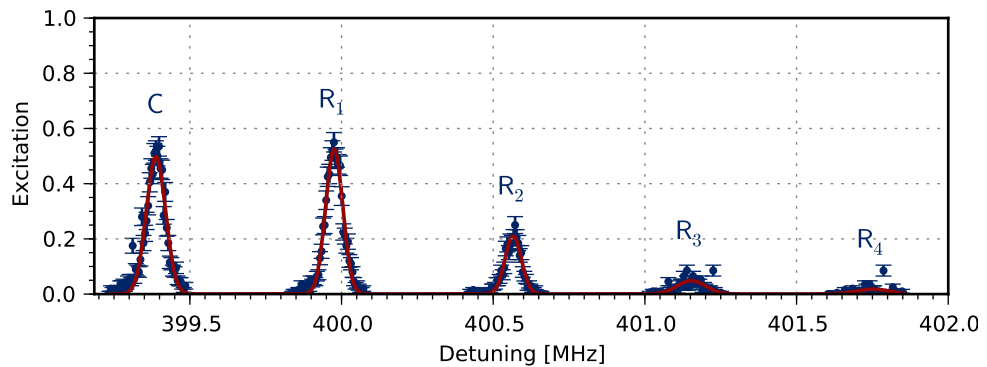


Figure 13.2: Sidebands after Doppler cooling before adiabatic tests. Line shapes with fits to Lorentz distributions.

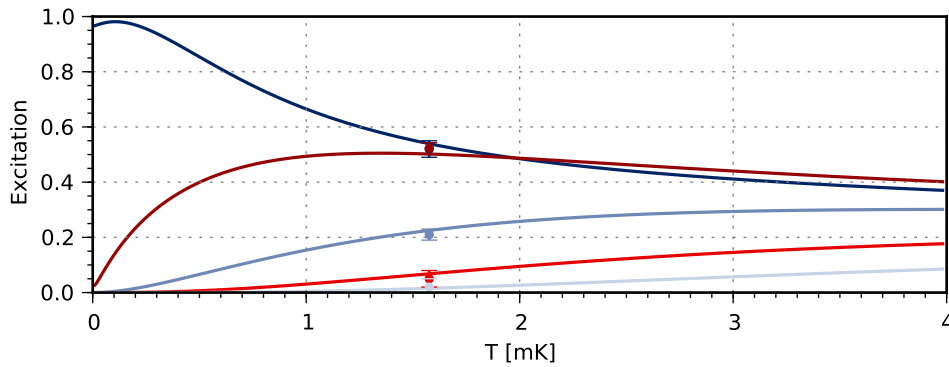


Figure 13.3: Calculated average coupling on: ■ Carrier; ■ 1st RSB; ■ 2nd; ■ 3rd; ■ 4th, for a pulse length of $t = 1.12$ resulting in a temperature of $T = 1.6 \pm 0.1$ mK.

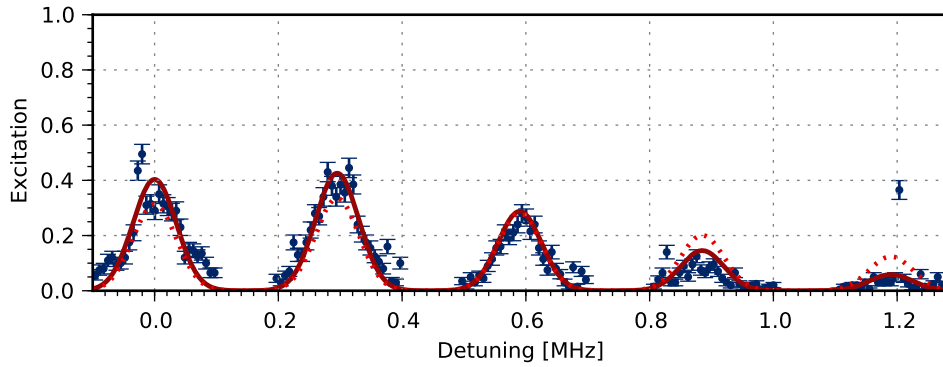


Figure 13.4: Sideband spectrum after adiabatic lowering of the endcap potential from $U_z = 80$ V to $U_z = 20$ V ($\omega_z = 2\pi \cdot 293$ kHz). The full line is the expected spectrum for perfect adiabatic cooling and the dotted line for the expected thermal distribution with same temperature as in Figure 13.2.

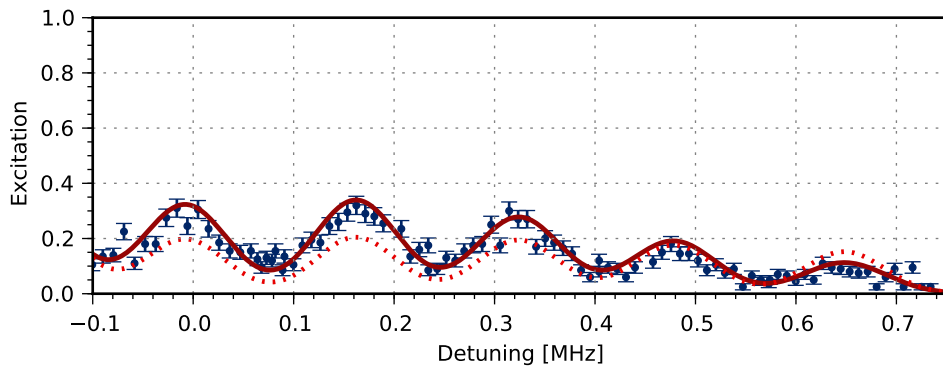


Figure 13.5: Sideband spectrum after adiabatic lowering of the endcap potential from $U_z = 80$ V to $U_z = 6$ V ($\omega_z = 2\pi \cdot 162$ kHz). Theoretical curves as in Figure 13.4.

13.2 Sideband Cooled

For ions cooled to the motional ground state, confirming adiabaticity is even simpler, as heating is easily observed as an increase in the strength of the red sideband. The sequence for this procedure is illustrated in Figure 13.6. This sequence starts with usual Doppler cooling, state initialization and sideband cooling. Once the ion is cooled to the motional ground state, the potential is adiabatically lowered, and after a short delay, the potential is returned to its initial value. Afterward, the red and blue sidebands are probed to detect a possible increase in the strength of the red sideband.

For an ideal adiabatic process, there should not be any change in the excitation on the red sideband. Unfortunately, the circuit used to combine the RF and DC potentials has an intrinsic low pass characteristic which inhibits a fast change of the potentials and limits the procedure to a duration of 200 ms. This results in significant heating and the excitation on the red sideband will be present even if the potential change in itself is adiabatic. The sidebands before and after the adiabatic procedure is illustrated in Figure 13.7.

During the adiabatic procedure, the excitation on the red sideband increases, corresponding to a change in the average motional quantum number of $\langle n \rangle = 0.27 \pm 0.03$. This is consistent with the heating rate from Figure 12.12 within the uncertainty and indicates that the potential change does not necessarily introduce additional heating.

At the reduced potential, the secular oscillation frequency of the ion is $\omega_z = 2\pi \cdot 162$ kHz. Relating the average kinetic energy of the secular motion, $(\langle n \rangle + 1/2)\hbar\omega_z/2$, to a corresponding temperature through the equipartition theorem, $m\langle v^2 \rangle/2 = k_B T/2$, results in a kinetic energy corresponding to only $6.7 \mu\text{K}$ for $\langle n \rangle = 0.27$. Such low temperatures can be very interesting for studying ultra-cold chemistry [28]. Though it is possible to reduce the potential even further, the linewidth of the laser limited the ability to confirm such potentials (see Figure 13.5). With an improved laser linewidth, it should be possible to study even lower potentials.

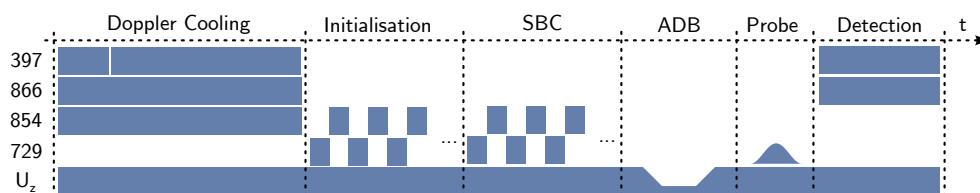


Figure 13.6: Sequence for investigating adiabatic lowering of the trap potential with a single sideband cooled ion.

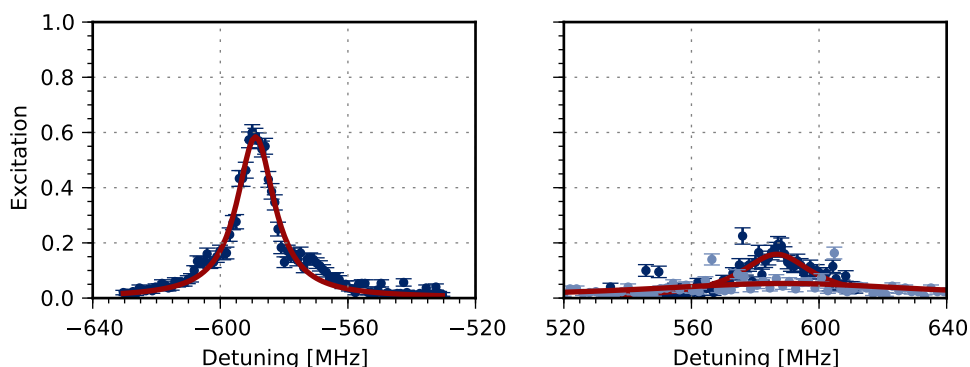


Figure 13.7: The red and blue motional sidebands for: • ordinary sideband cooling ($\langle n \rangle = 0.10 \pm 0.01$) and • after adiabatic cycle of the endcap potential to $U_z = 6$ V ($\langle n \rangle = 0.37 \pm 0.03$).

13.3 Conclusion

The results in this chapter demonstrate adiabatic cooling of a single trapped ion from both Doppler and sideband cooled initial conditions.

After Doppler cooling, the secular potential was reduced to 7.5% of the initial value with sideband strengths corresponding well to an adiabatic process. This indicates a thermal energy reduced by a factor of 3.6 and illustrates the feasibility of using potential changes to reduce the kinetic energy below the Doppler limit. Due to the large linewidth of the laser, the sidebands are only just distinguishable at the lowest potential; with an improved linewidth (as discussed in Section 10.4.1) we will be able to investigate the process at even lower potentials.

Adiabatic lowering of the secular potential has also been investigated with a sideband-cooled ion. The adiabatic process was limited by the electronics to a regime where intrinsic heating is significant, and perfect adiabaticity could therefore not be confirmed. The measured heating was, however, consistent with independently measured heating rates. This is promising for future investigations with a faster DC supply.

Adiabatic reduction of the trapping potential is very interesting in studies of ultra-cold chemistry where reactions are predicted to be dominated by quantum effects [28]. With adiabatic cooling, it is possible to study such reactions at temperatures below the Doppler limit without requiring more advanced cooling techniques. In addition, the combination of sideband cooling and adiabatic lowering makes it feasible to study chemistry with very low energy barriers; it is possible to reach kinetic energies corresponding to only a few μ K or below. This can further be extended with the possibility of tuning the final energy by adjusting the potential.

Another application is for Sympathetic Recoil Spectroscopy as mentioned in [Section 3.3](#). When the potential is lowered, the interaction between ions and light also changes, since it reduces the energy spacing between the levels - and thereby the required recoil kick for detection (a higher Lamb-Dicke factor). In the Lamb-Dicke limit, the scattering rate on the blue sideband is proportional to $\eta^2 = k^2\hbar/2m\omega$. This implies that recoil inducing scatter events will increase proportionally with $1/\omega$ and detection will require fewer scattered photons. This can be very relevant in spectroscopy of vibrational transitions in the infrared and for molecules where decay to other rovibrational levels are present.

Sympathetic Sideband Cooling of Molecular Ions

As mentioned in [Section 3.3](#), high precision studies of otherwise inaccessible molecular ions can be realized through Sympathetic Recoil Spectroscopy (SRS). The first step in realizing this is to cool a two ion crystal containing a molecular ion and a reference atom to the ground state: the topic of this chapter. This type of cooling scheme, termed sympathetic sideband cooling, has been demonstrated earlier in other experiments, for example by focusing light onto a single ion of a $^{40}\text{Ca}^+ / ^{40}\text{Ca}^+$ crystal with a resulting ground state occupation of 95% [96], and by atomic ions of different species, $^{24}\text{Mg}^+ / ^9\text{Be}^+$, with a resulting ground state occupation of 97% [97]. Finally, this has been an important ingredient in realizing a frequency reference based on $^{27}\text{Al}^+$ through quantum logic spectroscopy with a co-trapped $^9\text{Be}^+$ ion [20].

14.1 Sideband Spectrum of a Two Ion Crystal

When two ions are trapped together, two secular modes appear as described in [Section 2.3](#). In this case, each sideband gets a set of sub-sidebands which make the spectrum a bit more complex as seen in [Figure 14.1](#). With a well-known secular potential, it is however straightforward to map out the different sidebands, and the labels in [Figure 14.1](#) indicate the (n,m) 'th sideband of the in-phase/out-of-phase motions respectively.

The spectrum has been acquired with two $^{40}\text{Ca}^+$ ions in the trap, but the spectrum is very similar for co-trapped ions of different mass, with a minor shift in the sideband separations according to [Equation 2.24](#). For a typical in phase mode oscillation frequency of 300 kHz, the oscillation frequency shifts around 2 kHz for a change of one atomic mass unit (amu). This is on the edge of the current resolution (limited by the linewidth of the laser) but as

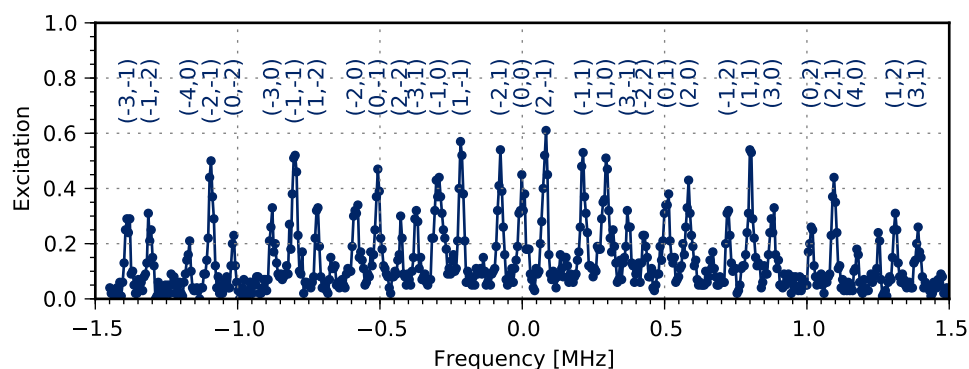


Figure 14.1: Sideband spectrum with two $^{40}\text{Ca}^+$ ions located along the axis of the trap. The sidebands are marked with sideband orders of the two secular modes as (in-phase, out-of-phase).

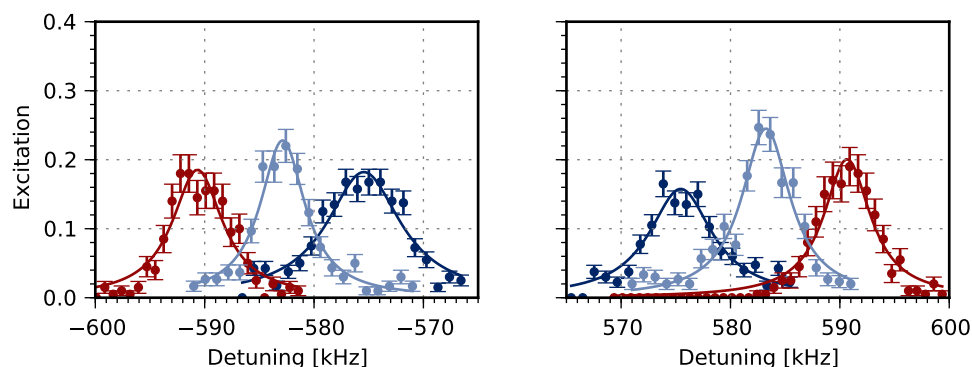


Figure 14.2: Second red and blue sidebands for the in-phase mode of a two ion crystal with different species. \bullet $^{44}\text{Ca} + ^{40}\text{Ca}$; \bullet $^{40}\text{Ca} + ^{40}\text{Ca}$; \bullet $^{42}\text{Ca} + ^{40}\text{Ca}$;

illustrated in Figure 14.2, it is possible to distinguish the different isotopes of calcium.

14.2 Formation/Identification of Molecular Ions

Molecular ions are formed by introducing H_2 or D_2 into the chamber from which CaH^+ and CaD^+ can be formed selectively. The mass of the reaction product can be confirmed with sideband spectroscopy at single amu accuracy as seen in Figure 14.3.

The spectrum clearly illustrates the sideband of $^{40}\text{CaH}^+$ falling between $^{40}\text{Ca}^+$ and $^{42}\text{Ca}^+$ and the latter overlapping with that of $^{40}\text{CaD}^+$ as expected. With this measurement, it is possible to verify the mass of the reaction product. Additionally, the dark ion can later be confirmed as a molecular com-

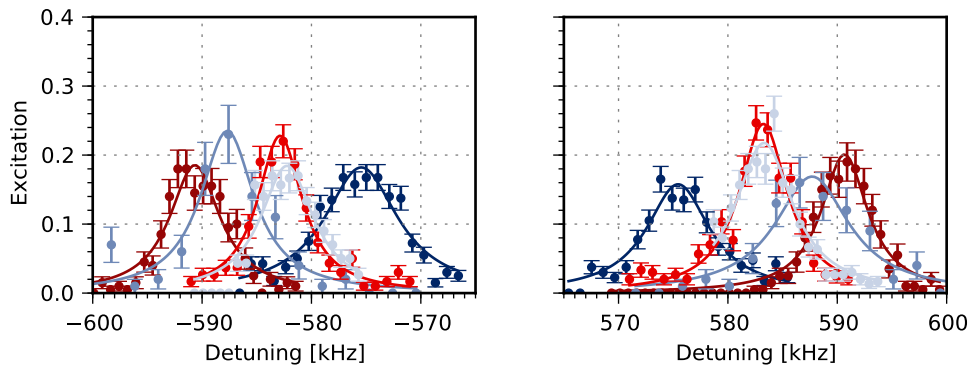


Figure 14.3: Second red and blue sidebands for the in-phase mode of a two ion crystal with different species of calcium and molecular products. • $^{44}\text{Ca} + ^{40}\text{Ca}$; • $^{40}\text{Ca} + ^{40}\text{Ca}$; • $^{40}\text{CaH} + ^{40}\text{Ca}$; • $^{42}\text{Ca} + ^{40}\text{Ca}$; • $^{40}\text{CaD} + ^{40}\text{Ca}$

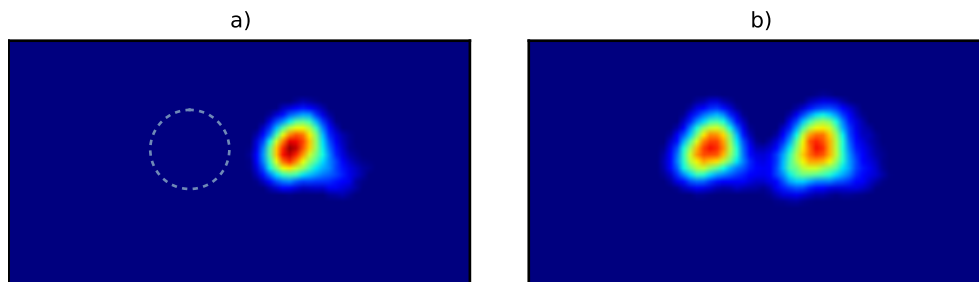


Figure 14.4: Photo dissociation of ^{40}CaH with exposure to UV light. a) before exposure $^{40}\text{CaH} + ^{40}\text{Ca}$ b) after exposure $^{40}\text{Ca} + ^{40}\text{Ca}$.

pound by subsequent photo-assisted dissociation. This is illustrated in Figure 14.4 showing the ions before and after approximately 1 s exposure to 272 nm light. With a bright ion appearing after exposure to ultraviolet light, the dark ion is confirmed to be a compound containing $^{40}\text{Ca}^+$. This technique is used after each experiment to ensure that the experiments indeed have been carried out with molecular ions.

14.3 Sideband Cooling

With two ions in the trap, both motional modes can in principle be cooled in the same way as for a single ion. If ground state cooling is used to enable the motion as a quantum bus, it will however suffice to cool only one of the modes. In this case the laser is tuned to one of the motional modes and

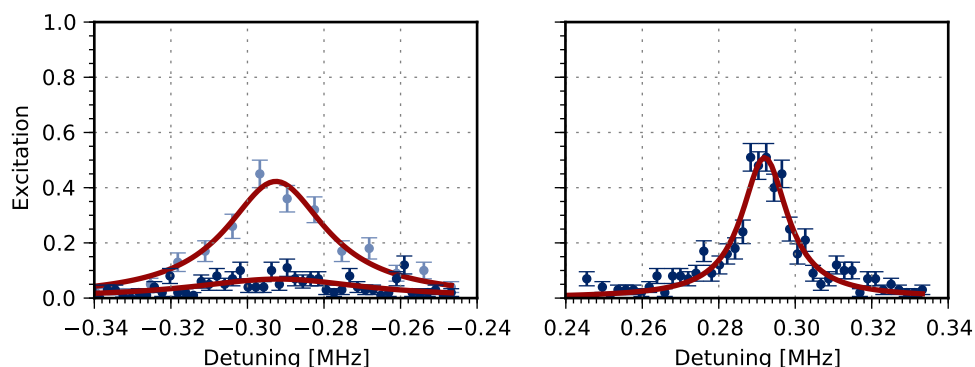


Figure 14.5: First red and blue sideband of $^{40}\text{CaH} + ^{40}\text{Ca}$ in-phase mode: \bullet before; and \bullet after sideband cooling, $P_0 = 0.86 \pm 0.01$.

sideband cooling proceeds just as in the single ion case.

The result of sympathetic sideband cooling of a single $^{40}\text{CaH}^+$ -ion together with a $^{40}\text{Ca}^+$ -ion is shown in Figure 14.5. A clear reduction in the strength of the red sideband is observed corresponding to a ground state population of $P_0 = 0.86 \pm 0.01$. Compared with the ground state population after Doppler cooling of $P_0 \approx 0.03$, this indicates a significant population transfer.

Later analysis has shown (see Appendix C for a description), that the final ground state population most likely was limited by a node in the excitation probability as illustrated in Figure 14.6. Due to a combination of low coupling on the second sideband and a node in the excitation probability of the first sideband, a significant population is trapped in states above $n = 100$. The simulations show that a change in the pulse lengths should enable close to unity ground state population. Alternatively, it is possible to use a continuous cooling scheme which does not suffer from this problem. In this case, it is however necessary to compensate for possible Stark shifts induced by the repumping laser. Theoretical studies have also indicated overall better performance with continuous cooling schemes [98].

14.4 Conclusion

With the experiments described in this chapter, we have demonstrated sympathetic sideband cooling of a molecular ion together with an interacting atomic ion. The final ground state occupation of $P_0 = 0.86 \pm 0.01$ was slightly below similar experiments with atomic ions [96, 97], though also realized at significantly lower secular frequency. Simulation results further show that a modified cooling sequence could lead to significant improvements in

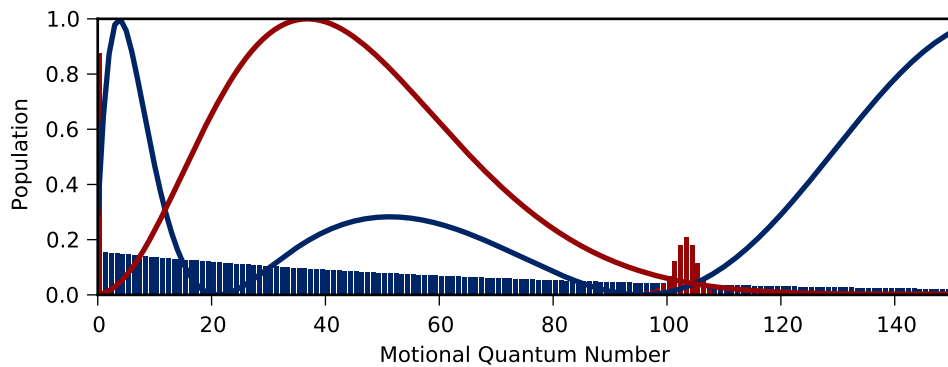


Figure 14.6: Simulated motional distribution before and after sideband cooling. Populations have been scaled $\times 10$ except for the ground state population after cooling. The solid lines indicate the expected population in $D_{5/2}$ after each pulse: \color{blue} first red sideband and \color{red} second red sideband. Population above $n = 100$ is trapped due to low coupling strength on both the first and second red sideband with a resulting ground state population of $P_0 = 0.87$.

the ground state population. Spectroscopy using sympathetic recoil would greatly benefit from this, but such measurements should also be possible with the current ground state population, though at lower signal-to-noise ratio.

In this demonstration, molecular ions are formed from Doppler cooled atomic ions, but it should be straightforward to extend the scheme to other types of molecules with similar masses. This makes Sympathetic Recoil Spectroscopy a very universal tool, as the same system can be used to study a multitude of different molecular and atomic ions.

CHAPTER 15

Summary and Outlook

This thesis has described our work on realizing experiments with molecular ions cooled to the motional ground state. The major part of this work has been to construct a system to generate optical pulses and to stabilize a laser for addressing the narrow $S_{1/2} \leftrightarrow D_{5/2}$ transition in $^{40}\text{Ca}^+$. The linewidth of the laser has been estimated to 55 Hz from the in-loop error signal. With the current equipment, it is not possible to measure the linewidth directly, it is only possible to set an upper bound by probing the $S_{1/2} \leftrightarrow D_{5/2}$ transition, for example using Ramsey spectroscopy. Technical difficulties resulted in a larger linewidth, but these will be resolved shortly and followed by such a measurement.

With this system, we have demonstrated sideband cooling of a single $^{40}\text{Ca}^+$ ion at motional frequency of 585 kHz to a ground state occupation of more than 99%. Cooling has, so far, only been realized in a single dimension, but the low heating rate indicates it should be straightforward to extend the cooling to all 3 dimensions using techniques that have been demonstrated in other groups [99, 100, 101]. This would provide the possibility to study reaction chemistry at temperatures of only a few μK . This naturally requires compensation of micromotion to the same level, but preliminary studies indicate that it should be feasible to reach kinetic energies below 1 μK , and compensation at this level has already been demonstrated in other traps [102].

The experiments were realized in a macroscopic trap with a diagonal electrode spacing of 7 mm. This provides a very open geometry, thus making the trap easier to combine with external equipment, for example to generate molecules or highly charged ions. The macroscopic size also results in reduced sensitivity to electric field noise from fluctuating patch potentials, resulting in a heating rate of only one quantum per second. Unlike other studies [79, 81], we observe a heating rate which is independent of the secular oscillation frequency. This indicates a dominant noise source with a different

frequency spectrum than typically observed. We plan to investigate this heating process further in the near future to reveal the source of this noise. With an improved DC supply for adiabatic lowering of the secular potential, we also expect to be able to investigate the heating process at even lower secular frequencies.

Through lowering of the axial potential, we have demonstrated adiabatic cooling of a single ion below the Doppler limit. The final temperature was reduced to one fourth of the initial temperature. The spectroscopic resolution of the 729 nm laser limited the minimum potential at which a reliable temperature measurement could be realized, but with a narrower linewidth it should be possible to investigate significantly lower potentials. Lowering of the axial potential was also utilized to reduce the zero-point motion of a single sideband cooled ion to a kinetic energy corresponding to only 6.8 μK . Due to a limited bandwidth in the DC supply, the measurements were limited to a regime where motional heating was significant, and perfect adiabaticity could therefore not be confirmed. In the near future, we plan to construct a new supply capable of controlling the potentials on a time scale where motional heating is negligible.

Finally, we have demonstrated sympathetic sideband cooling of a single molecular ion together with an auxiliary ion - the first step towards sympathetic recoil spectroscopy of molecular ions. We achieved a final ground state occupation of 86%, less than that realized with a single ion, but we expect a significant improvement in future experiments with an optimized cooling scheme. Other experiments have demonstrated close to unity ground state population with atomic ions of similar masses [96, 103] and even for ions with a mass ratio around 3 [20, 97]. This further supports the expectations of improved cooling with a revised cooling scheme.

With the demonstration of sympathetic sideband cooling of molecular ions, spectroscopic investigations of molecules are within reach. Looking ahead, it would be very interesting to realize spectroscopy between different rovibrational levels. For this, the molecule must be prepared in a well defined rovibrational state. Rotational cooling has already been demonstrated using optical pumping [104, 105], but with the ability to address different rotational states, it should also be possible to realize cooling by coupling the rotation to the translational motion of the ion [29, 106, 107], or alternatively by a probabilistic scheme [108]. Combined with optical frequency combs [109], this technique have potential to study a multitude of different molecular ions.

Part IV

Appendix

APPENDIX A

Ion motion in presence of stray electric fields

The motion of a trapped ion is affected by the presence of stray electric fields. With a stray electric field, the equation of motion is given by:

$$\frac{d^2 r_i}{d\xi^2} + (a_i - 2q_i \cos(2\xi))r_i + \frac{4qE_i}{m\Omega^2} = 0, \quad i = x, y, z \quad (\text{A.1})$$

where E_i is the electric field in the i 'th direction, q is the charge of the particle¹.

In the pseudopotential model it is assumed that the amplitude of the motion of the ion can be separated into two components (as described in section 2.1.1) given by (following [37])

$$r_i = R_i + \delta_i \quad (\text{A.2})$$

With the assumptions that $\delta_i \ll R_i$ and $\frac{d\delta_i}{dt} \gg \frac{dR_i}{dt}$ the equation of motion (A.1) can be written as

$$\frac{d^2 \delta_i}{d\xi^2} + (a_i - 2q_i \cos(2\xi))R_i + \frac{4qE_i}{m\Omega^2} = 0, \quad (\text{A.3})$$

If we further assume that $a_i \ll q_i$ and $E_i \ll \alpha U_{\text{rf}} R_i$ (A.3) can be integrated to:

$$\delta_i = -\frac{q_i R_i}{2} \cos(2\xi) \quad (\text{A.4})$$

and (A.2) can be written as:

$$r_i = R_i - \frac{q_i R_i}{2} \cos(2\xi) \quad (\text{A.5})$$

¹ Be aware not to confuse the charge of the particle q with the dimensionless parameters q_i

Substituting this into equation (A.1) yields:

$$\frac{d^2 r_i}{d\xi^2} + (a_i - 2q_i \cos(2\xi)) \left(R_i - \frac{q_i R_i}{2} \cos(2\xi) \right) + \frac{4qE_i}{m\Omega^2} = 0 \quad (\text{A.6})$$

From (A.3) it is seen that the acceleration due to the RF-drive over an oscillation period averages to zero, and the acceleration of the secular motion over the same period can hence be written as

$$\left\langle \frac{d^2 R_i}{d\xi^2} \right\rangle = \frac{1}{\pi} \int_0^\pi \frac{d^2 r_i}{d\xi^2} d\xi \quad (\text{A.7})$$

which can be integrated to

$$\frac{d^2 R_i}{d\xi^2} = - \left(a_i + \frac{q_i^2}{2} \right) R_i + \frac{4qE_i}{m\Omega^2} \quad (\text{A.8})$$

Expressing this in terms of t gives:

$$\frac{d^2 R_i}{dt^2} = - \left(a_i + \frac{q_i^2}{2} \right) \frac{\Omega^2}{4} R_i + \frac{4qE_i}{m\Omega^2} = \omega_i^2 R_i + \frac{4qE_i}{m\Omega^2} \quad (\text{A.9})$$

The general solution to this differential equation is:

$$R_i = r_i^0 \cos(\omega_i t + \phi_i) + \frac{4qE_i}{m\Omega^2 \omega_i^2} \quad (\text{A.10})$$

where r_i^0 and ϕ_i depends on the initial conditions. With the substitution $r_i^e = \frac{4qE_i}{m\Omega^2 \omega_i^2}$ (A.5) can be written as

$$r_i = \left(r_i^e + r_i^0 \cos(\omega_i t + \phi_i) \right) \left(1 - \frac{q_i}{2} \cos(2\xi) \right) \quad (\text{A.11})$$

APPENDIX B

The $^{40}\text{Ca}^+$ ion

B.1 Dipole Transitions

Transition	Wavelength [nm]	$\Gamma/2\pi$ [MHz]	Sat. intensity [mW/cm ²]
$^2\text{S}_{1/2}-^2\text{P}_{1/2}$	396.847	20.7	43.3
$^2\text{S}_{1/2}-^2\text{P}_{3/2}$	393.366	21.5	46.2
$^2\text{D}_{3/2}-^2\text{P}_{1/2}$	866.214	1.69	0.34
$^2\text{D}_{3/2}-^2\text{P}_{3/2}$	849.802	0.177	0.038
$^2\text{D}_{5/2}-^2\text{P}_{3/2}$	854.209	1.58	0.33

Table B.1: Data for dipole-allowed transitions in $^{40}\text{Ca}^+$. Transition wavelengths are measured in air [55, 110]. $\Gamma/2\pi$ is the transition rate [55, 110]. Saturation intensities are calculated according to $I_{\text{sat}} = \frac{\hbar\Gamma\omega^3}{12\pi c^3}$ [111], using the relevant transition rate and transition frequency for Γ and ω_a , respectively.

	$^2\text{S}_{1/2}(-1/2)$	$^2\text{S}_{1/2}(+1/2)$
$^2\text{P}_{1/2}(-1/2)$	$-\sqrt{1/3}$	$\sqrt{2/3}$
$^2\text{P}_{1/2}(+1/2)$	$-\sqrt{2/3}$	$\sqrt{1/3}$
$^2\text{P}_{3/2}(-3/2)$	1	-
$^2\text{P}_{3/2}(-1/2)$	$\sqrt{2/3}$	$\sqrt{1/3}$
$^2\text{P}_{3/2}(+1/2)$	$\sqrt{1/3}$	$\sqrt{2/3}$
$^2\text{P}_{3/2}(+3/2)$	-	1

Table B.2: Clebsch-Gordan coefficients for transitions between the $^2\text{S}_{1/2}$ state and the $^2\text{P}_{1/2}$ and $^2\text{P}_{3/2}$ states.

	$3D_{3/2, -3/2}$	$3D_{3/2, -1/2}$	$3D_{3/2, +1/2}$	$3D_{3/2, +3/2}$
$4P_{1/2, -1/2}$	$\sqrt{1/2}$	$-\sqrt{1/3}$	$\sqrt{1/6}$	-
$4P_{1/2, +1/2}$	-	$\sqrt{1/6}$	$-\sqrt{1/3}$	$\sqrt{1/2}$
$4P_{3/2, -3/2}$	$-\sqrt{3/5}$	$\sqrt{2/5}$	-	-
$4P_{3/2, -1/2}$	$-\sqrt{2/5}$	$-\sqrt{1/15}$	$\sqrt{8/15}$	-
$4P_{3/2, +1/2}$	-	$-\sqrt{8/15}$	$\sqrt{1/15}$	$\sqrt{2/5}$
$4P_{3/2, +3/2}$	-	-	$-\sqrt{2/5}$	$\sqrt{3/5}$

Table B.3: Clebsch-Gordan coefficients for transitions between the $3D_{3/2}$ state and the $4P_{1/2}$ and $4P_{3/2}$ states.

	$4P_{3/2, -3/2}$	$4P_{3/2, -1/2}$	$4P_{3/2, +1/2}$	$4P_{3/2, +3/2}$
$3D_{5/2, -5/2}$	$\sqrt{2/3}$	-	-	-
$3D_{5/2, -3/2}$	$-\sqrt{4/15}$	$\sqrt{2/5}$	-	-
$3D_{5/2, -1/2}$	$\sqrt{1/15}$	$-\sqrt{2/5}$	$\sqrt{1/5}$	-
$3D_{5/2, +1/2}$	-	$\sqrt{1/5}$	$-\sqrt{2/5}$	$\sqrt{1/15}$
$3D_{5/2, +3/2}$	-	-	$\sqrt{2/5}$	$-\sqrt{4/15}$
$3D_{5/2, +5/2}$	-	-	-	$\sqrt{2/3}$

Table B.4: Clebsch-Gordan coefficients for transitions between the $3D_{5/2}$ state and the $4P_{3/2}$ state.

B.2 Zeeman-splitting

The Zeeman-splitting of the magnetic sublevels of $^{40}\text{Ca}^+$ is given by:

$$\Delta E_{Zeeman} = m_J g_J \mu_B B, \quad (\text{B.1})$$

where m_J is the magnetic quantum number, μ_B is the Bohr magneton, B is the magnetic field strength and g_J is the Land g -factor,

$$g_J = 1 + \frac{J(J+1) + S(S+1) - L(L+1)}{2J(J+1)}. \quad (\text{B.2})$$

Values of g_J are listed in Table B.5 for the lowest lying states of the $^{40}\text{Ca}^+$ ion.

State	g_J
$^2\text{S}_{1/2}$	2
$^2\text{P}_{1/2}$	2/3
$^2\text{P}_{3/2}$	4/3
$^2\text{D}_{3/2}$	4/5
$^2\text{D}_{5/2}$	6/5

Table B.5: Values of g_J for the lowest lying levels of the $^{40}\text{Ca}^+$ ion.

For $B = 0.1 \text{ mT}$, the Zeeman-splitting of the ground-state sublevels is $2\pi \times 2.8 \text{ MHz}$.

B.3 The $S_{1/2} \leftrightarrow D_{5/2}$ Transition

The $S_{1/2} \leftrightarrow D_{5/2}$ transition at 729 nm is an electric quadrupole transition and allow transitions with $\Delta m_J = 0, \pm 1, \pm 2$. The coupling strength on these transitions depend on the geometry between the light and magnetic field which we describe by the parameters ϕ and γ , where ϕ is the angle between the magnetic field vector and the wave vector of the light. The second parameter, γ , describes the geometry with respect to the polarization and is the angle between the polarization vector and the magnetic field vector projected into the plane normal to the wave vector (this can also be thought of as the angle between \vec{B} and the plane spanned by \vec{k} and \vec{E}). In this basis, the relative coupling strength on the different Δm_J transitions is given by [102]:

$$\begin{aligned} g^{(0)} &= \frac{1}{2} \left| \cos(\gamma) \sin(2\phi) \right| \\ g^{(\pm 1)} &= \frac{1}{\sqrt{6}} \left| \cos(\gamma) \cos(2\phi) + i \sin(\gamma) \cos(\phi) \right| \\ g^{(\pm 2)} &= \frac{1}{\sqrt{6}} \left| \frac{1}{2} \cos(\gamma) \sin(2\phi) + i \sin(\gamma) \sin(\phi) \right| \end{aligned} \quad (\text{B.3})$$

These factors are illustrated in Figure B.1. For the geometry described in Part III, we have $\phi = 90^\circ$ and γ in the range from 0° to 90° .

The coupling strength between the individual magnetic sub-levels further depend on the Clebsch-Gordan coefficients. The maximum relative strength between these levels are illustrated in Figure B.2. For the geometry described

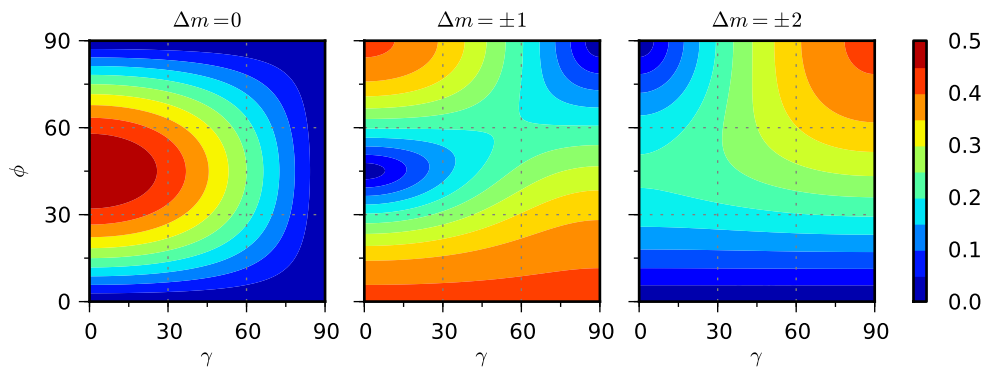


Figure B.1: Relative coupling strength on the $S_{1/2} \leftrightarrow D_{5/2}$ transition in different geometries. ϕ is the angle between \vec{B} and \vec{k} and γ the angle between \vec{B} and \vec{E} measured in the plane normal to \vec{k} (the plane spanned by electric and magnetic field vectors of the light).

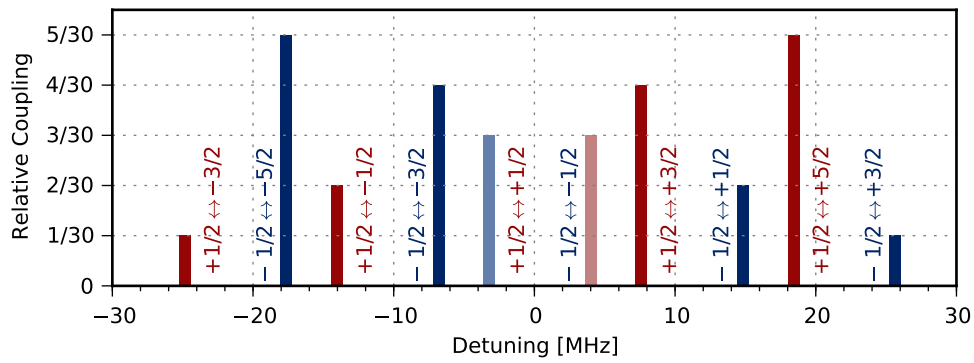


Figure B.2: Magnetic components of the $S_{1/2} \leftrightarrow D_{5/2}$ transition in a magnetic field of 0.66 mT. The maximum relative strengths are indicated according to the squared Clebsch-Gordan coefficients [102].

in [Part III](#), the two transitions in the center disappear as $\Delta m_j = 0$ transitions do not couple with $\phi = 90^\circ$.

Sideband Cooling Simulation

The sideband cooling simulations presented in [Chapter 14](#) are based on a simple statistical model. Starting with an initial thermal distribution after Doppler cooling, the expected population transfer on the red sideband is calculated and used to deduce a new motional distribution after each cooling cycle.

The excitation probability to the $D_{5/2}$ state is calculated for each individual motional state according to [Equation 3.6](#):

$$\rho_{ee}(n) = \sin^2\left(\frac{\Omega_{n,n+s}t}{2}\right), \quad (\text{C.1})$$

where $s = -2, -1$ for cooling on the second and first red sideband respectively. The actual Rabi frequencies, $\Omega_{n,n+s}$, are calculated with [Equation 3.17](#) from the experimentally measured Rabi frequency in the ground state. Starting with an initial thermal state, the new motional distribution is calculated after one cooling pulse (recall that s is a negative number):

$$p_n = p_n(1 - \rho_{ee}(n) + \rho_{ee}(n - s)) \quad (\text{C.2})$$

This process is repeated for each cooling cycle on the second red sideband and, subsequently, on the first red sideband. The resulting distribution, p_n , is plotted in [Figure 14.6](#). The solid curves in the same figure corresponds to $\rho_{ee}(n)$ for the first and second sidebands.

This simulation neglects all effects from off-resonant scattering and decays on the motional sidebands. Especially at high excitations, decay on the motional sidebands happens with a significant probability. The probability of decay is, however, nearly identical on the red and blue sidebands and should therefore not affect the dynamics significantly.

This model has also been applied for the single ion case with a resulting unity ground state occupation; in good agreement with the result in [Chapter 12](#).

APPENDIX D

Control System

A large part of realizing the sideband cooling experiments has been to develop a system to control the different parts of the experiment. This has involved construction of a hardware system to generate the actual pulses as well as development of software to control it. This appendix contains a brief description of the hardware and the corresponding software implementation.¹

D.1 Software System

The entire experiment is controlled from a computer with a software framework written in Python [112]. The software system is created as a modular framework to simplify future development. Communication between the different modules can be realized through TCP/IP which makes it possible to move parts of the system to separate hardware and/or other programming languages. An overview of the software system is illustrated in Figure D.1.

The first block, the *Graphical User Interface (GUI)*, provides control of the entire system and configuration of the different parameters. This user interface is based on a Python implementation of Qt4 [113]. The user interface is used to define all parameters for the specific experiments which are then passed to the other modules through a dictionary.

The *GUI* communicates with the *ExperimentController (ExpCtrl)* which handles the overall control of all running experiments. The *ExpCtrl* calls an instance of *ExperimentIterator (ExpItr)* for each experiment. *ExpCtrl* is capable of handling multiple active experiments which makes it possible to pause an ongoing experiment to interleave another, for example for testing possible frequency drifts etc.

¹ This description is rather brief; the author will hopefully soon have time to provide a more comprehensive documentation.

Expltr handles the actual iterations over each data point in an experiment. This includes iterations over typically 100 repetitions of the same sequence for averaging and iteration over each data point with different parameters (for example a frequency scan). *Expltr* handles control of the pulse-hardware and the CCD camera as well as processing of images. For each iteration, *Expltr* instructs *ExpCtrl* to transmit new data to update the *GUI*. Each instance of *Expltr* is configured with a specific script from a library of different experiments, for example quantum jump spectroscopy or Rabi flopping.

The Experiment Library contains the specific code for the different experiments, which are based on a set of standard sequence components from the class *SequenceComponents* (*SeqCom*). *SeqCom* contains the basic building blocks for an experiment, for example Doppler cooling, sideband cooling, readout etc. (basically corresponding to Figure 11.4). Figure D.2 shows a code example for a quantum jump spectroscopy experiment. *SeqCom* is reused in all experiments, which makes it simple to quickly realize new experimental sequences.

D.2 Hardware System

The actual hardware used to control the experiment is based on an open source Field Programmable Gate Array (FPGA) system [114, 115]. The FPGA runs at 100 MHz providing sub-micro-second control of 32 digital TTL outputs. These outputs are used to control shutters, camera exposure etc. An additional 32 digital channels are used to control a set of Direct Digital Synthesizers (DDS's) capable of synthesizing RF signals in the range between 10 MHz and 350 MHz [116]. These synthesizer boards are also equipped with individual FPGAs which make it possible to realize phase coherent switching between different frequencies as well as phase continuous switching and frequency/amplitude sweeps.

The sequences are generated by *Expltr* which interfaces with an open source API [117] for compiling the sequence to byte-code and transmitting it to the FPGA.

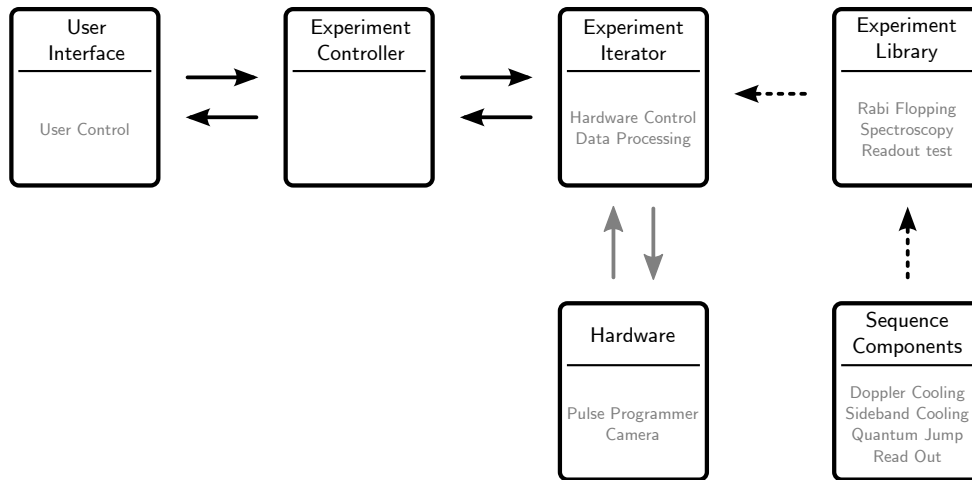


Figure D.1: Overview of the software framework. Normal arrows indicate two-way communication, the dashed arrows indicate pure imports/inheritance and the gray arrows represent actual electrical signals.

```

""" Doppler Cooling """
seq.doppler_cooling()

""" Qubit Initialisation """
if self.conf['qjsp.qunit']:# Check if qubit initialization is enabled
    seq.qubit_initialisation()

""" Sideband Cooling """
if self.conf['qjsp.sbc']:# Check if sideband cooling is enabled
    seq.sideband_cooling()

""" Quantum Jump """
seq.qu_jump() # One pi-pulse on transition

""" Read Out """
seq.read_out()

""" Ion Recycling """
seq.recycle()
  
```

Figure D.2: Example code for a quantum jump spectroscopy experiment. `seq` is an instance of `SequenceComponents`.

Bibliography

- [1] W. Paul. *Ein neues massenspektrometer ohne magnetfeld*. Zeitschrift für naturforschung, **A8**, 448 – 450 (1953).
- [2] H. A. Schuessler, E. N. Fortson, and H. G. Dehmelt. *Hyperfine structure of the ground state of $^3\text{He}^+$ by the ion-storage exchange-collision technique*. Phys. Rev., **187**, 5–38 (1969).
- [3] T. W. Hänsch and A. L. Schawlow. *Cooling of gases with laser radiation*. Opt. Commun., **13**, 68 (1975).
- [4] D. J. Wineland and H. Dehmelt. *Proposed $10^{14} \delta\nu < \nu$ laser fluorescence spectroscopy on Tl^+ mono-ion oscillator III*. Bull. Am. Phys. Soc., **20**, 637 (1975).
- [5] W. Neuhauser, M. Hohenstatt, P. E. Toschek, et al. *Visual observation and optical cooling of electrostatically contained ions*. Appl. Phys. A, **17**, 123–129 (1978).
- [6] S. A. Diddams, T. Udem, J. C. Bergquist, et al. *An optical clock based on a single trapped $^{199}\text{Hg}^+$ ion*. Science, **293**, 825–828 (2001).
- [7] J. L. Hall. *Nobel lecture: Defining and measuring optical frequencies*. Rev. Mod. Phys., **78**, 1279–1295 (2006).
- [8] T. W. Hänsch. *Nobel lecture: Passion for precision*. Rev. Mod. Phys., **78**, 1297–1309 (2006).
- [9] W. H. Oskay, S. A. Diddams, E. A. Donley, et al. *Single-atom optical clock with high accuracy*. Phys. Rev. Lett., **97**, 020801 (2006).
- [10] E. S. Shuman, J. F. Barry, and D. DeMille. *Laser cooling of a diatomic molecule*. Nature, **467**, 820–823 (2010).
- [11] J. H. V. Nguyen, C. R. Viteri, E. G. Hohenstein, et al. *Challenges of laser-cooling molecular ions*. New Journal of Physics, **13**, 063023 (2011).

- [12] T. Baba and I. Waki. *Cooling and mass-analysis of molecules using laser-cooled atoms*. Jpn. J. Appl. Phys, **35**, L1134–L1137 (1996).
- [13] K. Mølhave and M. Drewsen. *Formation of translationally cold MgH^+ and MgD^+ molecules in an ion trap*. Phys. Rev. A, **62**, 011401 (2000).
- [14] J. C. J. Koelemeij, B. Roth, A. Wicht, et al. *Vibrational spectroscopy of HD^+ with 2-ppb accuracy*. Phys. Rev. Lett., **98**, 173002 (2007).
- [15] J. I. Cirac and P. Zoller. *Quantum computations with cold trapped ions*. Phys. Rev. Lett., **74**, 4091–4094 (1995).
- [16] R. Feynman. *Simulating physics with computers*. International Journal of Theoretical Physics, **21**, 467–488 (1982).
- [17] D. Deutsch. *Quantum theory, the Church-Turing principle and the universal quantum computer*. Royal Society of London Proceedings Series A, **400**, 97–117 (1985).
- [18] A. Sørensen and K. Mølmer. *Quantum computation with ions in thermal motion*. Phys. Rev. Lett., **82**, 1971–1974 (1999).
- [19] P. O. Schmidt, T. Rosenband, C. Langer, et al. *Spectroscopy using quantum logic*. Science, **309**, 749–752 (2005).
- [20] T. Rosenband, P. O. Schmidt, D. B. Hume, et al. *Observation of the $^1S_0 \rightarrow ^3P_0$ clock transition in $^{27}\text{Al}^+$* . Phys. Rev. Lett., **98**, 220801 (2007).
- [21] T. Rosenband, D. B. Hume, P. O. Schmidt, et al. *Frequency Ratio of Al^+ and Hg^+ Single-Ion Optical Clocks; Metrology at the 17th Decimal Place*. Science, **319**, 1808–1812 (2008).
- [22] C. W. Chou, D. B. Hume, J. C. J. Koelemeij, et al. *Frequency comparison of two high-accuracy Al^+ optical clocks*. Phys. Rev. Lett., **104**, 070802 (2010).
- [23] S. Canuto, M. A. Castro, and K. Sinha. *Theoretical determination of the spectroscopic constants of CaH^+* . Phys. Rev. A, **48**, 2461–2463 (1993).
- [24] A. Boutalib, J. Daudey, and M. El Mouhtadi. *Theoretical study of the lowest electronic states of CaH and CaH^+ molecules*. Chemical Physics, **167**, 111–120 (1992). ISSN 0301-0104.
- [25] S. Schiller and V. Korobov. *Tests of time independence of the electron and nuclear masses with ultracold molecules*. Phys. Rev. A, **71**, 032505 (2005).
- [26] J. J. Hudson, B. E. Sauer, M. R. Tarbutt, et al. *Measurement of the electron electric dipole moment using YbF molecules*. Phys. Rev. Lett., **89**, 023003 (2002).

- [27] E. R. Hudson, H. J. Lewandowski, B. C. Sawyer, et al. *Cold molecule spectroscopy for constraining the evolution of the fine structure constant*. Phys. Rev. Lett., **96**, 143004 (2006).
- [28] S. Willitsch, M. T. Bell, A. D. Gingell, et al. *Chemical applications of laser- and sympathetically-cooled ions in ion traps*. Phys. Chem. Chem. Phys., **10**, 7200–7210 (2008).
- [29] P. O. Schmidt, T. Rosenband, J. C. J. Koelemeij, et al. *Spectroscopy of atomic and molecular ions using quantum logic*. AIP Conference Proceedings, **862**, 305–312 (2006).
- [30] M. T. Bell, A. D. Gingell, J. M. Oldham, et al. *Ion-molecule chemistry at very low temperatures: cold chemical reactions between coulomb-crystallized ions and velocity-selected neutral molecules*. Faraday Discuss., **142**, 73–91 (2009).
- [31] D. DeMille. *Quantum computation with trapped polar molecules*. Phys. Rev. Lett., **88**, 067901 (2002).
- [32] D. Griffiths. *Introduction to Electrodynamics*. Prentice Hall, New Jersey (1989).
- [33] R. Thompson, T. Harmon, and M. Ball. *The rotating-saddle trap: a mechanical analogy to rf-electric-quadrupole ion trapping?* Can. J. Phys., **80**, 1433 – 1448 (2002).
- [34] W. Paul. *Electromagnetic traps for charged and neutral particles*. Rev. Mod. Phys., **62**, 531 – 540 (1990).
- [35] M. G. Raizen, J. M. Gilligan, J. C. Bergquist, et al. *Ionic crystals in a linear paul trap*. Phys. Rev. A, **45**, 6493–6501 (1992).
- [36] N. McLachlan. *Theory and Application of Mathieu Functions*. Dover Publication, Inc., New York (1964).
- [37] P. K. Ghosh. *Ion Traps*. Clarendon Press, Oxford (1995).
- [38] D. Leibfried, R. Blatt, C. Monroe, et al. *Quantum dynamics of single trapped ions*. Rev. Mod. Phys., **75**, 281–324 (2003).
- [39] D. J. Berkeland, J. D. Miller, J. C. Bergquist, et al. *Minimization of ion micromotion in a Paul trap*. J. Appl. Phys., **83**, 5025–5033 (1998).
- [40] Q. A. Turchette, C. S. Wood, B. E. King, et al. *Deterministic entanglement of two trapped ions*. Phys. Rev. Lett., **81**, 3631–3634 (1998).

- [41] P. F. Herskind, A. Dantan, M. Albert, et al. *Positioning of the rf potential minimum line of a linear paul trap with micrometer precision*. J. Phys. B, **42**, 154008+ (2009).
- [42] J. J. Sakurai. *Modern Quantum Mechanics*. Addison-Wesley, Redwood City (1985).
- [43] G. Morigi and H. Walther. *Two-species coulomb chains for quantum information*. Euro. Phys. J. D, **13**, 261–269 (2001).
- [44] L. Allen. *Optical Resonance and Two-Level Atoms*. Wiley, New York (1975).
- [45] P. W. Milonni and J. H. Eberly. *Lasers*. Wiley, New York (1988).
- [46] C. J. Foot. *Atomic Physics*. Oxford University Press, New York (2005).
- [47] S. Stenholm. *The semiclassical theory of laser cooling*. Rev. Mod. Phys., **58**, 699–739 (1986).
- [48] C. R. Clark, J. E. Goeders, Y. K. Dodia, et al. *Detection of single-ion spectra by Coulomb-crystal heating*. Phys. Rev. A, **81**, 043428 (2010).
- [49] F. G. Major, V. N. Gheorghe, and G. Werth. *Charged Particle Traps*. Springer, Berlin (2004).
- [50] H. J. Metcalf and P. van der Straten. *Laser Cooling and Trapping*. Springer, New York (1999).
- [51] W. M. Itano and D. J. Wineland. *Laser cooling of ions stored in harmonic and Penning traps*. Phys. Rev. A, **25**, 35–54 (1982).
- [52] I. Marzoli, J. I. Cirac, R. Blatt, et al. *Laser cooling of trapped three-level ions: Designing two-level systems for sideband cooling*. Phys. Rev. A, **49**, 2771–2779 (1994).
- [53] C. Roos, T. Zeiger, H. Rohde, et al. *Quantum state engineering on an optical transition and decoherence in a Paul trap*. Phys. Rev. Lett., **83**, 4713–4716 (1999).
- [54] F. Diedrich, J. C. Bergquist, W. M. Itano, et al. *Laser cooling to the zero-point energy of motion*. Phys. Rev. Lett., **62**, 403–406 (1989).
- [55] D. James. *Quantum dynamics of cold trapped ions with application to quantum computation*. Appl. Phys. B, **66**, 181–190 (1998).
- [56] D. Meschede. *Optics, Light and Lasers*. Wiley-VCH, Weinheim, Germany (2004).

- [57] G. Poulsen. *Frekvensstabilisering af diodelaser*. Bachelor's Thesis, Departments of Physics, Aarhus University (2006).
- [58] N. Nise. *Control Systems Engineering, 5th Edition*. John Wiley & Sons (2008).
- [59] R. E. Thomas and A. J. Rosa. *The Analysis and Design of Linear Circuits*. Wiley (2006).
- [60] G. Kirchmair. *Frequency stabilization of a Titanium-Sapphire laser for precision spectroscopy on Calcium ions*. Diploma Thesis, Universität Innsbruck, Austria (2006).
- [61] R. Cook. *Concepts and Applications of Finite Element Analysis*. Wiley, New York (2001).
- [62] T. Nazarova, F. Riehle, and U. Sterr. *Vibration-insensitive reference cavity for an ultra-narrow-linewidth laser*. *Appl. Phys. B*, **83**, 531–536 (2006).
- [63] A. E. Siegman. *Lasers*. University Science Books (1986).
- [64] E. A. Donley, T. P. Heavner, F. Levi, et al. *Double-pass acousto-optic modulator system*. *Rev. Sci. Instrum.*, **76**, 063112 (2005).
- [65] M. Houssin, M. Jardino, and M. Desaintfuscien. *Comparison of the calculated transient responses of a Fabry-Perot used in reflection and in transmission*. *Rev. Sci. Instrum.*, **61**, 3348–3352 (1990).
- [66] L.-S. Ma, P. Jungner, J. Ye, et al. *Delivering the same optical frequency at two places: accurate cancellation of phase noise introduced by an optical fiber or other time-varying path*. *Opt. Lett.*, **19**, 1777–1779 (1994).
- [67] E. D. Black. *An introduction to Pound-Drever-Hall laser frequency stabilization*. *Am. J. Phys.*, **69**, 79–87 (2001).
- [68] A. Schoof, J. Grünert, S. Ritter, et al. *Reducing the linewidth of a diode laser below 30 Hz by stabilization to a reference cavity with a finesse above 10^5* . *Opt. Lett.*, **26**, 1562–1564 (2001).
- [69] U. Sterr, T. Legero, T. Kessler, et al. *Ultrastable lasers: new developments and applications*. In *Society of Photo-Optical Instrumentation Engineers (SPIE) Conference Series*, volume 7431 of *Society of Photo-Optical Instrumentation Engineers (SPIE) Conference Series* (2009).
- [70] T. Nazarova, C. Lisdat, F. Riehle, et al. *Low-frequency-noise diode laser for atom interferometry*. *J. Opt. Soc. Am. B*, **25**, 1632–1638 (2008).

- [71] J. W. Papi and D. Golini. *Delayed elastic effects in the glass ceramics Zerodur and ULE at room temperature*. *Appl. Opt.*, **30**, 3087–3090 (1991).
- [72] P. Herskind, J. Lindballe, C. Clausen, et al. *Second-harmonic generation of light at 544 and 272 nm from an ytterbium-doped distributed-feedback fiber laser*. *Opt. Lett.*, **32**, 268–270 (2007).
- [73] A. Mortensen, J. J. T. Lindballe, I. S. Jensen, et al. *Isotope shifts of the $4s^2 1S_0 \leftrightarrow 4s5p^1P_1$ transition and hyperfine splitting of the $4s5p^1P_1$ state in calcium*. *Phys. Rev. A*, **69**, 042502+ (2004).
- [74] N. Kjærgaard, L. Hornekær, A. M. Thommesen, et al. *Isotope selective loading of an ion trap using resonance-enhanced two-photon ionization*. *Appl. Phys. B*, **71**, 207–210 (2000).
- [75] C. Wunderlich, T. Hannemann, T. Körber, et al. *Robust state preparation of a single trapped ion by adiabatic passage*. *J. Mod. Opt.*, **54**, 154–1549 (2007).
- [76] D. M. Meekhof, C. Monroe, B. E. King, et al. *Generation of nonclassical motional states of a trapped atom*. *Phys. Rev. Lett.*, **76**, 1796–1799 (1996).
- [77] C. Roos, T. Zeiger, H. Rohde, et al. *Quantum state engineering on an optical transition and decoherence in a Paul trap*. *Phys. Rev. Lett.*, **83**, 4713–4716 (1999).
- [78] N. Daniilidis, S. Narayanan, S. A. Möller, et al. *Fabrication and heating rate study of microscopic surface electrode ion traps*. *New J. Phys.*, **13**, 013032 (2011).
- [79] L. Deslauriers, S. Olmschenk, D. Stick, et al. *Scaling and suppression of anomalous heating in ion traps*. *Phys. Rev. Lett.*, **97**, 103007 (2006).
- [80] J. Labaziewicz, Y. Ge, P. Antohi, et al. *Suppression of heating rates in cryogenic surface-electrode ion traps*. *Phys. Rev. Lett.*, **100**, 013001 (2008).
- [81] J. J. McLoughlin, A. H. Nizamani, J. D. Siverns, et al. *Versatile ytterbium ion trap experiment for operation of scalable ion-trap chips with motional heating and transition-frequency measurements*. *Phys. Rev. A*, **83**, 013406 (2011).
- [82] S. Seidelin, J. Chiaverini, R. Reichle, et al. *Microfabricated surface-electrode ion trap for scalable quantum information processing*. *Phys. Rev. Lett.*, **96**, 253003 (2006).
- [83] D. Stick, W. K. Hensinger, S. Olmschenk, et al. *Ion trap in a semiconductor chip*. *Nat. Phys.*, **2**, 36–39 (2006). ISSN 1745-2473.

- [84] R. G. DeVoe and C. Kurtsiefer. *Experimental study of anomalous heating and trap instabilities in a microscopic ^{137}Ba ion trap*. Phys. Rev. A, **65**, 063407 (2002).
- [85] F. Diedrich, J. C. Bergquist, W. M. Itano, et al. *Laser cooling to the zero-point energy of motion*. Phys. Rev. Lett., **62**, 403–406 (1989).
- [86] C. Roos, T. Zeiger, H. Rohde, et al. *Quantum state engineering on an optical transition and decoherence in a Paul trap*. Phys. Rev. Lett., **83**, 4713–4716 (1999).
- [87] S. A. Schulz, U. Poschinger, F. Ziesel, et al. *Sideband cooling and coherent dynamics in a microchip multi-segmented ion trap*. New J. Phys., **10**, 045007 (2008).
- [88] C. Tamm, D. Engelke, and V. Bühner. *Spectroscopy of the electric-quadrupole transition $^2S_{1/2}(f = 0) \rightarrow ^2D_{3/2}(f = 2)$ in trapped $^{171}\text{Yb}^+$* . Phys. Rev. A, **61**, 053405 (2000).
- [89] J. J. McLoughlin, A. H. Nizamani, J. D. Siverns, et al. *Versatile ytterbium ion trap experiment for operation of scalable ion-trap chips with motional heating and transition-frequency measurements*. Phys. Rev. A, **83**, 013406 (2011).
- [90] Q. A. Turchette, Kielpinski, B. E. King, et al. *Heating of trapped ions from the quantum ground state*. Phys. Rev. A, **61**, 063418 (2000).
- [91] S. X. Wang, Y. Ge, J. Labaziewicz, et al. *Superconducting microfabricated ion traps*. Appl. Phys. Lett., **97**, 244102 (2010).
- [92] J. C. Bergquist, F. Diedrich, W. M. Itano, et al. *Hg^+ single ion spec.* In A. Demarchi, editor, *Proc. 4th Symposium on Frequency Standards and Metrology*, pages TN–27. Springer Verlag, Heidelberg (1988).
- [93] R. B. Blakestad, C. Ospelkaus, A. P. VanDevender, et al. *High-fidelity transport of trapped-ion qubits through an X-junction trap array*. Phys. Rev. Lett., **102**, 153002 (2009).
- [94] G. Huber, T. Deuschle, W. Schnitzler, et al. *Transport of ions in a segmented linear paul trap in printed-circuit-board technology*. New J. Phys., **10**, 013004 (2008).
- [95] W. K. Hensinger, S. Olmschenk, D. Stick, et al. *T-junction ion trap array for two-dimensional ion shuttling, storage, and manipulation*. Appl. Phys. Lett., **88**, 034101 (2006).

- [96] H. Rohde, S. T. Gulde, C. F. Roos, et al. *Sympathetic ground-state cooling and coherent manipulation with two-ion crystals*. J. Opt. B, **3**, S34 (2001).
- [97] M. D. Barrett, B. DeMarco, T. Schaetz, et al. *Sympathetic cooling of $^9\text{Be}^+$ and $^{24}\text{Mg}^+$ for quantum logic*. Phys. Rev. A, **68**, 042302 (2003).
- [98] D. Leibfried. Private Communication (November, 2011).
- [99] C. Monroe, D. M. Meekhof, B. E. King, et al. *Resolved-sideband raman cooling of a bound atom to the 3D zero-point energy*. Phys. Rev. Lett., **75**, 4011–4014 (1995).
- [100] B. E. King, C. S. Wood, C. J. Myatt, et al. *Cooling the collective motion of trapped ions to initialize a quantum register*. Phys. Rev. Lett., **81**, 1525–1528 (1998).
- [101] C. Roos, H. Nagerl, H. Rohde, et al. *Ground state cooling, quantum state engineering and study of decoherence of ions in paul traps*. J. Mod. Opt., **47**, 2573–2582 (2000).
- [102] C. F. Roos. *Controlling the quantum state of trapped ions*. Ph.D. thesis, Leopold-Franzens-Universität Innsbruck (2000).
- [103] J. P. Home, M. J. McDonnell, D. J. Szwer, et al. *Memory coherence of a sympathetically cooled trapped-ion qubit*. Phys. Rev. A, **79**, 050305 (2009).
- [104] P. F. Staannum, K. Hojbjerg, P. S. Skyt, et al. *Rotational laser cooling of vibrationally and translationally cold molecular ions*. Nat. Phys., **6**, 271–274 (2010).
- [105] T. Schneider, B. Roth, H. Duncker, et al. *All-optical preparation of molecular ions in the rovibrational ground state*. Nat. Phys., **6**, 275–278 (2010).
- [106] C. Lazarou, M. Keller, and B. M. Garraway. *Molecular heat pump for rotational states*. Phys. Rev. A, **81**, 013418 (2010).
- [107] I. S. Vogelius, L. B. Madsen, and M. Drewsen. *Rotational cooling of molecular ions through laser-induced coupling to the collective modes of a two-ion Coulomb crystal*. J. Phys. B, **39**, S1267–S1280 (2006).
- [108] I. S. Vogelius, L. B. Madsen, and M. Drewsen. *Probabilistic state preparation of a single molecular ion by projection measurement*. J. Phys. B, **39**, S1259–S1265 (2006).
- [109] D. Leibfried. *Quantum state preparation and control of single molecular ions*. arXiv:1109.0208 (2011).

-
- [110] NIST Atomic Spectra Database. <http://physics.nist.gov>.
- [111] B. H. Bransden and C. J. Joachain. *Physics of Atoms and Molecules*. Longman Scientific & Technical, England (1983).
- [112] <http://python.org/>.
- [113] <http://qt.nokia.com/>.
- [114] <http://pulse-programmer.org/>.
- [115] P. Pham. *A general-purpose pulse sequencer for quantum computing*. Master's thesis, Massachusetts Institute of Technology (2005).
- [116] P. Schindler. *Frequency synthesis and pulse shaping for quantum information processing with trapped ions*. Diploma thesis, Universität Innsbruck, Austria (2008).
- [117] <http://sourceforge.net/projects/pulse-sequencer/>.